Doctoral theses at NTNU, 2016:361

Magnus Nord

EELS and STEM studies of perovskite oxide heterostructures

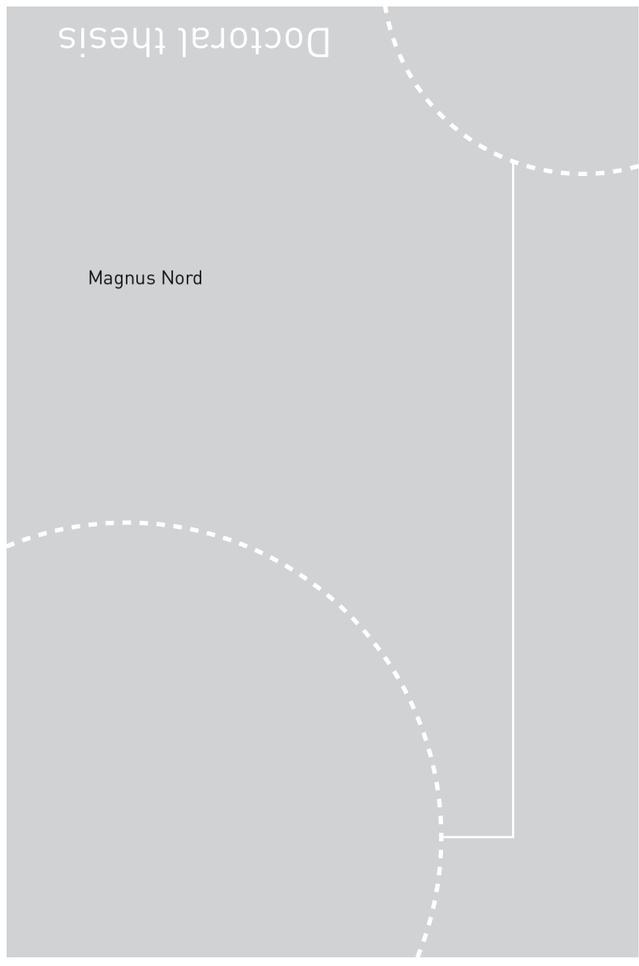

ISBN 978-82-326-2066-1 (printed ver.)
ISBN 978-82-326-2067-8 (electronic ver.)
ISSN 1503-8181

NTNU
Norwegian University of
Science and Technology

NTNU
Norwegian University of
Science and Technology
Thesis for the Degree of
Philosophiae Doctor
Faculty of Natural Sciences and Technology
Department of Physics

Doctoral theses at NTNU, 2016:361

NTNU
Norwegian University of
Science and Technology

Magnus Nord

EELS and STEM studies of perovskite oxide heterostructures

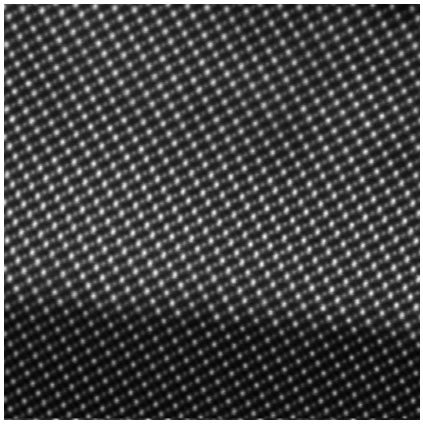

Thesis for the Degree of Philosophiae Doctor

Trondheim, December 2016

Norwegian University of Science and Technology
Faculty of Natural Sciences and Technology
Department of Physics

NTNU
Norwegian University of
Science and Technology

NTNU
Norwegian University of Science and Technology

Thesis for the Degree of Philosophiae Doctor

Faculty of Natural Sciences and Technology
Department of Physics

ISBN 978-82-326-2066-1 (printed ver.)
ISBN 978-82-326-2067-8 (electronic ver.)
ISSN 1503-8181

Doctoral theses at NTNU, 2016:361

Printed by NTNU Grafisk senter

Abstract

Perovskite oxide heterostructures have attracted much research interest due to a strong coupling between the local crystal structure and the functional properties. Of special interest are the interfaces of thin film systems, where novel phases can occur from this phenomenon. This gives these materials a large range of functional properties, making them good candidates for use in novel device concepts like spintronics. To tailor-make devices from perovskite oxide heterostructures we need to understand their detailed structure at subnanometer scales. Transmission Electron Microscopy is an ideal tool for this due to the atomic resolution and wealth of experimental signals. In particular Scanning Transmission Electron Microscopy (STEM) and Electron Energy Loss Spectroscopy (EELS) are powerful techniques to investigate the crystal and electronic structure in these materials.

EEL spectra contain a wealth of information used to examine the electronic structure of a material at the atomic level. However, EELS data is often difficult to analyse quantitatively due to its complicated spectral features. In this project, a method to quantitatively and automatically analyse EEL spectra has been developed. The method is based on the model based approach, and has been implemented in the free and open source program HyperSpy. Utilizing this method, detailed information about oxidation state and the presence of oxygen vacancies has been extracted.

From high quality atomic resolution STEM images the position of individual atomic columns is resolvable. This technique can therefore be used to investigate small structural changes in a material. Most challenging is the analysis of light elements, such as the oxygen column. As displacement of oxygen atoms is a common type of structural distortion in perovskite oxide heterostructures, there is a need for good methods to find the position and shape of oxygen columns. In this project, the program Atomap was developed to be able to automatically, accurately and robustly find the position and shape of all cation and oxygen columns.

In this work, STEM, EELS, Atomap and HyperSpy have been used to study the atomic and electronic structure of three different material systems. These have been $La_{0.7}Sr_{0.3}MnO_3$ (LSMO) grown on (001)-oriented $SrTiO_3$ (STO),

LSMO grown on (111)-oriented STO and a bilayer system $La_{0.7}Sr_{0.3}MnO_3/LaFeO_3$ (LSMO/LFO) grown on (111)-oriented STO.

In the LSMO/STO-(001) system, analysis of STEM and EELS data revealed the presence of oxygen vacancies and a reduction in the Mn oxidation state at the interface. In co-junction with STEM-imaging, a different structural phase was observed on the LSMO side of the interface, compared to the bulk of the thin film. This phase was identified as a Brownmillerite structure with unordered oxygen vacancies, which became ordered over time.

Using STEM-EELS, chemical intermixing was studied in the heterostructures grown on (111)-oriented STO. Cation intermixing was observed on the STO interfaces. The terminating layer of the STO substrate was Sr-deficient, leading to a thin $LaSrTiMnO_3$ layer at the interface.

When a LSMO/LFO bilayer was grown on (111)-oriented STO, structural changes were seen in both LFO and LSMO. Atomap was used to analyse the atomic structure. The position of all the atomic columns including oxygen was found, this revealed structural coupling between the LSMO and LFO.

An important consideration is potential sample damage from the electron probe. Therefore, beam damage on the perovskite oxide materials was studied by exposing the TEM sample to varying electron doses. Beam damage effects were observed in both EELS and STEM data. Importantly, it was found that in LSMO, sample damage can occur without it being visible in the STEM images. The damaged area also extended into the region surrounding the exposed area. This shows careful examination of potential beam damage is vital. To facilitate this, a standard method for assessing a TEM sample for beam damage susceptibility was suggested.

Acknowledgments

As my main advisor through my PhD project, Prof. Randi Holmestad has with her long experience with TEM and positive attitude been a great support and facilitator for my work.

Dr. Per Erik Vullum has also shared his extensive knowledge and experience in advanced TEM-techniques, crystallography and sample preparation with me, and this has been vital for getting the high quality data presented in this thesis.

As a great repository of knowledge of functional materials and perovskite oxides Prof. Thomas Tybell has been of great help for me when trying to understand the structure and materials I've studied, as well as giving suggestions on how to improve the quality of my article manuscripts.

I like to thank my collaborators in the Oxide Electronics group at Department of Electronics and Telecommunications. Ingrid Hallsteinsen and Jos Boschker for growing the thin film systems I have been studying, and Magnus Moreau for running DFT-calculations on these material systems.

I'm grateful to all the people in the TEM-group at NTNU for valuable scientific discussions, and a great social environment. Especially Ragnhild Sæterli and Bjørn Soleim for keeping the sample preparation labs and TEMs running smoothly.

I would also like to extend a big thanks to NTNU Nanolab, especially Ken Roger Ervik, for keeping the FIB-SEM in excellent working conditions. Also a big thanks to Dr. Vidar Fauske for valuable tips and tricks on how to make TEM-samples using the FIB.

I'd also like to thank to Prof. Jian Min Zuo at University of Illinois at Urbana-Champaign for hosting me during my research stay there.

Honorable mentions to Dr. Ian MacLaren at University of Glasgow for accelerating the preparation of the manuscript in Paper IV.

Preston Buscay is acknowledged for diligent proof-reading.

Lastly, but not least, my lovely girlfriend Ida Hjorth for support, encouragement and proof-reading.

With regards to funding sources the Norwegian PhD Network on Nanotech-

nology for Microsystems is acknowledged for funding my PhD-position. The Norwegian PhD Network on Nanotechnology for Microsystems is sponsored by the Research Council of Norway (RCN), Division for Science, under contract number 190086/S10. Instrument and training time on the FIB at the NTNU Nanolab was supported by the Norwegian Micro- and Nano-Fabrication Facility (Norfab), which is supported by the RCN under contract number 197413/V30. The NORTEM project is acknowledged for partial funding of TEM instrument time, grant 197405 through the INFRASTRUCTURE program of the RCN.

Preface

This thesis is submitted as fulfillment of the requirements for the degree of philosophiae doctor (PhD) at the Norwegian University of Science and Technology (NTNU). The work was carried out at the Department of Physics (IFY), at NTNU, from August 2011 to October 2016. For Paper I, most of the experimental work was performed at the Technical University of Denmark - Center for Electron Nanoscopy (DTU-CEN). For Paper II-V the experimental work was carried out at the NORTEM and NanoLab facilities at NTNU. I also spent 6 months on a research stay at University of Illinois at Urbana–Champaign with Prof. Jian Min Zuo's group.

Publications included in this thesis

Paper I

M. Nord, P. E. Vullum, M. Moreau, J. E. Boschker, S. M. Selbach, R. Holmestad, and T. Tybell. *Structural phases driven by oxygen vacancies at the $La_{0.7}Sr_{0.3}MnO_3$/ $SrTiO_3$ hetero-interface.* Applied Physics Letters 106, 041604, (2015). DOI: 10.1063/1.4906920

Paper II

M. Nord, P. E. Vullum, I. Hallsteinsen, T. Tybell, and R. Holmestad. *Assessing electron beam sensitivity for $SrTiO_3$ and $La_{0.7}Sr_{0.3}MnO_3$ using Electron Energy Loss Spectroscopy.* Ultramicroscopy 169, (2016). DOI: 10.1016/j.ultramic.2016.07.004

Paper III

I. Hallsteinsen, **M. Nord**, T. Bolstad, P. E. Vullum, J. E. Boschker, P. Longo, R. Takahashi, R. Holmestad, M. Lippmaa, and T. Tybell. *Effect of Polar (111)-*

Oriented $SrTiO_3$ on Initial Perovskite Growth. Crystal Growth & Design, 16, 2357-2362, (2016). DOI: 10.1021/acs.cgd.6b00143

Paper IV

M. Nord, P. E. Vullum, I. MacLaren, T. Tybell, and R. Holmestad. *Atomap: a new software tool for the automated analysis of atomic resolution images using 2-dimensional Gaussian fitting.* Submitted to Advanced Structural and Chemical Imaging.

Paper V

I. Hallsteinsen, M. Moreau, A. Grutter, **M. Nord**, P. E. Vullum, D. A. Gilbert, T. Bolstad, J. K. Grepstad, R. Holmestad, S. M. Selbach, A. T. N'Diaye, B. J. Kirby, E. Arenholz, and T. Tybell. *Concurrent magnetic and structural reconstructions at the interface of (111)-oriented $La_{0.7}Sr_{0.3}MnO_3/LaFeO_3$.* Physical Review B 94, 201115(R) (2016). DOI: 10.1103/PhysRevB.94.201115

Author's contribution

In Paper I M.N. did the sample preparation of the TEM-lamellas using mechanical wedge polishing and ion milling. M.N. performed the HR-STEM and EELS characterization, with assistance from Takeshi Kasama. M.N. did the STEM strain, and STEM-EELS data processing with assistance from P.E.V.. M.M. and S.M.S. performed the DFT calculations, analysis of the DFT results and manuscript text related to the DFT. J.E.B. synthesised the thin film sample, and performed the X-ray analysis. M.N. was in charge of the manuscript writing, with large contributions from R.H., T.T. and P.E.V., and input from the other co-authors.

M.N. came up with the initial idea and concept for Paper II, and did the experimental STEM-imaging and EELS work. He also did the TEM-lamella sample preparation with a FIB. M.N. did the software development for the tools used to process EELS data. I.H. synthesised the thin film materials. M.N., R.H., T.T. and P.E.V. interpreted and analysed the results. M.N. drafted the manuscript, discussed it with the co-authors and finalized the manuscript.

For Paper III, M.N. did the STEM-EELS characterization of the LSMO/LFO/STO-(111) sample together with P.L.. M.N. did the STEM-imaging and EELS characterization of the LSMO/STO-(111) sample. He also did

the EELS processing and analysis. M.N. commented on the manuscript drafted by I.H.. M.N. made the TEM figures. M.N. also contributed the EELS results and analysis in the supporting information.

M.N. came up with the initial concept for the work in Paper IV, and did FIB-sample preparation and the experimental STEM-imaging. In addition, he did the development of the software tools. M.N. drafted the manuscript, with input from the co-authors.

In Paper V, M.N. did the TEM-sample preparation using FIB, and performed the STEM ABF, HAADF and EELS characterization. He also did the STEM ABF, HAADF and EELS data processing, and analysis with P.E.V. and R.H.. M.N. commented on the manuscript drafted by I.H.. M.N. made the TEM figures. M.N. also contributed to the supporting information.

Selected presentations

M. Nord, J. E. Boschker, P. E. Vullum, T. Tybell, R. Holmestad. *Transmission Electron Microscopy characterization of* $La_{0.7}Sr_{0.3}MnO_3/SrTiO_3$ *ferroelastic thin films.* 2012 MRS Fall Meeting & Exhibit, Boston, USA, 2012 [Poster]

M. Nord, J. E. Boschker, P. E. Vullum, T. Tybell, R. Holmestad. *Study of electronic reconstruction in* $La_{0.7}Sr_{0.3}MnO_3/SrTiO_3$ *thin film interface using Transmission Electron Microscopy.* 4th annual workshop of the Norwegian PhD Network on Nanotechnology for Microsystems, Bergen, Norway, 2013 [Talk]

M. Nord, J. E. Boschker, M. Moreau, P. E. Vullum, S. M. Selbach, T. Tybell, R. Holmestad. *Structural and electronic characterization of altered structure at the* $La_{0.7}Sr_{0.3}MnO_3/SrTiO_3$ *heteroepitaxial interface.* 2014 MRS Spring Meeting & Exhibit, San Fransisco, USA, 2014 [Talk]

Publications not included in the thesis

- J. E. Boschker, Å. F. Monsen, **M. Nord**, R. Mathieu, J. K. Grepstad, R. Holmestad, E. Wahlstrom, T. Tybell. *In-plane structural order of domain engineered* $La_{0.7}Sr_{0.3}MnO_3$ *thin films.* Philosophical Magazine, 93, 13, (2013). DOI: 10.1080/14786435.2012.747010

- I. Hallsteinsen, J. E. Boschker, **M. Nord**, S. Lee, M. Rzchowski, P. E. Vullum, J. K. Grepstad, R. Holmestad, C. B. Eom and T. Tybell. *Surface*

stability of epitaxial $La_{0.7}Sr_{0.3}MnO_3$ thin films on (111)-oriented $SrTiO_3$. Journal of Applied Physics 113, 183512 (2013). DOI: 10.1063/1.4804312

- F. A. Martinsen, B. K. Smeltzer, **M. Nord**, T. Hawkins, J. Ballato, U. J. Gibson. *Silicon-core glass fibres as microwire radial-junction solar cells.* Scientific Reports, 4, 6283, (2014). DOI: 10.1038/srep06283

- E. Christiansen, **M. Nord**, I. Hallsteinsen, P. E. Vullum, T. Tybell and R Holmestad. *Structural investigation of epitaxial $LaFeO_3$ thin films on (111) oriented $SrTiO_3$ by transmission electron microscopy* Journal of Physics: Conference Series, 644 (2015). DOI: 10.1088/1742-6596/644/1/012002

- N. P. Wagner, P. E. Vullum, **M. Nord**, A. M. Svensson and F. Vullum-Bruer. *Vanadium Substitution in Li_2MnSiO_4/C as Positive Electrode for Li Ion Batteries*, Journal of Physical Chemistry C, 120 (2016). DOI: 10.1021/acs.jpcc.6b01831

List of acronyms

ABF annular bright field

ADF annular dark field

CFEG cold field emission gun

EELS electron energy loss spectrum

ELNES electron energy loss near edge structure

EXELFS extended electron energy loss fine structure

FFT fast Fourier transform

FIB focused ion beam

GPA geometrical phase analysis

HOLZ higher order laue zone

HRSTEM high-resolution scanning transmission electron microscopy

LAO $LaAlO_3$

LFO $LaFeO_3$

LSMO $La_{0.7}Sr_{0.3}MnO_3$

PCA principal component analysis

PLD pulsed laser deposition

RHEED reflection high-energy electron diffraction

STEM scanning transmission electron microscopy

STO $SrTiO_3$

TEM transmission electron microscopy

XAS X-ray absorption spectroscopy

ZLP zero loss peak

Contents

Part I

Introduction

Chapter 1

Motivation

The electronic industry requires smaller and smaller components to continue increasing the computing power and storage capacity in modern devices. This is exemplified by "Moore's law", which is the observation that the transistor density doubles approximately every second year. However, as the semi-conductor based transistors get smaller, one starts to run into physical limitations. This necessitates new kinds of devices, based on materials with novel properties such as perovskite oxides[1, 2].

Perovskite oxides are interesting due to their large range of functional properties. These include properties such as ferroelectricity[3], ferromagnetism[4], multiferroicity[5] and colossal magnetoresistance[4]. The large range of properties is due to a strong structure - function coupling, meaning small changes in the structure of the material can lead to large changes in how the material functions.

What makes these materials interesting from a device perspective are the many different ways the structure, and therefore the functional properties, can be influenced. This potentially allows for fine tuning of the device's functional properties. Recent developments in synthesis methods have enabled the growing of these materials as high quality thin films, using another perovskite as substrate[3, 6, 7]. This unlocks even more ways of influencing the structure, as the thin film's structure will be affected by the substrate's structure. To properly understand the physics of these thin film systems one must understand what happens on the interface between the film and substrate, ideally at the atomic scale.

There are many different advanced characterization techniques which can be used to study perovskite oxides thin films, like Scanning Tunneling Microscopy (STM)[8], neutron diffraction[9] and synchrotron based X-ray techniques[9, 10]. One of the most versatile is aberration corrected Transmission Electron Microscopy (TEM), which allows imaging down to individual atomic columns, enabling a high degree of structural characterization. This can be coupled with complementary

spectroscopic techniques, which can probe the orbital and electron structure at the same length scales. Combining the structural and spectroscopic characterization makes it possible to study the same local area simultaneously, acquiring a vast amount of information about these perovskite oxide heterostructure interfaces.

The aim of this thesis has been to characterize the interfaces of perovskite oxide thin films using advanced Transmission Electron Microscopy techniques. These techniques include high-resolution Scanning Transmission Electron Microscopy (STEM) combined with Electron Energy Loss Spectroscopy (EELS). Both techniques give a wealth of information, however often very little of the rich information contained in these data types is actually utilized. Thus, the focus of this PhD-work has been to develop better tools for analysing both EELS and atomic resolution STEM data.

This thesis consists of an introduction part followed by 5 papers. The introduction will give an overview of the methods used and materials examined in this work. This will include an overview of STEM methods and techniques, and a discussion of the perovskite oxide material system. As the development of data processing methods is an important aspect of this thesis, a literature review of the different processing methods for STEM-imaging and EELS data is given, focused on the studies of perovskite oxides. Lastly, the results are summarized and possible future work is outlined.

Chapter 2

Method and materials

This chapter will cover the methods which have been used, and the materials which have been studied in this work. The methods section include advanced aspects of scanning transmission electron microscopy (STEM). The materials section gives an overview of the perovskite oxide structure, and how the perovskite oxide functional properties can be changed. Lastly, it also includes a brief overview of the sample preparation techniques used in this project.

2.1 Scanning Transmission Electron Microscopy

This section will briefly discuss different aspects of STEM, focusing on the more advanced facets of using such an instrument. For more information about the basic concepts of a Transmission Electron Microscopy (TEM) and STEM, see the book *Transmission Electron Microscopy* by Williams and Carter[11].

2.1.1 Operating principles

In STEM one uses a convergent electron probe, which is focused into a narrow spot. This spot is scanned across the sample in a raster pattern, meaning the various signals are generated from a small point in the sample. A schematic of the inner workings of a STEM is shown in Figure 2.1a. Going from the top: the electrons are generated; passed through the condenser system to create a sharp probe; and scanned in a raster pattern (Figure 2.1b) across the sample using scanning coils. Of special interest is the wealth of signals which can be acquired simultaneously. Due to the small spatial extent of the beam, the signal is generated in a small region: down to a single atomic column or, in some 2D materials, from a single atom.

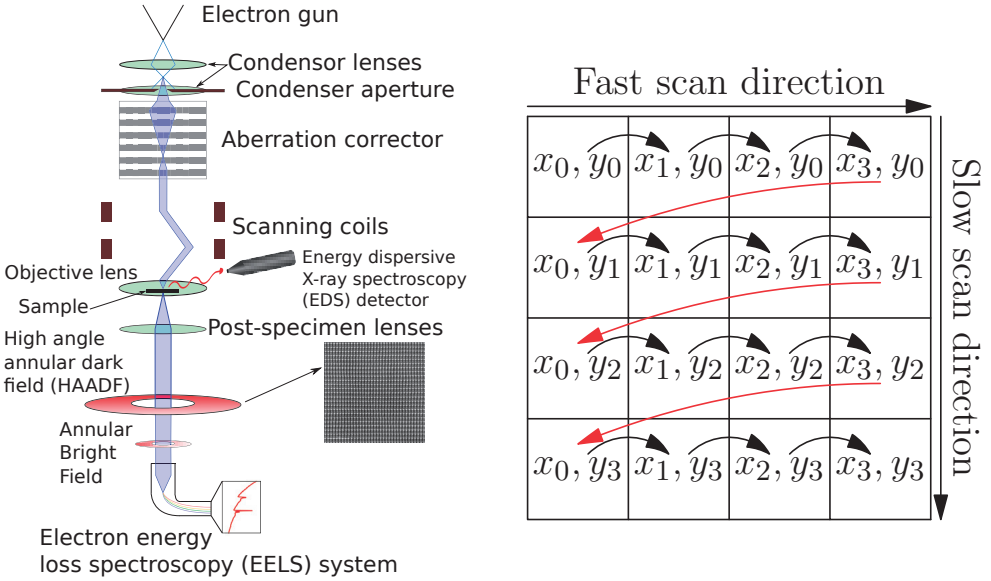

Figure 2.1: (a) Inner workings of a STEM. The scan coils scan the electron beam across the sample in a raster pattern, as shown in (b).

Electron gun

The type of electron gun greatly affects the size of the electron probe, and important parameters are energy spread and brightness. Chromatic aberrations increase the probe size, but a low energy spread reduces this effect. A low energy spread is also important for doing electron energy loss spectroscopy, which is outlined in Section 2.1.2.

The brightness is a measure of how many electrons the gun can emit per second. The brightness is vital, since one needs a high probe current to be able to image things faster than the microscope instabilities such as sample drift. The electron gun in the Jeol ARM microscope in Trondheim is a cold field emission gun, and it is optimal for doing STEM-imaging and spectroscopy: the low energy spread makes it possible to access much of the fine details in this rich data types, and the high brightness of the gun means that acquisitions can be rapid. This rapid acquisition also helps mitigate the effects of microscope instability discussed in Section 2.1.1.

Aberration correction

Imperfections in round electromagnetic lenses lead to lens aberrations and broadening of the electron probe, but many of these aberrations can be reduced with

aberration correctors[12, 13]. These are a relatively recent development, giving a smaller probe size that has enabled imaging of sub-ångstrom features in STEM. The STEM aberration corrector is placed after the condenser lenses, and a STEM with this kind of aberration corrector is often called a probe corrected STEM. Probe correctors allow for higher probe brightness without compromising probe size. This makes it possible to use spectroscopic techniques which require a high amount of electron counts, such as EELS (Section 2.1.2). Probe aberration corrected instruments have been vital for this project, and all the experimental TEM work has been done on aberration corrected STEM instruments. However, the details on how these correctors work are outside the scope of this thesis. A thorough introduction to (S)TEM aberration correction can be found in *Aberration-Corrected Imaging in Transmission Electron Microscopy* by Rolf Erni[14].

Microscope stability

An often overlooked aspect of acquiring atomic resolution images is the effect of microscope stability[15]. The stability is affected by factors such as temperature, mechanical vibrations, magnetic and electric fields.

Temperature changes can lead to thermal expansion or contraction in the microscope column and sample holder. Normally this is not very noticeable, but when we're trying to image features on the atomic scale this effect can be of great annoyance. One source of temperature instability is the temperature of the microscope room, which is affected by computers, the microscope itself and people inside the room. This issue can be reduced by having an air circulation system creating laminar airflow and water-cooled walls. But even with the cooling systems, having too many people inside the room will create excess heat. The cooling systems in these microscope rooms are often designed to handle a maximum amount of people (often 2). However, in my anecdotal experience, ideally there should be only 1 person inside the microscope room. Also, it can take hours for the room temperature to stabilize properly. Simply opening the door to the microscope room can introduce large amount of sample drift. This is shown in Figure 2.2, where the images are from several long exposure spectroscopic acquisition in the same microscope session. In the last acquisition the door was opened briefly, leading to large sample drift. One solution to this is to have a remote controlled microscope, however the microscope used in this work did not have this capability.

Another source of temperature instability is the microscope lenses themselves. Since they are electromagnetic lenses, the power of the lenses are changed by increasing or decreasing the electron current flowing through them. This changes the heat generation from the lenses, and can lead to thermal instability. This is especially apparent when doing EELS on a Jeol ARM, since that requires going to

low camera lengths which induce large changes in the current to the illumination system lenses. Thus, when doing EELS experiments, one should not change the camera lengths, but rather do microscope alignments on the same detector as one use to acquire the EELS data.

Most high end TEMs are placed in special-built rooms, with large amount of vibration damping. While this greatly reduces the effect of mechanical vibrations, the best time to do high resolution experiments is when there is as little activity as possible: evenings, weekends, or most preferably Sunday nights. This also applies to magnetics fields created by trains, subways, cars and lorries. The easiest solution is to do experiments when these vehicles are not in use.

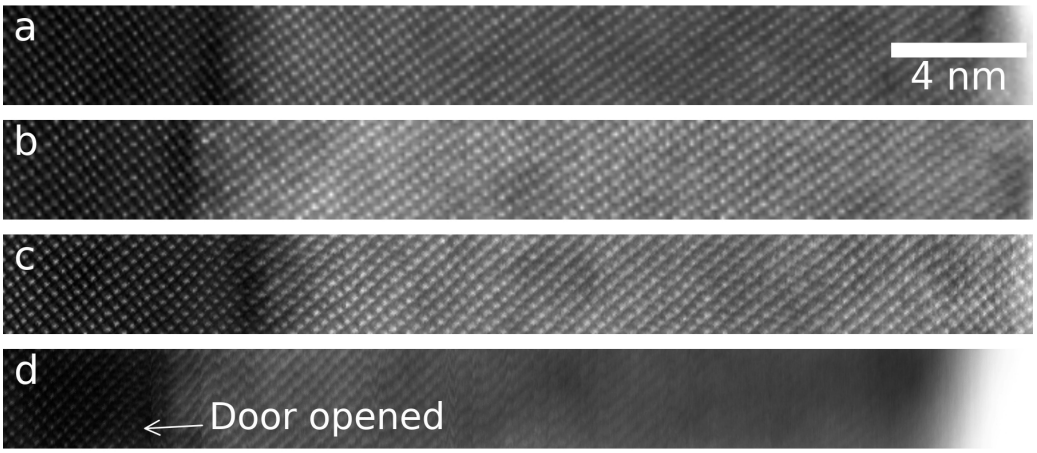

Figure 2.2: Ambient temperature effects on microscope stability when acquiring 16 minute exposure spectroscopic data. Images show data from several spectrum images acquired in the same session. (a-c) Acquired when the microscope and room are thermally stable, after about 2 hours of not opening the door, not changing the lens setting significantly and with only one person in the microscope room. (d) At the point annotated by the arrow, the door to the microscope room was briefly opened and closed, with the person leaving the room. This induced large amounts of sample drift.

Image averaging

One solution for many of the instabilities, is acquiring multiple frames rapidly and average them in post processing. By having a sufficiently fast acquisition rate the instabilities and distortions are uncorrelated, and can be averaged out. In addition, this can be coupled with corrections of well-known scanning instabilities. One such implementation is Smart Align developed by Lewys Jones[16], which has

been used in this project. This is used in Paper IV to increase the precision of determining the position of atomic columns.

2.1.2 Signals

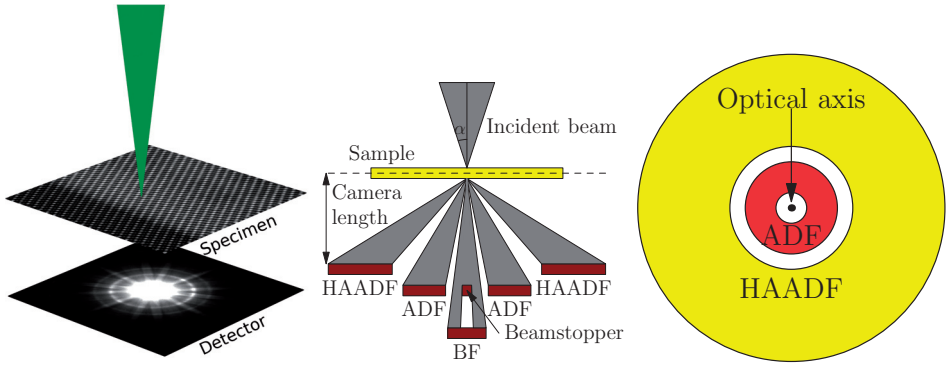

Figure 2.3: Leftmost image: schematic of a convergent electron beam hitting a sample, and electrons scattering onto the detector plane. Middle image: Showing location of various detectors from the side. Convergence semiangle α and camera length L. Rightmost image: ADF and HAADF detectors from a topside viewpoint.

Having generated a sharp convergent electron probe, the next step is passing it through the material to be characterized. The electron beam interacts with the sample and generates a convergent beam electron pattern in the back focal plane, as shown in the leftmost image in Figure 2.3. Different interaction mechanisms scatter the electrons in the beam to different angles.

Detection of the scattered and unscattered electrons in the beam is normally done by placing a detector in the back focal plane. This is seen in the middle image in Figure 2.3, which shows some commonly used detectors when doing STEM-imaging. The important parameters are the collection semi-angles, which is determined by the distance from the sample to the detectors. However, the detectors are locked to a specific physical position, so the distance to the detectors (camera length) is handled by the post-specimen lenses. Thus, one can change between 2 to 200 cm camera lengths easily.

High angle scattering

Scattering to above ≈ 100 mrad scattering angle is often called High Angle Annular Dark Field (HAADF) or "Z-contrast", as there is a proportionality to the atomic number ($\approx Z^2$). However, this Z-contrast interpretation is often affected by a number of factors, for example: diffraction effects[17], electron channeling along

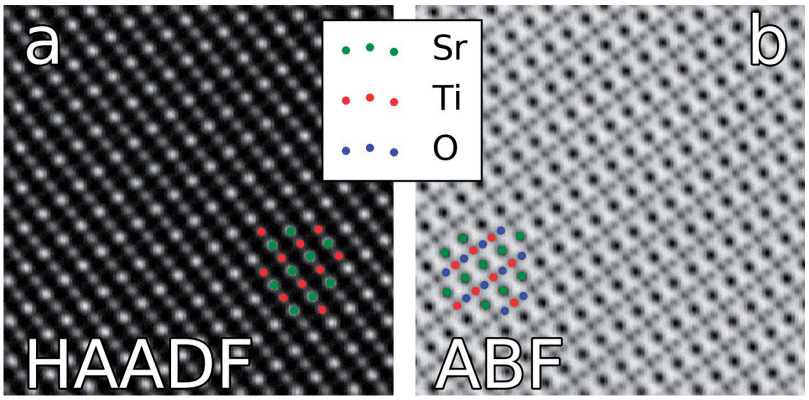

Figure 2.4: Atomic resolution STEM images of $SrTiO_3$ with the electron beam parallel to the $[1\bar{1}0]$ direction. (a) Annular Dark Field (ADF, 73 to $\approx$ 170 mrad) image showing Z-contrast, where heavier elements are brighter compared to lighter elements. This is seen with the Sr and Ti atomic columns, which have atomic numbers 38 and 22, respectively. (b) Annular Bright Field (ABF, 11 to 23 mrad) image acquired simultaneously with (a). Here, the O columns are clearly visible, and can be used to infer octahedral tilting in the perovskite structure. This can be seen in Paper IV and Paper V.

the atomic columns [18] and effects of defects in the structure[19]. An example of the higher order laue zone (HOLZ) diffraction effects is seen in the leftmost image in Figure 2.3, where the bright rings are due to a doubling of the unit cell parallel to the electron beam. These rings can appear above 100 mrad, and they may cause certain atomic columns to appear more intense than they should under the more simplistic "Z-contrast" interpretation[17].

While there are many caveats when trying to use HAADF to precisely determine the quantity of specific elements in a material, often called quantitative STEM[20], this imaging mode has many advantages. It mostly originates from incoherent thermal diffuse scattering, which is approximately proportional to the number of protons in the atomic nucleus squared (Z^2)[21]. It works well on thicker samples, and the interpretation is normally fairly straight forward[18]. An example of this is shown in Figure 2.4a, which shows an ADF image of $SrTiO_3$. Here, the heavier strontium (Z = 38) atomic columns are brighter compared to the titanium (Z = 22) columns, while the oxygen (Z = 8) columns are almost impossible to see.

Annular bright field

Annular Bright Field (ABF) relies on using the low scattering angles from about 11 to 23 mrad, with an electron probe convergence angle of about 20 mrad[22]. Compared to ADF, ABF enables the imaging of lighter elements as shown in Figure 2.4b, where the oxygen atomic columns are clearly visible. For analysing perovskite oxide materials this is very useful, since the oxygen positions can be used to infer the octahedral tilt pattern[23]. Such analysis is discussed in more detail in Section 3.2, and has been used in Paper IV and V. While being able to image light elements is very useful, this imaging mode has several pitfalls. To actually image the oxygen columns one needs thinner samples compared to ADF, and ADF is much more sensitive to beam alignments, meaning it is much harder to practically make it work[22–24].

Also, the technique relies on keeping the centre of the beam in the middle of the beam stopper shown in Figure 2.3. Thus, any effect which shifts the center beam in the detector plane can change the location of the atomic columns, which can be misinterpreted as changes in the material. There are several ways to cause such a shift: i) impure scan shift/tilt, often called d-scan, leads to the beam shifting in the detector plane when scanning in the sample plane. It is possible to compensate for this using post-specimen deflectors, but the microscope (Jeol ARM200CF) which was used to do the ABF imaging in this work did not have this functionality. With a properly aligned microscope, this is not an issue when scanning over small regions $\approx$ 50 nm. ii) Electric[25] and magnetic[26] fields can also lead to a beam shift, due to the Lorentz force. iii) Simply by not properly centering the beam on the beam stopper.

Electron Energy Loss Spectroscopy

When the electron beam passes through the material, it will lose energy to inelastic scattering events. Most of these inelastic events occurs when the electron beam excites electrons in the materials through a variety of mechanisms: plasmon excitations, band transitions, inner shell ionizations, phonon excitations and Cherenkov radiation[27]. One can detect these changes by passing the electron beam through an electron spectrometer, which will spread the electrons as a function of energy. By subtracting the energy of the electrons in the beam, one can get the electron intensity as a function of how much energy they have lost. The result is an electron energy loss spectrum (EELS), shown in Figure 2.5.

Figure 2.5a shows a typical EEL spectrum, which includes all the major features. The zero loss peak (ZLP) is the most intense feature and contains the electrons which do not lose any energy when passing through the sample, and is used to calibrate the energy offset. The region after the ZLP to about 100 eV en-

ergy loss is commonly called the low loss, and contain the characteristic plasmon peaks. The energy region from about 100 eV and higher is normally called high loss (or core loss) and contains most of the core loss features which are due to inner shell ionizations. In this work the inner shell ionizations have been the most important, so those will be the focus here.

As mentioned earlier, an important development for doing EELS is Cold Field Emission Guns (CFEG). Compared to regular Field Emission Guns (FEG), the CFEG produces an electron beam with less energy spread. This greatly increases the energy resolution possible when doing EELS[27].

Another way of reducing the energy spread is by using a monochromator[27], which is used to exclude electrons with too high and too low energy. This effectively decreases the energy spread by sacrificing beam intensity. The monochromator is very useful for probing low energy losses like plasmons and band-gaps. However, the reduction in beam intensity makes it less useful for higher energy losses like inner shell ionizations in perovskite oxides, due to the smaller scattering cross section for these events. So traditionally, monochromators have not been used for these kinds of EELS experiments. However, some modern instruments have advanced monochromators combined with a CFEG, which enable both a small and a relatively intense electron probe[28]. The Trondheim Jeol ARM used for most of this work did not have a monochromator.

EELS: Inner shell ionizations

One process by which the electrons in the beam can lose energy is through inner shell ionizations. These processes occur when an electron in the material is excited from a filled inner electron shell to an empty or partially filled outer electron shell. A schematic of this excitation for manganese in a perovskite structure is shown in Figure 2.5d. The energy differences between these shells are different for every element, so the ionization events can be used to determine which elements are present in a material[27]. An example of this is shown in Figure 2.5b, which shows a typical core loss spectrum from $La_{0.7}Sr_{0.3}MnO_3$, outlining the major features: i) The plasmon background which is normally fitted with a power law and subtracted is shown with green. ii) Core loss edges which create a continuum background, for transition metals these edges commonly have white lines[27]. Having subtracted the plasmon background, one gets the signal originating from a specific core loss edge (Figure 2.5c). The core loss edge is commonly divided into two separate regions: electron energy loss near edge structure (ELNES) and extended electron energy loss fine structure (EXELFS). This is shown in Figure 2.5c for Mn-$L_{2,3}$, where the two clearly defined peaks are part of the ELNES, and the more diffuse post-edge belongs to the EXELFS[27].

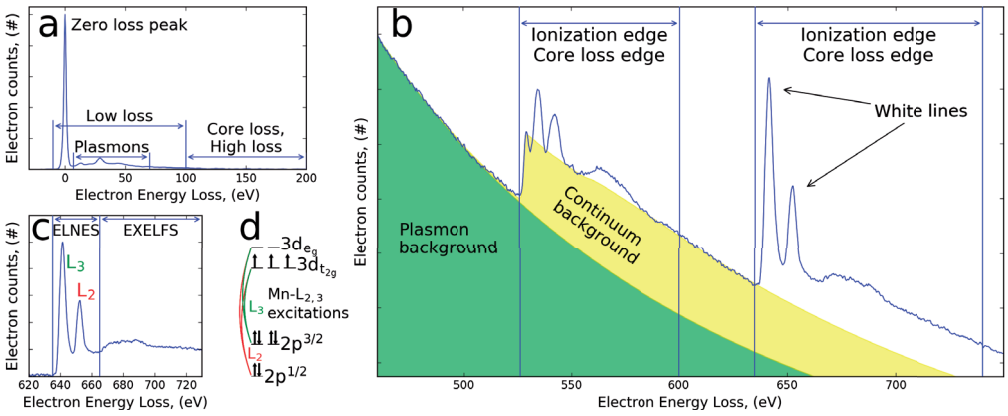

Figure 2.5: Electron energy loss spectrum from the transition metal perovskite oxide $La_{0.7}Sr_{0.3}MnO_3$. (a) A typical EEL spectrum for a thin sample, showing the major features. (b) Core loss region, with the background (green) and the core loss edges O-K and Mn-$L_{2,3}$. Continuum background from O-K edge shown with yellow. (c) Mn-$L_{2,3}$ core loss edge with the background removed, showing the two major parts: electron loss near edge structure (ELNES), and extended electron energy loss fine structure (EXELFS). (d) Inner shell excitation for Mn^{3+}. Excitations from $2p^{3/2}$ to 3d are called L_3, $2p^{1/2}$ to 3d are called L_2.

The transition metal perovskite oxide heterostructures are especially suited for core loss EELS. This is due to the transition metals having very well defined ELNES which are sensitive to a variety of physical parameters such as oxidation state[7, 29–31] and crystal structure modifications[32]. The ELNES signal is also strong, making it easy to examine compositional variations such as cation intermixing[33, 34]. In addition, the oxygen K-edge (1s to 2p) is also sensitive to the B-cation oxidation state[29] and presence of oxygen vacancies[19, 35].

The core loss edges for the materials studied in this work are also positioned fairly close to each other without directly overlapping (see Table 2.1), and at relatively low energy losses (below 1000 eV). Thus, all these edges can be acquired in the same exposure, making this type of data easy to acquire. In addition, many of the features are coupled. For example, oxygen vacancies may lead to a change of both the oxygen-K edge and the Mn-$L_{2,3}$ edges.

Combining STEM with EELS enables the acquisition of this kind of data at sub-ångstrom resolutions. This enables the characterization of local chemical and electronic structure for a variety of materials. Perovskite oxide heterostructures are often studied in this context, since the interesting physics can often reside down to single monolayers[36].

Quantifying these core loss edges can be done by fitting components to the

Table 2.1: List of the perovskite oxide materials studied in this work. Showing element number (Z), oxidation state for each of the elements (Ox. state), electron configuration (El. config.) and the experimental EELS edge onsets[27].

		Z	Ox. state	El. config.	EELS edge onset
$SrTiO_3$	Sr	38	+2	[Kr]	$L_{2,3}$: 1940 eV
	Ti	22	+4	[Ar]	$L_{2,3}$: 455 eV
	O	8	-2	[Ne]	K: 532 eV
$La_{0.7}Sr_{0.3}MnO_3$	La	57	+3	[Xe]	$M_{4,5}$: 832 eV
	Sr	38	+2	[Kr]	$L_{2,3}$: 1940 eV
	Mn	25	+3.3	[Ar] $3d^{3.7}$	$L_{2,3}$: 640 eV
	O	8	-2	[Ne]	K: 532 eV
$LaFeO_3$	La	57	+3	[Xe]	$M_{4,5}$: 832 eV
	Fe	26	+3	[Ar] $3d^5$	$L_{2,3}$: 708 eV
	O	8	-2	[Ne]	K: 532 eV

experimental signal, which is called the model based approach[37]. This approach is used in Paper I, IV, V and especially Paper II. The different methods used in literature for analysing EELS data is discussed in detail in Section 3.1. Finding the optimal settings for EELS experiments is a trade-off between many different factors, for example between signal-to-noise and energy resolution. This is also discussed in Paper II.

2.1.3 Quantifying atomic positions

An important part of characterizing crystals is getting accurate atomic position data. For single crystals, this can be done to very high precision using X-ray diffraction based techniques. However, thin film interfaces contribute very little intensity to the X-ray diffraction patterns. In addition, the size of the X-ray beam also limits the spatial resolution since the X-ray beam will cover a large area of the thin film.

Atomic resolution STEM images contain a wealth of information, as shown in Figure 2.6. Fourier based techniques are often used to do structural characterization on such datasets. Simply using a 2D fast Fourier transform (FFT) on the full or subset of an image can give information about the periodicities of the structure. This is a simple and easy method, which can reveal the presence of superstructures or changes of lattice parameter. An advanced Fourier method is Geometrical Phase Analysis (GPA) which is commonly used for determining strain fields and changes in lattice parameters[38]. While the Fourier methods can be very easy to use and can reveal very small displacements[39], the main limitation is

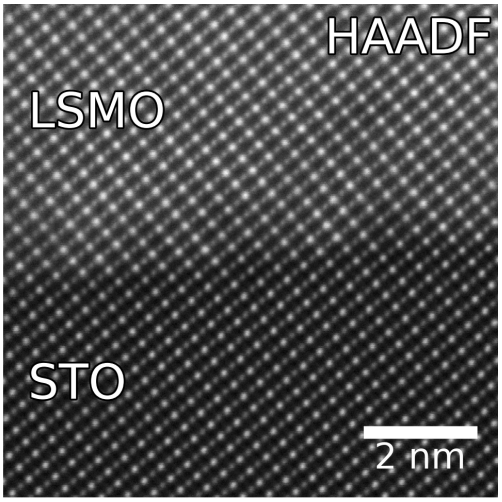

Figure 2.6: High resolution STEM-HAADF image of $La_{0.7}Sr_{0.3}MnO_3$ thin film grown on $SrTiO_3$, showing the great amount of information contained in this kind of atomic resolution data. The data has been acquired as an image stack and processed using Smart Align[16].

the low spatial resolution: they can not give information about individual atomic columns, due to the spatial resolution being limited to one unit cell when using a large mask[39].

Ideally one would like to use real space methods to study variations in atom positions, since they enable the analysis of individual atomic columns[40, 41]. We want to extract information on this length scale because interesting properties can reside in single atomic planes[7, 36]. In addition, one should use methods which can also extract information about the shape of the atomic columns as this can be used to infer the structure parallel to the electron beam[42, 43]. The software implementation Atomap using such a real space method is explained in Paper III. An extended discussion about the various methods using for such analysis is included in Section 3.2.

2.1.4 Data analysis tools

Much of the work during the PhD has been in developing software tools for data analysis. This has been motivated by the increasingly large amount of data which can be acquired in a single TEM session. For example, the newer generation EELS spectrometers can acquire up to 1000 spectra each second[27], and doing a simple line scan across a thin film can result in several thousand spectra. While this is

great for getting many high quality datasets, doing the data processing manually for each dataset or spectrum is clearly not practical. Thus, much of my work has been focused on automation of data processing, to allow for a similar high throughput of data processing. In addition, many of the current data processing toolkits are proprietary, which often makes it impossible to see exactly how the data processing algorithms are implemented. This basically means that by using them the processing is done in a "black box", as you do not really know exactly what has been done to your data[44–46].

The majority of the software development in this thesis has been implemented in HyperSpy (`http://hyperspy.org/`), which is a free and open source Python software package developed for analysing multi-dimensional data. A full list of the contributions can be found on HyperSpy's GitHub page[1]. The implementations developed and presented in this thesis can be summarized to a couple of main contributions:

- `model.fit_component`: function to fit a single component (such as a Gaussian, Lorentzian, ...) to a signal. Useful for setting initial values before doing a multi-component fit.

- `component.set_parameters_free`, `component.set_parameters_not_free`: utility functions for locking or unlocking several parameters in a component with one function.

- `plot_spectra`: visualization function for plotting spectral data.

- Many minor typos and smaller bug-fixes, and discussions on development issues.

In addition to the features already merged into the HyperSpy, there are some features in development in this project which will be merged at some later date:

- `model.set_coreloss_edge_onset` A more robust way of setting the onset of EELS edge components, as discussed in article Paper II. `https://github.com/hyperspy/hyperspy/pull/1271`

- `model.Gaussian2D` Adding support for non-symmetrical 2D Gaussians, used heavily in Paper IV to model the atomic columns. `https://github.com/hyperspy/hyperspy/pull/1241`

There are also some contributions not directly related to HyperSpy:

[1] `https://github.com/hyperspy/hyperspy/commits?author=magnunor`

- Improving the scale bar of Matplotlib, which is the standard plotting library for scientific Python: https://github.com/matplotlib/matplotlib/blob/master/lib/mpl_toolkits/axes_grid1/anchored_artists.py#L228
- A Python utility script for plotting the position of detectors in a TEM: https://github.com/magnunor/camera_aperture_position

I have also contributed 26 EEL spectra to the open data repository EELS DataBase https://eelsdb.eu/:

- https://eelsdb.eu/author/magnus/

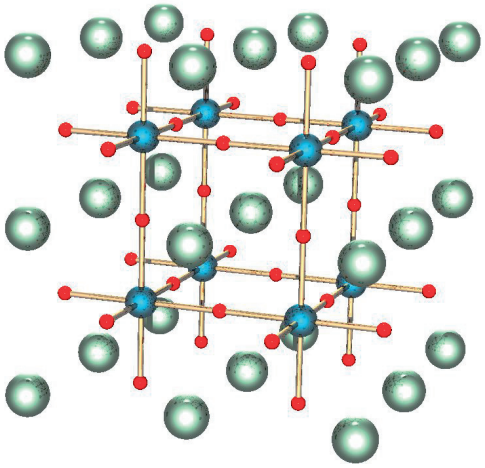

Figure 2.7: The perovskite oxide structure, with the chemical formula ABO_3. The green atoms (A) are metal cations. The blue atoms (B) are metal cations. The red atoms (O) are oxygen. Image from Wikipedia[2].

2.2 Perovskite oxide heterostructures

The perovskite oxides are a promising and important class of functional materials. Even though the perovskite oxide materials family share the same basic structure, there is the vast range of different functional properties. These properties range from ferroelectricity[3], multiferroicity[5], ferromagnetism[4] and colossal magnetoresistance[4]. This large variety of properties is in part due to a strong structure-function coupling, where small changes in structural parameters can result in large changes in functional properties.

Note, all crystallographic directions are given in the pseudocubic coordinate system.

2.2.1 Basic structure

An ideal perovskite oxide has the chemical formula ABO_3, and the cubic space group $Pm\bar{3}m$. Where A and B are metal cations, and O is oxygen. The A atoms are at the corner position (0,0,0), the B atoms are at the center position (0.5,0.5,0.5), while the O atoms are at center of the cube faces. This structure is shown in Figure 2.7. $SrTiO_3$ and $CaTiO_3$[47] are two examples of perovskite oxides materials.

[2] `http://en.wikipedia.org/wiki/File:Perovskite.jpg`

Due to the difference in electron affinity and size of the A and B cations, the perovskite structure often deviate from the cubic form[48]. Goldschmidt formulated an equation to predict the structure in the low symmetry (low temperature) phase, given by the sizes of the cations and oxygen. This Goldschmidt tolerance factor, t, is given by,

$$t = \frac{R_A + R_O}{\sqrt{2}\,(R_B + R_O)}.$$

where R_A is the ionic radius for the A cation, R_O for the oxygen and R_B for the B cation. A t smaller than 1 gives the most common low-symmetry phase for perovskites[49]: rhombohedral- or orthorhombic-structure. A t larger than 1 can give the tetragonal structure. A $t \approx 1$ can get the ideal cubic perovskite structure, such as $SrTiO_3$.

2.2.2 Tuning parameters: functional properties

Of special interest are epitaxially grown thin films of these materials. The interfaces between the substrate and thin film can affect the functional properties of the whole system, leading to exotic phases at the interface or greatly changing the bulk properties. Some transition metals, such as Fe and Mn, commonly have partly filled 3d orbitals and several possible oxidation states. This makes them interesting as B-cations in perovskite systems, due to the added flexibility in orbital structure.

The following examples show some of the ways the properties in these kinds of materials systems can be controlled, giving a very large set of control parameters. Potentially, this large parameter space enables tailor-making of devices, enabled by fine tuning of functional properties. However, due to the strongly correlated nature of the electron states, the properties are very hard to predict theoretically[50].

Epitaxial heterostructures

One way of taking advantage of the strong structure-function coupling is by growing epitaxial perovskite-perovskite heterostructures, which lock the in-plane lattice size of the film to the substrate through substrate clamping. This form of interface engineering has become an interesting research avenue, as it allows for tuning of properties through careful selection of substrate material. It has been enabled by recent advances in synthesis methods such as Molecular Beam Epitaxy and Pulsed Laser Deposition, where epitaxial growth can be controlled down to single monolayers[3, 7].

An example of this is the induction of ferroelectricity in STO by substrate clamping. Bulk STO is cubic and paraelectric down to 0 K, however STO can be

made ferroelectric by growing it on a substrate[51]. This is achieved by carefully selecting an appropriate substrate, where the mismatch between the bulk STO lattice parameter and the substrate can induce ferroelectricity in different directions. Growing STO (3.905 Å) on the orthorhombic (110) surface of $DyScO_3$ (3.944 Å) leads to an in-plane tensile lattice mismatch of 1.0%. This tensile strain leads to an in-plane ferroelectric polarization in the STO film[51]. Using a $(LaAlO_3)_{0.29}\times(SrAl_{0.5}Ta_{0.5}O_3)_{0.71}$ (LSAT) (3.869 Å) substrate gives an in-plane compressive lattice mismatch of -0.9%, and therefore an out-of-plane ferroelectric polarization. Another tuning parameter in heterostructures is the substrate orientation. To illustrate this importance, $SrTiO_3$ (100) atomic planes are neutral, while the (111) atomic planes are not[6]. This give rise to alternating net charges in the <111> directions, potentially leading to reconstructions at heterostructure interfaces[6, 52]. In addition, in (111)-heterostructures, three corners of the oxygen octahedron will couple across the interface, potentially leading to stronger structural coupling[6].

Another way of controlling the structure is by growing the thin film on a "miscut" substrate. Instead of growing the thin film on a flat (001)-oriented $SrTiO_3$ substrate, the thin film can be grown on a substrate which is miscut relative to one of the other zone axes. This miscut leads to the creation of "steps" or "terraces" in the substrate, and can influence what kinds of domains are formed in the thin film. By varying the miscut angles the size of the steps can be controlled, which will affect the domain formation. Nagarajan et al. managed to control the orientation in an epitaxial $PbZr_{0.2}Ti_{0.8}O_3$ thin film grown on a miscut $SrTiO_3$ substrate[53]. The mechanism is believed to be due to relaxation of microstress at the step edges. However, it is noted that having a step size in the same order of magnitude as the film thickness is necessary to control the domain formation in this fashion[53].

Electronic reconstruction

Another way of altering the properties of perovskite oxide heterostructures is electronic reconstructions[54]. Here, the orbitals at the interface can change dramatically, generating novel phases. Thin $LaAlO_3$ (LAO) films grown on STO turned out to have a conductive interface, even though both materials are insulators[35]. The new interface phase is due to the polar catastrophe, where combining the non-polar STO and polar LAO leads to a diverging electric field which must be compensated somehow. By transferring electrons from the surface of the LAO film to the Ti at the interface, the oxidation state of Ti is changed from +4 to +3 leading to conduction at the interface layer [35].

More recently, ferromagnetic ordering has been observed in the Ti^{3+} at this interface by using element-specific techniques such as X-ray absorption spectroscopy

(XAS) and X-ray magnetic circular dichroism (XMCD)[55]. Neither STO nor LAO in bulk form exhibit this ordering, showing how electronic reconstructions can create new interfacial phases.

Chemical substitutions

The perovskite oxides also readily accept chemical substitutions, allowing heavy degree of doping. One well-known example is the doping of $La_{1-x}Sr_xMnO_3$, which both alter the structure and the functional properties. $SrMnO_3$ (x = 1) is hexagonal, insulating and paramagnetic at room-temperature. $LaMnO_3$ (x = 0) is orthorhombic, insulating and paramagnetic at room-temperature. $La_{0.7}Sr_{0.3}MnO_3$ (LSMO) is ferromagnetic at room-temperature and exhibits the colossal magnetoresistance effect, making it a candidate for spintronic devices[56]. Chemical substitution was utilized by Lee et al. which grew several $La_{0.7}Sr_{0.3}MnO_3/La_{1-x}Sr_xMnO_3$ (1 unit cell)/STO heterostructures with varying degrees of x-doping in the one unit cell at the interface[57]. Using DFT-calculations in co-junction with synchrotron based techniques (XAS, XMCD) they found changes in the Mn^{3+} and Mn^{4+} concentrations for the different Sr-doping. Interestingly, a high degree of Sr-doping (x=0.67) at the interface made the thin LSMO films behave similarly as thicker LSMO films.

For a more thorough treatment on the many ways of changing the functional properties see the book *Multifunctional oxide heterostructures*[58].

2.2.3 Pulsed Laser Deposition

All material samples in this project were grown by using Pulsed Laser Deposition (PLD), and this section will therefore give a brief introduction to this deposition technique. The book *Pulsed laser deposition of thin films: applications-led growth of functional materials* by Robert Eason[59] is a good source for a more thorough review. For specifics on PLD growth of $La_{1-x}Sr_xMnO_3$ see the work by Sayani Majumdar *et al.* [60].

With PLD, a high degree of control over thin film synthesis can be obtained. This is achieved thanks to sub-monolayer control of the deposition process, due to fine control of the laser pulses. This gives the possibility of making the high quality epitaxial thin film systems studied in this thesis, with a high degree of stoichiometric control. An example of this is seen in Figure 2.6, which shows a $La_{0.7}Sr_{0.3}MnO_3$ film grown coherently on a (111)-oriented $SrTiO_3$ substrate.

The PLD works by firing a laser in short pulses onto the material which is to be deposited, called the target material. This creates a plasma plume of the target material, which impinges on a heated substrate. The deposition can be done

in both ultrahigh vacuum and background pressure. This makes the technique versatile for a large range of materials.

Some important parameters are the surface temperature, target to substrate distance, the substrate surface quality, energy and frequency of the laser, substrate orientation and oxygen pressure. Substrate orientation is of special interest in this work, since most of the films studied were grown on (111)-oriented $SrTiO_3$[6].

As mentioned earlier, having in-situ monitoring of the film growth is important for making high quality films. One common way of doing this is reflection high-energy electron diffraction (RHEED)[61]. Here, the surface layer of a material is characterized using 10-30keV electrons coming in at a very small angle compared to the sample surface. These electrons interact with the sample surface, giving a diffraction pattern in the detector plane. This diffraction pattern can then be used to characterize the roughness of the surface, which for example can be used to determine if the growth is 2- or 3-dimensional. In addition, RHEED can be used to determine the thickness of the deposited material[61].

2.3 Sample preparation

An important aspect of any work relying on Transmission Electron Microscopy is the sample preparation. This project is no exception, and much time has been spent on optimizing techniques for making good TEM-lamellas.

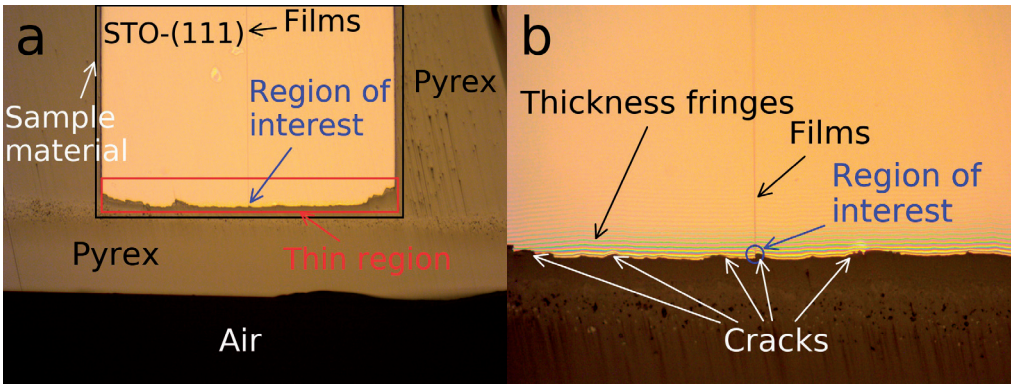

Figure 2.8: Result of mechanical wedge polishing of a $SrTiO_3$ substrate cross section sample, showing extensive cracking in the thin regions. (a) Overview, with the sample glued to pyrex. Showing the major features of the sample, with two pieces of the sample material glued together. The films are glued facing eachother, and viewed edge-on here. (b) Higher zoom, showing the extensive cracking especially in the region of interest.

Two different $SrTiO_3$-substrate orientations were studied: (001) and (111). With the (001)-substrates it was possible to make high quality cross section TEM-lamellas using mechanical wedge polishing (tripod). The method is outlined in the master thesis by Emil Christiansen[62]. However, mechanical wedge polishing did not work very well with the (111)-substrates. This is seen in Fig. 2.8, which shows the result of mechanical wedge polishing of a $SrTiO_3$-(111) substrate after the final polish. When the wedges got too thin, they started cracking, and this seemed to especially happen at the region of interest. This made it almost impossible to make high quality cross section TEM-lamellas. Therefore, the best way of making cross section TEM-lamellas of (111)-substrates was found to be using a dual beam Focused Ion Beam (FIB). This yielded very high quality TEM-lamellas, enabling the work in Paper II-V. An example of such a cross section TEM-lamella is shown in Fig. 2.9.

Although high quality STO-(111) cross section samples proved impossible to make using mechanical wedge polishing, plane view samples worked out much better. Both the tripod and the FIB were used. Firstly the bulk of the material was thinned using the tripod, then the final thinning was performed using the FIB.

None of these results on the plane view samples are included in this thesis, but the results are included in Emil Christiansen's master thesis[62] and an article by the same author[63]. This work was performed on $LaFeO_3/SrTiO_3$-(111) samples, however this sample preparation method should be applicable to similar systems, like $La_{0.7}Sr_{0.3}MnO_3/SrTiO_3$-(111).

A recipe which produced repeatably high quality cross section lamellas for (111)-substrates is included in part IV: appendix.

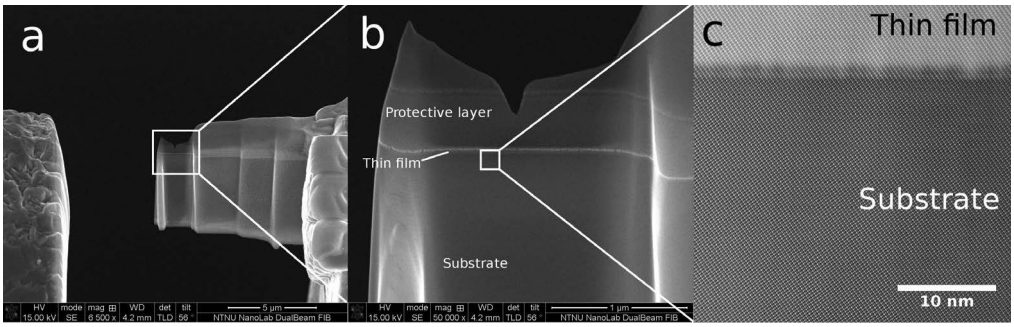

Figure 2.9: Result of making a cross section $La_{0.7}Sr_{0.3}MnO_3/SrTiO_3$-(111) TEM sample using a dual beam Focused Ion Beam (FIB). See appendix IV for details on how it was made. (a) Overview imaging using the electron beam in the FIB, showing the "staircase" sample material in the middle, and the copper TEM grid to the left and right. (b) Close-up of the thinnest region of the sample using the electron beam in the FIB, showing various protective layers and sample materials. (c) STEM-HAADF image using the ARM200CF, showing the atomic structure of the sample material.

Chapter 3

STEM-EELS analysis of perovskite oxides

This chapter will discuss different data processing methods used to study atomic resolution STEM-images and STEM-EELS data from perovskite oxide heterostructures. An overview over the different methods will be outlined, and advantages and disadvantages discussed.

This chapter assumes extensive knowledge about STEM, EELS and the data processing methods associated with these techniques. For a more general introduction to these subjects see Section 2.1, *Electron Energy-Loss Spectroscopy in the Electron Microscope* by Egerton[27] and *Transmission Electron Microscopy* by Williams and Carter[11].

3.1 EELS data analysis

The analysis of EELS data from transition metal oxides is complex, and identification of variables such as oxidation state is largely based on comparisons with standards with known properties. One reason for the complexity is the complicated shape of the core loss edges, and the non-trivial task in simulating them. This section will in detail discuss the current status of advanced data processing for EELS of transition metal oxides.

As mentioned in Section 2.1.2, it is possible to examine the chemical, orbital and electronic structure using EELS. Several aspects of the material can be probed, including the oxidation state of the transition metal B-cations and oxygen stoichiometry. The oxidation state is very important for the functional properties of many of the perovskite oxide materials. For example, $SrTiO_3$ is normally insulating, but if a certain amount of oxygen is removed it becomes conducting, due to

the titanium oxidation state shifting from +4 to +3[64]. $La_{0.7}Sr_{0.3}MnO_3$ exhibits double exchange mediated ferromagnetism due to the mixed oxidation state in Mn, but if the Mn-oxidation state is lowered this effect disappears[58]. One way to lower the Mn-oxidation state is by introducing oxygen vacancies, which cause the Mn oxidation state to become lower. Thus being able to detect the presence of oxygen vacancies in the perovskite oxides is important.

As vacancies often come in the form of point defects, they are usually very hard to image directly[1]. Thus, detecting oxygen vacancies in perovskite oxides is often done indirectly. One example of this is by Muller *et al.*[19], which grew $SrTiO_{3-\delta}$ thin films with varying degrees of oxygen deficiency (δ). To characterize the oxygen vacancies, they used several indicators. i) STEM low angle annular dark field (LAADF) intensity, which shows oxygen vacancy contrast due to de-channeling effects. Using the STEM-LAADF imaging has several advantages, as it has a much higher signal-to-noise ratio compared to the EELS techniques. However, the oxygen sensitivity using LAADF is limited by many factors affecting the LAADF intensity: for example variations in the surface layer and carbon contamination. ii) Oxygen-K edge core loss EELS. The shape of the O-K edge changes quite drastically when oxygen vacancies are present, so using this edge as an indicator for oxygen vacancies is straight forward. iii) Core loss EELS, by examining the titanium $L_{2,3}$ edge, which is sensitive to the local coordination and the Ti-oxidation state. Since the Ti-$L_{2,3}$ edge is sensitive to changes in the oxidation state, it is also an effective way of inferring the amount of oxygen vacancies. Due to local charge neutrality, removing oxygen will lead to electrons being transferred to the titanium. This leads to a shift from Ti^{4+} to Ti^{3+}, which causes large changes in the Ti-$L_{2,3}$. In addition, the Ti-$L_{2,3}$ edge is much more intense compared to the O-K edge, giving it better signal-to-noise ratio. Due to this higher signal-to-noise ratio, the Ti-$L_{2,3}$ could be used to detect $\approx \delta = 0.05$.

Nakagawa *et al.* used STEM-EELS to examine the $LaAlO_3/SrTiO_3$-(001) interface, where the $SrTiO_3$ had either a TiO or SrO_2 termination[35]. Other work had already established that with TiO termination, a conducting layer appeared at the $LaAlO_3/SrTiO_3$ interface[65]. With the SrO_2 termination, this conducting layer was not present. Using the O-K edge they could determine the presence of oxygen vacancies, and using the Ti-$L_{2,3}$ edge they could determine the oxidation state of the titanium. With the TiO terminated sample, a clear Ti^{3+} signal and a small amount of oxygen vacancies were observed at the $SrTiO_3$ side of the interface. On the SrO_2 terminated sample, they observed a significant accumulation of oxygen vacancies at the interface and very little signal from Ti^{3+}. The presence of the conducting layer in the TiO terminated layer could therefore be explained as a compensation of the polar catastrophe: $LaAlO_3$-(001) has polar atomic planes,

[1] An exception to this is 2-D materials like graphene

and growing it on the non-polar $SrTiO_3$ introduces a diverging electric potential[35]. This diverging potential must be compensated somehow. With the TiO terminated $SrTiO_3$, this can be compensated by transferring half an electron to the last layer in $SrTiO_3$. This leads to a shift from Ti^{4+} (bulk $SrTiO_3$) to Ti^{3+} which is conductive. In the SrO_2 termination case, the polar catastrophe is compensated by introducing oxygen vacancies which have a positive charge[35].

For the articles discussed above, the data analysis of the EEL spectra has consisted of removal of the power law background, followed by fitting of a linear combination of reference spectra[19, 35]. Using the reference spectra can be very robust, especially if the signal-to-noise ratio is low. However, it has several requirements, the most important is that the reference spectra have to be obtained. Secondly, the method is limited by the reference spectra which one got. One could use the residual of the fitting to see if any unknown spectra are present in the data. However, if the unknown signal is sufficiently similar to one of the reference spectra, a linear combination of the reference spectra might "hide" the unknown signal. In addition, the reference spectra should optimally be from samples with the same thickness, since plural scattering can affect the shape of the edges. These thickness effects can be removed by deconvolving with the low loss spectra, however this can also introduce artifacts[27]. Another way of processing EELS data is by a simple integration of the intensity[66], after subtracting the power law background. This method is also robust, since it simply counts up the intensity across a certain range. However, this potentially discards useful information like the shape of the fine structure edges.

More information can be extracted by using the model based approach[37], which works by constructing a model consisting of several components and then fitting this model to the experimental data. The challenge then becomes finding the right components to include in the model. These components cover different aspects of the experimental data: power law for the background[37], Hartree-Slater cross sections for the ionization edges[67] and Lorentzian or Gaussian distributions for the fine structure[37]. The components have several parameters, like a 1-dimensional Gaussian having amplitude, sigma (σ) and center position. Thus, it is possible to quantify more of the data contained with these rich spectra. One disadvantage with the model based approach is the necessity for clearly resolved edges if one wants to fit many different components to the signal. For example, trying to fit 7 separate components with 19 parameters all together to an experimental signal requires some clever processing steps. So making sure the model fits nicely to the experimental data, requires quite a lot of careful consideration in picking sensible initial values and fitting bounds. If available, the model can also be convolved with the low loss spectra. This has several advantages: it takes into account plural scattering, and gives a better fit to the experimental data.

Riedl and coauthors[68] examined a variety of methods for estimating the Mn-$L_{2,3}$ intensity ratio. This included: i) The ratio of the max intensity for L_3 and L_2. ii) Fitting a step edge at the max intensity point for both L_3 and L_2, then taking the ratio of the remaining intensity in the L_3 and L_2. iii) Curve fitting using two Hartree-Slater cross sections for the L_3 and L_2 continuum backgrounds, and one Gaussian distribution for each of the L_3 and L_2 fine structure peaks. iv) Setting the L_3 Hartree-Slater onset to the position of 10% of the L_3 peak; L_2 to the point of minimum intensity between the $L_{2,3}$ peaks; fit the amplitude of the Hartree-Slater cross sections using a region between 50 to 100 eV after the L_3 peak; take the ratio of the intensity between the L_3 and L_2 peaks. Comparing these methods, they found the iv) method to be the most sensitive and has the least noise. One possible reason for the curve fitting in iii) performing worse could be the L_3 and L_2 not being properly constrained as in iv). The lack of constrains could lead to the amplitude in the Gaussians varying due to the Hartree-Slater cross sections "eating up" the experimental intensity. In addition, in only using the amplitude of the Gaussians, the potentially important information in the σ and center position is unused. Thus, there are some avenues for improving the curve fitting method explained here[68]. This is considered in Paper II.

Varela *et al.* studied systematically the EELS fine structure $La_xCa_{1-x}MnO_3$ with x from 0 to 1[29]. Using these samples with known oxidation state, they examined how the EELS fine structure changed as a function of oxidation states. Three different Mn-oxidation state indicators were examined: i) Mn-$L_{2,3}$ ratio, by fitting Hartree-Slater cross sections to the continuum background, and integrating up the intensity in the L_3 and L_2 peaks. ii) Fitting one Gaussian to the oxygen-K prepeak and another Gaussian to the main peak, then taking the ratio between the area under the two Gaussians. iii) Energy separation between the oxygen-K prepeak and main peak, using the center position of the same Gaussians as above. All methods were found to be sensitive to the Mn-oxidation state, however method iii) was found to be the most sensitive and with the smallest error bars. The same was also noted by Rield and coauthors[69]. However, one disadvantage with using the oxygen K-edge is the potentially large variations, especially when there are large amounts of oxygen vacancies. For example, in Paper I the O-K prepeak disappeared completely due to high concentrations of oxygen vacancies. This made it impossible to get a proper Gaussian fit to the O-K prepeak. This was not the case for the Mn-$L_{2,3}$, which still retained its general shape. In addition, they tested all three methods as a function of sample thickness from 0 to 1 t/λ. Both the oxygen energy separation and the oxygen ratio methods were within error bars over the thickness range. The Mn-$L_{2,3}$ ratio was within error bars for most of the thickness series, except towards the thicker regions at 1 t/λ.

Similar work on a variety of transition metal oxides was done by Tan *et al.*,

who examined two different ways of extracting the oxidation states: L_3 edge onset and $L_{2,3}$ ratio[31]. Using the edge onset requires an accurate calibration of the energy scale, however there are many factors which can cause an energy shift. To account for this, they used a script which acquired the core loss and zero loss peak serially, meaning the absolute energy scale could be properly calibrated[2]. This method was used to acquire EEL spectra from a wide range of V, Mn and Fe based oxides with known oxidation states. The $L_{2,3}$-ratio was extracted similarly to method iv) in Riedl *et al.*[68], but using Hartree-Slater cross sections for the core loss edges and a smaller integration window (8 eV) was used for the L_2 and L_3 peaks. The edge onset was set as 10% of the net intensity of the L_3 peak. They found the edge onset (chemical shift) method to be more robust as an indicator for oxidation state than the $L_{2,3}$ ratio, due to higher precision and not being sensitive to thickness changes. As also noted by Varela[29], the ratio method was also sensitive to changes in the sample thickness. However, for Tan[31], the effect of thickness on the $L_{2,3}$ ratio was much larger. This thickness sensitivity can be tackled by deconvolution with the low loss spectrum, however this can introduce artifacts in the core loss spectrum. One limitation with the edge onset is materials with mixed oxidation state. If a material consists of 50/50 Mn^{2+} and Mn^{3+}, the method would only detect the edge onset of the Mn^{2+} due to this being at a lower energy loss. In this case, using the model based approach with fitting each peak with a Gaussian, it could be possible to pick out the presence of a mixed oxidation state. This is due to the L_3 peak becoming wider, which would be noticeable in the σ parameter. In addition, the L_3 onset would shift towards lower energy loss. This is discussed in Paper II, section 2.2.

A general comment on using absolute energy for determining oxidation states, is that the absolute energy scale can vary between instruments due to slight differences in spectrometer calibrations. This can also vary on the same instrument between different energy dispersion settings. In my anecdotal experience, using the absolute energy from other studies is therefore risky, due to these slightly varying settings. Of course, this can probably be fixed by a more rigorous calibration regime. Secondly, the DualEELS capability on the GIF Quantum ER is limited to energy jumps of 2000 eV. This means it can be problematic to acquire the zero loss peak for calibration when working on core loss edges over 2000 eV. However, one possible solution is using some other feature with known energy for calibration.

To summarize this review of data processing of core loss transition metal oxides: there are no general methods which work well for even the same element in different structures. This is due to the complex shape of these experimental core loss spectra, coupled with the difficulty of simulating EEL spectra for these strongly correlated electron structures. This again makes it hard to directly compare lit-

[2]In newer EEL spectrometers by Gatan, this is included in the DualEELS functionality.

erature values, making it necessary to focus on the general trends (like $L_{2,3}$-ratio) instead of specific numbers. Thus, this necessitates the need for different processes and methods for analyzing EELS fine structure data.

3.2 Structural characterization

With the advent of probe corrected STEM, characterizing the atomic structure of materials has become routine. Due to the strong function-structure coupling in the perovskite oxides, there are several types of structural distortions which are of interest: oxygen octahedron tilt patterns, oxygen octahedron deformations and cation displacements. The latter is perhaps the easiest to characterize, since the cations can routinely be imaged using STEM-HAADF. An example of this is B-cation displacement in ferroelectrics, which can be used to estimate the local polarization[70].

The oxygen octahedron tilt pattern can affect properties such as electron hopping and therefore influence the conductivity[58]. Deformations, like elongation or compression, of the oxygen octahedron can lead to splitting of the B-cation energy levels[50]. This can then promote different types of spin ordering, leading to for example different types of antiferromagnetic orderings[58]. Thus being able to directly image these kinds of structural distortions is important, as it allows the macroscopic functional properties to be explained. This section will cover the state of the art of measuring the displacements and distortions in all the sub-lattices present in the perovskite oxide structure: A-cations, B-cations and especially the oxygen atomic columns since historically they've been the hardest to image. The focus will be on the methods used to extract the structural information, as this has been one of the themes in this thesis, as seen in Paper IV.

As discussed earlier in section 3.1, oxygen vacancies are often characterized using EELS. These vacancies often come in the form of individual point defects, which are hard to image directly. However, these oxygen vacancies can also order into specific atomic planes. This was examined by Ferguson *et al.*[71], which used a $SrTiO_3$ oxygen getter layer grown epitaxially on top of a $La_{0.7}Sr_{0.3}MnO_3/SrTiO_3$-(001) substrate. Here, the presence of ordered oxygen vacancies in the structure is visualized directly in the HAADF contrast. This contrast is seen as alternating bands of lower intensity in every second perovskite unit cell in the out-of-plane growth direction ([001]-direction). The reason for this is the oxygen vacancies ordering into these darker planes (Figure 3.1), turning the oxygen octahedra into tetragons, and increasing the distance between these layers. Thus, the dark layer originates from the A-cations being further away from each other, not the lower amount of oxygen content directly[72]. This structure is called a brownmillerite phase, which is associated with oxygen vacancy ordering in a perovskite lattice.

A similar study was performed by Gazques *et al.*[72], where they grew oxygen deficient epitaxial $La_{0.5}Sr_{0.5}CoO_{3-\delta}$ (LSCO) thin films on a variety of substrates: $SrTiO_3$-(001), $SrTiO_3$-(110) and $LaAlO_3$-(001). Here, the oxygen vacancies ordered into similar brownmillerite structures as seen by Ferguson *et al.*[71], how-

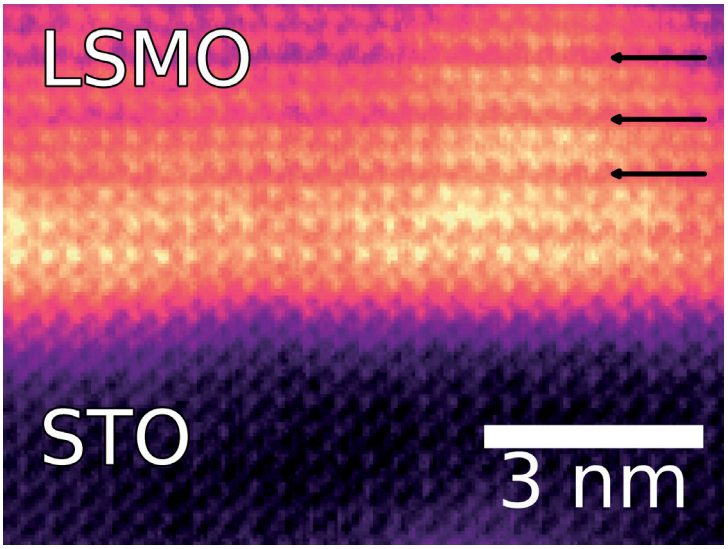

Figure 3.1: Atomic resolution STEM-HAADF image of a brownmillerite structure in an LSMO thin film grown on an STO-(001) substrate.

ever the direction of the ordering depended on the misfit strain with the substrate. For the $SrTiO_3$-(001), the LSCO film was tensile strained (-1.8%). To relieve this strain, the oxygen deficient layers are oriented parallel to the growth direction. Since these layers are larger, they effectively reduce the tensile strain from the substrate. For the $LaAlO_3$-(001) substrate, the LSCO film was compressively strained (1.3%). Here, the oxygen deficient layers are oriented perpendicular to the growth direction, leading to an in-plane compression. By using GPA[38] they could map the amount of both in-plane and out-of-plane strain, giving an image of how the strain was accommodated through ordering of oxygen vacancies[72].

While Fourier based techniques such as GPA is relatively fast and fairly robust, they also have some drawbacks. The main one being the limited spatial resolution, which is limited to about 1 unit cell[39] when using large masks in Fourier space. There is also the risk of artifacts[39, 73], especially when using the large masks. Note, even if the spatial resolution is limited, the precision of the strain can be within 0.25% (1 pm)[39]. This limited spatial resolution is a problem, since we ideally want to get information about individual atomic columns. One way to do this is by using real space methods, which will be discussed below.

Borisevich *et al.* studied a $BiFeO_3$ (BFO) this film grown on $La_{0.67}Sr_{0.33}MnO_3/SrTiO_3$-(100)[42]. Here, they examined the width of a charged ferroelectric domain wall in the BFO film. The difference between the two domains in the chosen projection, $<110>_{pc}$, was the oxygen octahedral tilt pattern.

This resulted in the oxygen in the shared BiO atomic columns being shifted in relation to the Bi atoms: in one of the domains the oxygen position was shifted in the same direction for every atomic column, while for the other domain with 90 degrees rotation in relation to the Bi-atom in every other atomic column. HAADF is normally used to visualize heavy atoms (often referred to as Z-contrast), but as explained in Section 2.1.2 the HAADF intensity can be influenced by many different factors. Using Bloch wave simulations[74], they established that for a sample thickness above 20 nm the oxygen column was actually visible as an asymmetry in the Bi atomic column. Thus, it is possible to distinguish between the two different domains by quantifying the different Bi atoms shapes. By extracting a region around each atom, principal component analysis (PCA) was performed on all the Bi atom columns. This showed the first component was related to the average shape of the atom columns, while the second was related to the ellipticity. By plotting the weight map for the second component, they could extract information such as the width of the domain walls[42].

He *et al.* used high resolution STEM-ABF to analyse the octahedral tilt patterns in a variety of perovskite oxide heterostructures[43]. By acquiring the STEM data as image stacks, then aligning and summing them in post-processing, datasets with low scanning distortions could be achieved. These datasets could then be used to find the center position of the oxygen columns using center of mass. This could then be used to infer the in-plane octahedron tilt pattern. Similar to the work by Borisevich *et al.*[42], PCA was performed on the images of the oxygen columns. This allowed for information about the shapes of the oxygen columns to be quantified, which was then used to figure out the tilt pattern parallel to the electron beam. By combining the center of mass data with the PCA data, they extracted information about all the oxygen octahedron rotation axes. This allowed for a better understanding of how the oxygen octahedron changed as a function of distance from the heterostructure interface, giving information about the strain relaxation mechanism[43].

Zuo and coauthors used template matching to find the positions of atomic columns in STEM-HAADF images[73]. This method is based on using a sub-image (template) of a repeating structure from the full HAADF image. For example, in an image of Si [110] a good template would be the Si dumbbell[73]. This template is cross correlated with the full image, giving a correlation map which in essence shows where the dumbbells are located. A peak finding routine is then used to find all the peaks in the correlation map, which is further refined using center of mass. These refined peaks can then be used to quantify the strain[73].

iMtools[75] was used by MacLaren *et al.* to examine phase boundaries in La-doped $PbZrO_3$[70]. Similarly to He *et al.*[43], they acquired STEM-HAADF data as an image stack which was summed in post processing to reduce effects

of scanning distortions. Using 2D Gaussian fitting for each atomic column, an average precision of 6-7 pm was achieved for the A- and B-cation atomic columns. This was then used to find the structure of the phase boundary, and the amount of shift in the B-cations was used to quantify the ferroelectric polarization.

Another recent software package using real space fitting is the "oxygen octahedra picker" by Wang et al.[40]. The program works by firstly using center of mass on a region around each B-cation atomic column. Next, the oxygen columns around a B-cation atomic column has to be selected manually, and they are used to find the rest of the oxygen positions. These initial positions are then refined using either center of mass or, if higher precision is wanted, 2D Gaussians.

Being able to map the center positions of the oxygen columns is important, as this can be used to infer the octahedron tilt pattern. This can be done by using center of mass[42]. While this is very robust[76], due to it simply being the intensity weight of an atomic column, a 2D Gaussian least square fitting will provide better precision[40, 76]. Apart from the better precision, the fitting also provides more information in the form of the width of the atomic column. This can be further improved by using an elliptical 2D Gaussian with rotation, which can give both the ellipticity (magnitude and direction), as shown in Paper IV. However, one large drawback with the Gaussian fitting is the risk of fitting failure, and the higher computational cost[76]. The former can be offset by setting reasonable initial values, and checking if the fitting results fall within certain limits. The latter can also be improved setting reasonable initial values, but the increased computational time will always be an issue. However, when doing the fitting in post processing this does not matter that much[3]. Thus, several software packages use 2D Gaussians, often with center of mass to get initial values[40, 76].

An alternative to the 2D Gaussian fitting is the template matching method used by Zuo[73], since it does not require the atomic columns to conform to the shape of a Gaussian. Thus, one can choose the template to be several atoms, or a whole unit cell. One example of this is the Si [110] dumbbell. With a sufficiently thin TEM-sample and well-aligned aberration corrected instrument it is normally easy to resolve the individual atom columns in a dumbbell, which makes it easy to do a 2D Gaussian fitting on each of them. However, if there is a large overlap between the atoms, trying to fit two 2D Gaussian could be difficult. In such a situation, template matching would be a much easier solution, due to the reduced risk of fitting failure. This is also relevant for perovskite oxides, especially if one use one of the "non-optimal" projections, where the atomic separation is low.

As shown by He *et al.*[43] the shapes of the oxygen columns can contain useful information. It should therefore be possible to extract similar information by

[3]Very large datasets processed using Atomap (Paper IV) used about 1 hour. Typical datasets shown in Paper IV used about 5-10 minutes.

fitting 2D Gaussians to the oxygen columns. The center positions of the oxygen columns are easy obtain (as seen in Paper IV), however the shape is more of a challenge. In these cases using PCA on the oxygen columns[43] could be better way of getting this shape information.

One factor which has not been discussed, is the software implementations themselves. For example, iMtools is implemented in the proprietary IDL programming language, which needs to be purchased. Versions of Windows newer than Windows XP may not be compatible with iMtools[75]. This reduces the availability of the software. In addition, the source code is not available under an open source license, making it harder to continue further development if the original creators abandons the project. A further risk in this specific case is the proprietary IDL language, since one is reliant on the company actually continuing supporting it.

Thus, the software implementations of these methods should by accessible under an open source license[44], since it allows other researchers to pick up an abandoned project. This also greatly increases reproducibility and impact, since researchers can, i) test the code to make sure bugs do not influence the results, and ii) improve the original code by contributing[46].

3.3 Opportunities and challenges

The aberration corrected instruments have enabled acquisition of high resolution STEM and EELS data. The challenge has become the microscope scanning distortions, which in practice limits the precision of the structural data that can be extracted. Luckily, much work has been done recently on addressing the scanning distortion issues, allowing for this high resolution data to be utilized to its fullest. This involves acquiring the STEM image data as image stacks with faster pixel dwell times, where the image stack is corrected using non-rigid registration and averaged in post processing[16].

Having acquired high quality datasets, the challenge then becomes quantifying them. There is a need for robust real space analysis tools which can extract both the position and shapes of individual atomic columns with high precision. This is needed so the fine structural details in the perovskite oxide heterostructure interfaces can be characterized, and better understand novel functional properties. These tools, and their source code, should be available to the wider community, so the algorithms can be checked for errors and improved by the microscopy community.

The increasing availability of low-energy spread and high brightness CFEG STEMs, has allowed for good signal-to-noise ratio acquisition of high energy resolution EELS data. For the perovskite oxides, this has enabled a greater insight into the various forms of electronic and orbital reconstructions which can occur at

the interfaces of these materials.

The challenge here consist of developing better data analysis routines, which can both extract the rich information contained in this data type, and also allow for easier comparison of results between different research groups.

Part II

Papers

Paper I

Structural phases driven by oxygen vacancies at the $La_{0.7}Sr_{0.3}MnO_3/SrTiO_3$ hetero-interface

M. Nord, P. E. Vullum, M. Moreau, J. E. Boschker, S. M. Selbach, R. Holmestad, and T. Tybell

Applied Physics Letters, 106, 041604 (2015)

APPLIED PHYSICS LETTERS **106**, 041604 (2015)

Structural phases driven by oxygen vacancies at the $La_{0.7}Sr_{0.3}MnO_3/SrTiO_3$ hetero-interface

M. Nord,[1] P. E. Vullum,[1,2] M. Moreau,[3] J. E. Boschker,[3] S. M. Selbach,[4] R. Holmestad,[1] and T. Tybell[3,a)]
[1]*Department of Physics, NTNU, 7491 Trondheim, Norway*
[2]*Materials and Chemistry, SINTEF, 7465 Trondheim, Norway*
[3]*Department of Electronics and Telecommunications, NTNU, 7491 Trondheim, Norway*
[4]*Department of Materials Science and Engineering, NTNU, 7491 Trondheim, Norway*

(Received 12 October 2014; accepted 17 January 2015; published online 29 January 2015)

An oxygen vacancy driven structural response at the epitaxial interface between $La_{0.7}Sr_{0.3}MnO_3$ films and $SrTiO_3$ substrates is reported. A combined scanning transmission electron microscopy and electron energy loss spectroscopy study reveal the presence of an elongated out-of-plane lattice parameter, coupled to oxygen vacancies and reduced manganese oxidation state at the $La_{0.7}Sr_{0.3}MnO_3$ side of the interface. Density functional theory calculations support that the measured interface structure is a disordered oxygen deficient brownmillerite structure. The effect of oxygen vacancy mobility is assessed, revealing an ordering of the vacancies with time. © *2015 AIP Publishing LLC*. [http://dx.doi.org/10.1063/1.4906920]

Perovskite oxide materials exhibit interesting magnetic, electric, dielectric, and piezoelectric properties, which make them a promising and important class of functional materials. For example, $La_{0.7}Sr_{0.3}MnO_3$ (LSMO) is a mixed-valence system where the interplay between Mn^{+3} and Mn^{+4} gives properties such as colossal magnetoresistance through double-exchange.[1] In particular, the LSMO/$SrTiO_3$ (STO) heterostructure has been considered a promising system for devices such as magneto-tunneling junctions, metal-based spintronics, and magnetic memory. A recent development is the fabrication of oxygen-poor modulations of the perovskite structure as thin films. Ferguson *et al.*[2] induced oxygen vacancies in LSMO grown on STO, using a top layer of oxygen deficient STO as an oxygen getter. This resulted in a brownmillerite phase, where the oxygen vacancies ordered into a superstructure. Similar structures have also been reported in $La_{0.5}Sr_{0.5}CoO_{3-\delta}$ (LSCO) heterostructures. Growing the LSCO on substrates with different lattice mismatch led to different kinds of oxygen vacancy ordering, driven by strain relief accommodation.[3] These structures are not only interesting for the ionic transport[4] properties but also for their effect on other functional properties. *Ab-initio* calculations predict oxygen vacancies close to the interface of tensilely strained films.[5] There have also been several observations of changes in cation oxidation state[6–8] and lattice parameter[9] close to interfaces in similar systems. Understanding the correlation between oxygen vacancies and B-site cation oxidation state, and how the oxygen vacancies behave and order over time is important for implementation in devices.

In this letter, we report on a combined Scanning Transmission Electron Microscopy-Electron Energy Loss Spectroscopy (STEM-EELS) and Density Functional Theory (DFT) study of a LSMO/STO heterostructure, where a coupling between oxygen vacancies, the manganese oxidation state, and an elongated out-of-plane lattice parameter in the LSMO film close to the interface is observed. We attribute these observations to a brownmillerite structure with disordered oxygen vacancies, which order over time.

35 nm thick epitaxial LSMO films were grown on (001)-oriented STO substrates using pulsed laser deposition and *in-situ* RHEED analysis.[10] The substrates were annealed for 1 h at 950 °C in oxygen ambient before the deposition. A KrF excimer laser ($\lambda = 248$ nm) with a fluency of $\sim 2\,J\,cm^{-2}$ and a repetition rate of 1 Hz was employed on a stoichiometric $La_{0.7}Sr_{0.3}MnO_3$ target.[10] Cross sectional TEM foils were prepared using mechanical tripod wedge polishing followed by low-energy Ar-ion milling. A combined STEM-EELS and STEM-high angle angular dark field (HAADF) study was performed to probe the electronic and lattice structure at the interface using a probe corrected FEI Titan 80–300, with a beam energy of 300 keV. The energy resolution of EELS was found to be 1.0 eV from the full width at half maximum (FWHM) of the zero loss peak. The STEM and EELS study on the ordered brownmillerite after 1.5 years was performed on a probe- and image-corrected cold-FEG Jeol ARM 200F. For the EELS analysis, principal component analysis (PCA)[11] was used to reduce noise and standard power law background subtraction was done using HyperSpy.[12] To increase the electron count statistics, the EELS data were not collected at atomic resolution, but with a larger probe. To rule out the effect of the electron beam inducing changes in the material, the same EELS experiments were performed in similar regions with shorter exposure and at a beam energy of 120 keV, showing the same results as the 300 keV data at 3 s exposure time. In addition, electron beam exposure tests were performed, where the same area was exposed to the electron beam for 30 s under the same experimental conditions as the data in this work. No significant changes in the EELS data were observed. The DFT calculations were done with the Projector Augmented Wave (PAW) method[13] as

a)Author to whom correspondence should be addressed. Electronic mail: thomas.tybell@iet.ntnu.no

implemented in the Vienna *Ab-initio* Simulation Package (VASP),[14,15] using the PBEsol functional[16] with a GGA + U approximation.[17] The La, Sr_sv, Mn_sv, and standard O PBE PAW potentials supplied with VASP were used, and a Hubbard U correction of 3 eV and 10 eV was applied to the Mn 3d electrons and La 4f orbitals, respectively, in concordance with previous related investigations.[5,18] A 36 atom $La_6Sr_2Mn_8O_{20}$ unit cell with a $6 \times 6 \times 2$ gamma centered k-point mesh and a plane wave cutoff energy of 550 eV was used for the calculations of the oxygen deficient LSMO unit cells. The in-plane lattice constants were fixed at the equilibrium calculated value for cubic STO, while the ionic coordinated and out-of-plane lattice constant were allowed to relax until the Hellmann-Feynman forces on the ions were smaller than 0.01 eV/Å.

The structural quality of the thin film and substrate was investigated by STEM-HAADF. Fig. 1(a) shows typical data, revealing a coherent interface, and X-ray analysis confirms that the films are epitaxial.[10]

Possible strain around the epitaxial interface was analyzed relying on geometrical phase analysis (GPA)[19] of the STEM-HAADF data. Fig. 1(a) shows a STEM-HAADF image of the LSMO/STO heterostructure, and the corresponding out-of-plain strain data from GPA is displayed in Fig. 1(b). Using the lattice parameter of bulk STO, 3.905 Å, as a reference, the substrate averages as expected to 0% out-of-plane strain, with a standard deviation of 0.17%. For the film, an elongated out-of-plane lattice parameter is observed in the first 3 nm. This corresponds to a relative out-of-plane strain of 2.5% compared to the LSMO bulk pseudo cubic lattice parameter of 3.876 Å. Similar strain has been reported in BFO grown on LSMO/STO,[9] where the first few unit cells closest to the interface are elongated in the out-of-plane direction.

To further investigate the region with enlarged out-of-plane LSMO lattice parameter, we probe the electronic structure by EELS, providing information on both the manganese and oxygen electronic state through the Mn-$L_{2,3}$ and O-K core loss edges. EELS line scans were acquired in a line orthogonal to the film/substrate interface, as schematically shown in Fig. 2(a), with STEM-EELS data representative for (i) the bulk LSMO film (red), (ii) the interface on the film side (green), and (iii) the bulk STO (blue), presented in Fig. 2(b). The manganese edge consists of two peaks: L_3 (Mn $2P_{3/2} \rightarrow 3d$) and L_2 (Mn $2P_{1/2} \rightarrow 3d$),[11] see Fig. 3(a). There is a clear difference between the Mn-$L_{2,3}$ spectra acquired at the interface and those acquired away from the interface. The intensity ratio between the L_3 and L_2 peaks (L_3/L_2-ratio)

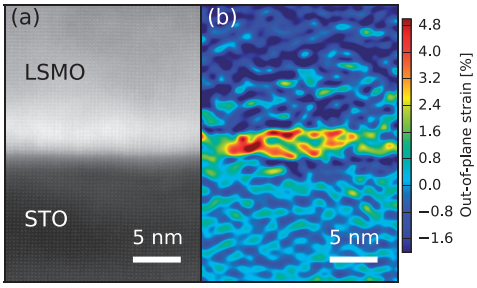

FIG. 1. (a) Cross-sectional STEM-HAADF image of the LSMO/STO heterostructure, showing a coherent interface. (b) Map of the out-of-plane strain in (a), using the STO-substrate (3.905 Å) as a reference.

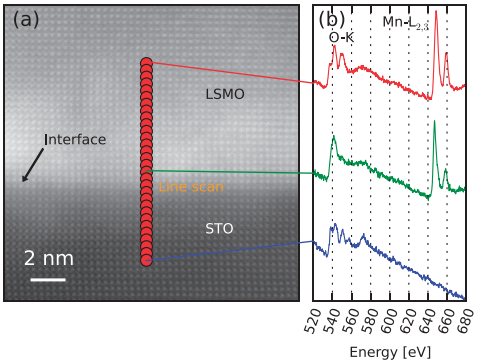

FIG. 2. (a) Cross-sectional STEM-HAADF image of the LSMO/STO heterostructure. (b) Results of an EELS line scan across the LSMO/STO interface.

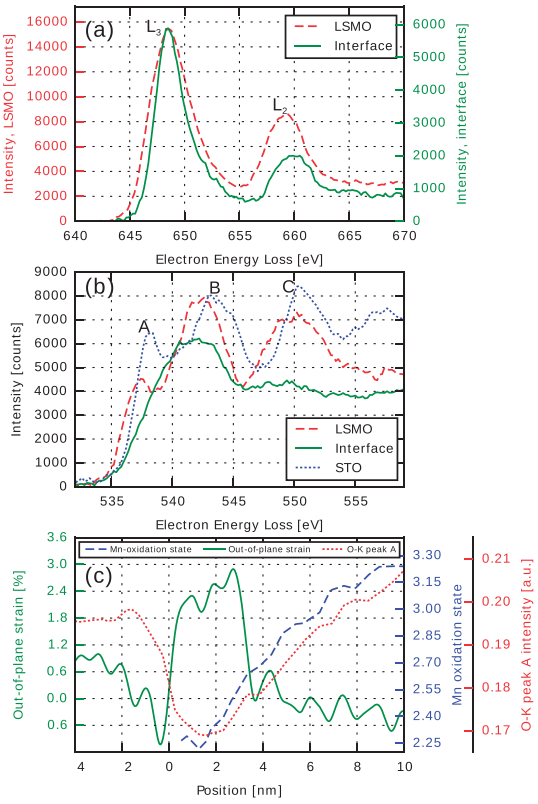

FIG. 3. (a) Manganese L_2- and L_3-edges from the middle of the LSMO film, and LSMO film side of the interface. (b) Oxygen K-edge from the LSMO film side of the interface, in the middle of the LSMO film, and STO substrate. (c) Integrated out-of-plane strain from Fig. 1(b), manganese oxidation state and integrated oxygen K-edge peak A intensity normalized on the total O-K edge intensity (shown in Fig. 3(b)).

is larger at the interface. This is indicative of a lower Mn oxidation state at the interface as compared to bulk LSMO, as the intensity of the L_3 peak increases relative to the L_2 peak when the Mn oxidation state is lowered.[11,20] We note that the FWHM line width of the Mn-L_3 peak is smaller at the interface as compared to the rest of the film, supporting a lower Mn oxidation state at the interface.[20] The Mn-oxidation state was estimated as in Varela *et al.*[11] and plotted in Fig. 3(c) (blue dashed line). As can be seen in Fig. 3(c), a clear trend for the Mn oxidation state was observed: starting at 3.2 far from the interface and monotonically decreasing towards 2.3 close to the interface. This trend of a reduction in Mn oxidation state has also been observed in (La,Ca)MnO_3/STO[6] and $TbMnO_3$/STO,[7] and has been proposed to explain the observed magnetic "dead layer" in similar systems.[21]

In order to investigate the possible presence of oxygen vacancies, known to be present in similar thin film systems,[2] the oxygen electronic structure was investigated. As seen in Fig. 2(b), large spectral differences are observed between the oxygen K-edges across the interface. The oxygen K-edges from the (i) middle of the film, (ii) film side of the interface, and (iii) STO bulk are shown in detail in Fig. 3(b). The main fine structure peaks are labeled as A, B, and C. The O-K edges from the bulk of the film, and the STO substrate, are consistent with LSMO[8] and STO bulk[22] data previously reported. However, the O-K edge at the LSMO side of the interface is not consistent with LSMO bulk. We observe that peak A is weak or not present in the LSMO interface region. Peak A is attributed to the covalent interaction between O 2p and Mn 3d states in the LSMO perovskite structures,[11] and is known to be sensitive to the Mn oxidation state. In addition, a weakening of peaks A and C in conjunction with a broadening of peak B has been correlated with oxygen vacancies.[23] The bond between Mn and O becomes more ionic as the Mn oxidation state decreases, reducing the interaction between the orbitals. A low Mn oxidation state then corresponds to a less intense peak,[11] consistent with the Mn L-edge data. We take the integrated intensity of peak A normalized over the total O-K intensity as a measure of oxygen content, the results of this shown in Fig. 3(c) (red dotted line). As can be seen, the amount of oxygen vacancies increases towards the interface, and subsequently decreases to a constant value in the substrate.

The strain, shift in Mn oxidation state and the changes in oxygen signal imply a deviation from the perovskite structure at the film side of the interface. The formal valence for Mn in $La_{0.7}{}^{+3}$ $Sr_{0.3}{}^{+2}Mn^{+3.3}O_3{}^{-2}$ (valence shown in superscript) is 3.3. Removing oxygen lowers the Mn oxidation state as the charge compensating electrons localize on Mn, consistent with the data. We note that oxygen vacancies can be expected close to the interface in thin films that are tensiled strained by the substrate.[5] Assuming that the whole shift in Mn oxidation state is due to oxygen vacancies, an oxygen deficiency of $\delta = 0.5$ ($LSMO_{3-\delta}$) is found (corresponding to $La_{0.7}Sr_{0.3}MnO_{2.5}$). This amount of oxygen vacancies is also consistent with the oxygen fine structure, which is similar to the one reported by Yao *et al.*[23] This large number of oxygen vacancies breaks the MnO_6 octahedron, and hence, destroys the perovskite structure.[24] A known cation non-stoichiometric phase is the Ruddlesden-Popper structure.[25] However, our high-resolution STEM-HAADF data are not consistent with the clear signature of such a phase. Other cation non-stoichiometries, such as La- or Mn- deficient phases, correspond to an increase in the formal Mn valence, not consistent with our EELS data. A possible reduction in Sr-content would lower the Mn oxidation state, however, this is not consistent with the O-K edge.[26] Therefore, we do not attribute the observed changes to cation non-stoichiometry.

The oxygen deficient brownmillerite structure, $ABO_{2.5}$ is compatible with the experimental data. Recently, there have been several reports on thin film synthesis of brownmillerites in multiple material systems.[2,27–29] For example, a brownmillerite phase, where oxygen vacancies are ordered, was shown in a LSMO/STO heterostructure by Ferguson *et al.*[2] In that work, the vacancies were ordered in preferred layers resulting in an out-of-plane lattice parameter of 16.47 Å, corresponding to four pseudo-cubic LSMO unit cells with a 6.1% elongation of the out-of-plane lattice parameter compared to the stoichiometric perovskite. This is considerably larger than the 2.5% elongation we measure close to the interface in this work. However, one possibility is that disordered oxygen vacancies result in a lower out-of-plane strain state. In order to test this hypothesis, we have performed DFT calculations on brownmillerites with ordered and disordered oxygen vacancy structures. The calculations were performed on structures with different oxygen vacancy positions (see supplementary material[30]), the results shown in Table I. There is a clear trend that structures with oxygen vacancies ordered in layers are more stable than oxygen vacancies distributed in all the Mn layers. The most stable structure, corresponding to the one observed by Ferguson *et al.*,[2] is 0.223 eV/f.u. more stable than the most stable disordered structure. However, the DFT calculations also reveal that the disordered structures all show an elongated out-of-plane lattice parameter in the order of 1%–2%, in good agreement with our experimental strain data, while the ordered structures show an elongation in the order of 6%–7%.

TABLE I. DFT calculated energy differences between the different oxygen vacancy brownmillerite structures and the most stable ordered structure, given per $ABO_{2.5}$ formula unit, and the corresponding out-of-plane strain compared to stoichiometric bulk LSMO. The different structures (A, B, C, and D) referring to different positioning of the oxygen vacancies, see supplementary material[30] for details.

	Ordered structure A	Ordered structure B	Ordered structure C	Disordered structure A	Disordered structure B	Disordered structure C	Disordered structure D
ΔE/f.u. (eV)	0.014	0	0.035	0.304	0.357	0.223	0.238
Strain (%)	6.72	6.52	7.00	2.38	2.39	1.55	2.11

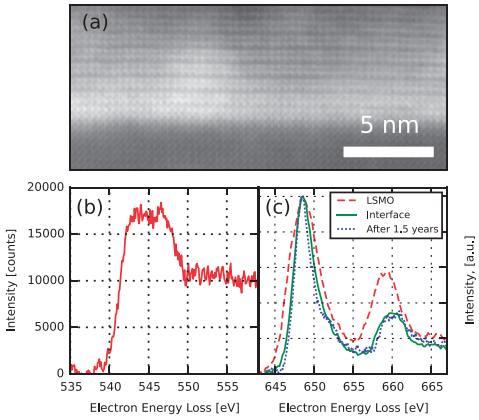

FIG. 4. (a) Cross sectional STEM-HAADF image from the same TEM lamella as Figs. 1(a) and 2(a), after approximately 1.5 years showing an ordered brownmillerite superstructure at the film side of the interface. (b) Representative STEM-EELS data from the superstructure in (a), showing an oxygen K-edge consistent with oxygen vacancies. (c) The same as (b) but for the Mn-$L_{2,3}$ edge, with the spectra from Fig. 3(a) as comparison.

Based on the above discussion, a brownmillerite phase with disordered oxygen vacancies at the LSMO side of the interface towards STO is the only interpretation that agrees with both STEM and EELS data and DFT calculations. Fig. 4(a) shows STEM-HAADF data taken on the same TEM lamellas after approximately 1.5 years. Here, we find an ordered, layered structure at the interface, compatible with an ordered brownmillerite phase.[2] Figs. 4(b) and 4(c) display representative O-K and Mn-$L_{2,3}$ EELS edges from the ordered structure, confirming the presence of oxygen vacancies and manganese oxidation state corresponding to the one observed close to the interface in the disordered phase. GPA of the layered structure reveals an elongated lattice parameter of 5%–6% compared to LSMO bulk, consistent with the DFT-calculations. However, just at the interface a larger elongation is observed. This ordering of the oxygen vacancies with time is in agreement with the ~0.2 eV energy difference between the ordered and disordered structures found using DFT.

In conclusion, we have studied the strain and electronic structure of a LSMO/STO heterojunction using STEM-HAADF and STEM-EELS. The results reveal a region with an elongated out-of-plane lattice parameter, reduced oxygen content, and lowered manganese oxidation state extending from the interface to about 3 nm into the LSMO film. These properties are attributed to the presence of a brownmillerite phase with disordered oxygen vacancies, in agreement with DFT calculations, not previously reported in as-grown LSMO/STO thin films. After approximately 1.5 years, the same TEM lamella show a brownmillerite phase with ordered oxygen vacancies. These finding shed light on the effect of oxygen vacancies on the structure of complex perovskite oxide interfaces, and reveal that they can order over time possibly affecting functional properties.

This project was supported by the Norwegian Research Council under Project No. 10239707 and The Norwegian PhD Network on Nanotechnology for Microsystems. Takeshi Kasama at Center for Electron Nanoscopy at the Technical University of Denmark (CEN-DTU) was thankfully acknowledged for support with the STEM-EELS investigations. The Norwegian Metacenter for Computational Science (Notur) was acknowledged for providing computational resources for DFT-calculations through the project NN9301K.

[1]Y. Tokura, Rep. Prog. Phys. **69**, 797 (2006).
[2]J. D. Ferguson, Y. Kim, L. F. Kourkoutis, A. Vodnick, A. R. Woll, D. A. Muller, and J. D. Brock, Adv. Mater. **23**, 1226 (2011).
[3]J. Gazquez, S. Bose, M. Sharma, M. A. Torija, S. J. Pennycook, C. Leighton, and M. Varela, APL Mater. **1**, 012105 (2013).
[4]S. V. Kalinin and N. A. Spaldin, Science **341**, 858 (2013).
[5]U. Aschauer, R. Pfenninger, S. M. Selbach, T. Grande, and N. A. Spaldin, Phys. Rev. B **88**, 054111 (2013).
[6]A. Kobrinskii, A. Goldman, M. Varela, and S. Pennycook, Phys. Rev. B **79**, 094405 (2009).
[7]S. Venkatesan, M. Döblinger, C. Daumont, B. Kooi, B. Noheda, J. T. M. De Hosson, and C. Scheu, Appl. Phys. Lett. **99**, 222902 (2011).
[8]L. Samet, D. Imhoff, J.-L. Maurice, J.-P. Contour, A. Gloter, T. Manoubi, A. Fert, and C. Colliex, Eur. Phys. J. B: Condens. Matter **34**, 179 (2003), available at http://link.springer.com/article/10.1140%2Fepjb%2Fe2003-00210-8.
[9]A. Y. Borisevich, H. J. Chang, M. Huijben, M. P. Oxley, S. Okamoto, M. K. Niranjan, J. D. Burton, E. Y. Tsymbal, Y. H. Chu, P. Yu *et al.*, Phys. Rev. Lett. **105**, 087204 (2010).
[10]J. E. Boschker, E. Folven, Å. F. Monsen, E. Wahlström, J. K. Grepstad, and T. Tybell, Cryst. Growth Des. **12**, 562 (2012).
[11]M. Varela, M. Oxley, W. Luo, J. Tao, M. Watanabe, A. Lupini, S. Pantelides, and S. Pennycook, Phys. Rev. B **79**, 085117 (2009).
[12]See http://hyperspy.org/ for HyperSpy: Hyperspectral data analysis toolbox.
[13]P. E. Blochl, Phys. Rev. B **50**, 17953 (1994).
[14]G. Kresse and D. Joubert, Phys. Rev. B **59**, 1758 (1999).
[15]G. Kresse and J. Furthmuller, Phys. Rev. B **54**, 11169 (1996).
[16]J. P. Perdew, A. Ruzsinszky, G. I. Csonka, O. A. Vydrov, G. E. Scuseria, L. A. Constantin, X. Zhou, and K. Burke, Phys. Rev. Lett. **100**, 136406 (2008).
[17]V. I. Anisimov, J. Zaanen, and O. K. Andersen, Phys. Rev. B **44**, 943 (1991).
[18]R. L. Johnson-Wilke, D. Marincel, S. Zhu, M. P. Warusawithana, A. Hatt, J. Sayre, K. T. Delaney, R. Engel-Herbert, C. M. Schlepütz, J.-W. Kim *et al.*, Phys. Rev. B **88**, 174101 (2013).
[19]M. J. Hÿtch, E. Snoeck, and R. Kilaas, Ultramicroscopy **74**, 131 (1998).
[20]T. Riedl, T. Gemming, and K. Wetzig, Ultramicroscopy **106**, 284 (2006).
[21]R. P. Borges, W. Guichard, J. G. Lunney, J. M. D. Coey, and F. Ott, J. Appl. Phys. **89**, 3868 (2001).
[22]D. A. Muller, N. Nakagawa, A. Ohtomo, J. L. Grazul, and H. Y. Hwang, Nature **430**, 657 (2004).
[23]L. Yao, S. Majumdar, L. Äkäslompolo, S. Inkinen, Q. H. Qin, and S. V. Dijken, Adv. Mater. **26**, 2789 (2014).
[24]S. Stølen, E. Bakken, and C. E. Mohn, Phys. Chem. Chem. Phys. **8**, 429 (2006).
[25]R. G. Palgrave, P. Borisov, M. S. Dyer, S. R. C. McMitchell, G. R. Darling, J. B. Claridge, M. Batuk, H. Tan, J. Verbeeck, J. Hadermann *et al.*, J. Am. Chem. Soc. **134**, 7700 (2012).
[26]A. B. Shah, Q. M. Ramasse, S. J. May, J. Kavich, J. G. Wen, X. Zhai, J. N. Eckstein, J. Freeland, A. Bhattacharya, and J. M. Zuo, Phys. Rev. B **82**, 115112 (2010).
[27]K. Matsumoto, M. Haruta, M. Kawai, A. Sakaiguchi, N. Ichikawa, H. Kurata, and Y. Shimakawa, Sci. Rep. **1**, 27 (2011).
[28]Y. M. Kim, J. He, M. D. Biegalski, H. Ambaye, V. Lauter, H. M. Christen, S. T. Pantelides, S. J. Pennycook, S. V. Kalinin, and A. Y. Borisevich, Nat. Mater. **11**, 888 (2012).
[29]H. Jeen, W. S. Choi, J. W. Freeland, H. Ohta, C. U. Jung, and H. N. Lee, Adv. Mater. **25**, 3651 (2013).
[30]See supplementary material at http://dx.doi.org/10.1063/1.4906920 for details on the different positioning of the oxygen vacancies in the simulated structures.

Paper II

Assessing electron beam sensitivity for $SrTiO_3$ and $La_{0.7}Sr_{0.3}MnO_3$ using electron energy loss spectroscopy

Magnus Nord, Per Erik Vullum, Ingrid Hallsteinsen, Thomas Tybell, and Randi Holmestad

Ultramicroscopy, 169, 98–106 (2016)

Ultramicroscopy 169 (2016) 98–106

Contents lists available at ScienceDirect

Ultramicroscopy

journal homepage: www.elsevier.com/locate/ultramic

Assessing electron beam sensitivity for $SrTiO_3$ and $La_{0.7}Sr_{0.3}MnO_3$ using electron energy loss spectroscopy

Magnus Nord [a,*], Per Erik Vullum [a,c], Ingrid Hallsteinsen [b], Thomas Tybell [b], Randi Holmestad [a]

[a] Department of Physics, NTNU, Trondheim, Norway
[b] Department of Electronics and Telecommunications, NTNU, Trondheim, Norway
[c] Materials and Chemistry, SINTEF, Trondheim, Norway

ARTICLE INFO

Article history:
Received 19 January 2016
Received in revised form
23 June 2016
Accepted 3 July 2016
Available online 5 July 2016

Keywords:
Electron energy loss spectroscopy
Perovskite oxide
Quantification
STEM
Beam damage
Model based approach

ABSTRACT

Thresholds for beam damage have been assessed for $La_{0.7}Sr_{0.3}MnO_3$ and $SrTiO_3$ as a function of electron probe current and exposure time at 80 and 200 kV acceleration voltage. The materials were exposed to an intense electron probe by aberration corrected scanning transmission electron microscopy (STEM) with simultaneous acquisition of electron energy loss spectroscopy (EELS) data. Electron beam damage was identified by changes of the core loss fine structure after quantification by a refined and improved model based approach. At 200 kV acceleration voltage, damage in $SrTiO_3$ was identified by changes both in the EEL fine structure and by contrast changes in the STEM images. However, the changes in the STEM image contrast as introduced by minor damage can be difficult to detect under several common experimental conditions. No damage was observed in $SrTiO_3$ at 80 kV acceleration voltage, independent of probe current and exposure time. In $La_{0.7}Sr_{0.3}MnO_3$, beam damage was observed at both 80 and 200 kV acceleration voltages. This damage was observed by large changes in the EEL fine structure, but not by any detectable changes in the STEM images. The typical method to validate if damage has been introduced during acquisitions is to compare STEM images prior to and after spectroscopy. Quantifications in this work show that this method possibly can result in misinterpretation of beam damage as changes of material properties.

1. Introduction

Perovskite oxide materials have received a great deal of interest due to their magnetic and electronic properties [1,2]. In bulk form they exhibit a wide range of functional properties, such as ferroelectricity [3], ferromagnetism [4], dielectric properties, and colossal magnetoresistance [4]. These range of properties are enabled by strong structure–function coupling, where small variations in structural parameters can result in large changes in functional response. In recent years there has been a resurgence of interest in these materials due to advances in thin film synthesis methods such as molecular beam epitaxy and pulsed laser deposition (PLD), where epitaxial growth can be controlled down to single monolayers [3]. By epitaxial growth and correct substrate use it is possible to control the structure, opening for new avenues for fine tuning functional properties.

One such control parameter is chemical substitution of the A- or B-cations. For example, by replacing La with Sr in $La_{1-x}Sr_xMnO_3$ the magnetic response can be tuned, and at $x \approx 0.3$ maximum in colossal magnetoresistance is observed [5]. Strain engineering is another control parameter, by changing the in-plane lattice constant of the substrate the thin film's in-plane lattice spacings can be locked to the substrate's. This clamping can modify the crystal structure of the film, for example through biaxial strain and suppression of oxygen octahedral rotations [6,7]. Oxygen vacancies constitute an important control parameter. It has been reported that by growing oxygen deficient $La_{0.5}Sr_{0.5}CoO_{3-\delta}$ on substrates with different lattice parameters, the oxygen vacancies can order in specific crystal directions [8]. Oxygen vacancies can also affect the conductivity of a material, for example turning the insulating $SrTiO_3$ into a conductor through charge transfer from the vacancy to the titanium atom [9]. In $La_{0.7}Sr_{0.3}MnO_3$, the presence of oxygen vacancies can lead to breakdown of the ferromagnetic order by suppressing the double-exchange mechanism [10]. Lastly, crystal orientation of the substrate adds another control parameter. As materials often are anisotropic, growing films in different crystal orientations is paramount. The most studied substrate orientation has been the (100) orientation, however recently (111) oriented

* Corresponding author. Present address: SUPA, School of Physics and Astronomy, University of Glasgow, Glasgow G12 8QQ, United Kingdom.
E-mail address: magnunor@gmail.com (M. Nord).

http://dx.doi.org/10.1016/j.ultramic.2016.07.004
0304-3991/

thin film systems have been realized [11,12]. By relying on the discussed control parameters, it should be possible to fine tune functional properties and to tailor-make devices. However, the complex interplay between the different parameters makes it challenging to understand and characterize the relationship between structure and properties, generating a demand for high resolution spatial techniques.

Transmission electron microscopy (TEM) is one of the most used tools to study perovskite oxides [7,12–17], and in particular embedded parts of the materials. In the latter years, the development of sub-Å resolution scanning TEM [18,19] (STEM) combined with high energy resolution electron energy loss spectroscopy (EELS) has turned the combination of STEM and EELS into one of the most powerful tools to characterize the structure and electronic properties of perovskite oxides with atomic resolution [13,14]. EEL spectra are now used to collect information about chemical composition including cation diffusion [20], cation oxidation state [21,22], crystal structure modifications [23], and vacancies [15,16]. These are all parameters that the functional properties are extremely sensitive to. However, a correct interpretation of structure–property relations relies on several sensitive steps in the characterization scheme: (a) the high energy and flux of the electron beam used in modern TEMs can possibly modify the materials due to beam damage [17,24–27], (b) the interpretation of the fine structure information of the EEL core loss spectra rely on a correct handling of the plasmon background and modelling of the various features in the spectra, and (c) the TEM sample preparation can possibly alter the inherent structure and properties of the materials.

In the present paper we have used STEM–EELS to systematically study an epitaxial heterostructure with two of the most studied perovskite oxides: $La_{0.7}Sr_{0.3}MnO_3$ (henceforth LSMO) grown on $SrTiO_3$ (STO) along the [111] direction. A refined and improved model based approach for processing of EELS spectra in order to correctly interpret the fine structure of the core loss is presented. From this we have established thresholds for beam current and exposure times, beyond which beam damage is introduced. One very important observation is that for LSMO the onset of beam damage, both as a function of beam current and exposure time, sets in before any damage can be seen directly in the STEM image. For STO, changes in the STEM image occur simultaneously with the onset of beam damage as deduced from EELS, however some of these subtle changes can be missed under common experimental conditions.

2. Materials and method

2.1. Experiment

The beam exposure experiments were performed on LSMO/STO:Nb-(111) and LSMO/$LaFeO_3$ (LFO)/STO-(111) samples grown by PLD [11]. Cross section TEM lamellas were prepared by focused ion beam (FIB), on a FEI Helios Nanolab DualBeam FIB, using standard lift-out technique. Prior to starting the FIB preparation, a 10 nm Pt/Pd layer was sputter coated on top of the wafer. In the FIB an additional 80 nm Pt protection layer was deposited by electron beam assisted deposition, before adding a 3 μm carbon protection layer by ion beam assisted deposition. The coarse ion beam thinning was done at 30 kV. Final thinning was performed with 5 and 2 kV ion beam acceleration voltages. After FIB preparation, the TEM samples were milled for 20 s on each side with Ar-ions at 100 eV using a Gatan PIPS II. The TEM experiments were done on a double-corrected Jeol ARM200CF equipped with a Gatan Quantum ER, using an energy dispersion of 0.25 eV/channel and a collection semi-angle of 66 mrad. Low and core loss EEL spectra were acquired quasi-simultaneously using the DualEELS functionality on the Gatan Quantum. All STEM-high angle annular dark field (HAADF) data were acquired with inner and outer collection angles of 118–471 mrad. A HAADF-STEM overview of the LSMO/STO sample is shown in Fig. 1.

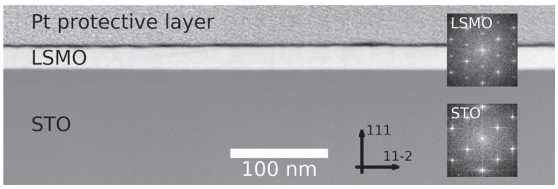

Fig. 1. HAADF STEM overview of the LSMO film, STO substrate and the FIB deposited Pt protection layer. Insets show FFTs from HRTEM images acquired on the same sample.

The beam exposure experiments were performed by acquiring a STEM-HAADF image of the area, then positioning the STEM probe inside this area while simultaneously acquiring an EEL spectrum every 0.1 s. The probe remained at this position for up to 3.3 min. After the exposure experiment was finished, another STEM-HAADF image was acquired for comparison and to estimate the sample drift. The sample drift was estimated by using some landmark features in the field of view, for example an inhomogeneity in the Pt-protective layer for the experiments done on the LSMO film. For the STO substrate, which has no inherent identifiable features, a marker was created by leaving the electron probe for a sufficient time to change the HAADF intensity, like in Fig. 3. This procedure was repeated for different acceleration voltages, spot sizes and condenser apertures on both the LSMO film, and the STO substrate. The properties of the different probes are shown in Table 1. For the LSMO film, all the exposure experiments were done in the middle of the cross section film: about 10 nm from the interface. The STO substrate exposures were performed about 100 nm away from the interface. The TEM foil thickness in the analyzed regions was approximately 0.5λ (λ = inelastic mean free path) at 200 kV, and 0.6λ at 80 kV.

2.2. EELS modelling

To extract physical relevant parameters from the EELS fine structure data, the model based approach was utilized [28] using the open source software HyperSpy [29]. This approach works by fitting several components to an experimental spectrum, and the sum of these components is the model. These components are distributions or functions such as Gaussians or Hartree–Slater core loss ionization edges [30]. For modelling the titanium-$L_{2,3}$ core loss edge (transitions between $2p^{1/2}$ and $2p^{3/2}$ to 3d), four Gaussians were used (one for each peak), and two Hartree–Slater edges

Table 1
Properties for electron beams used in the exposure experiments. Probe currents were measured using the Gatan Quantum ER.

Acceleration voltage (kV)	Probe	Aperture (μm)	Current (pA)	Size (Å)	Convergence semi-angle (mrad)
200	3C	50	646	1.2	34.2
200	3C	30	223	1.1	20.4
200	5C	50	177	0.9	34.2
200	5C	30	63	0.9	20.4
80	3C	50	631	2.2	34.2
80	3C	30	215	1.9	20.4
80	5C	50	167	1.6	34.2
80	5C	30	58	1.4	20.4

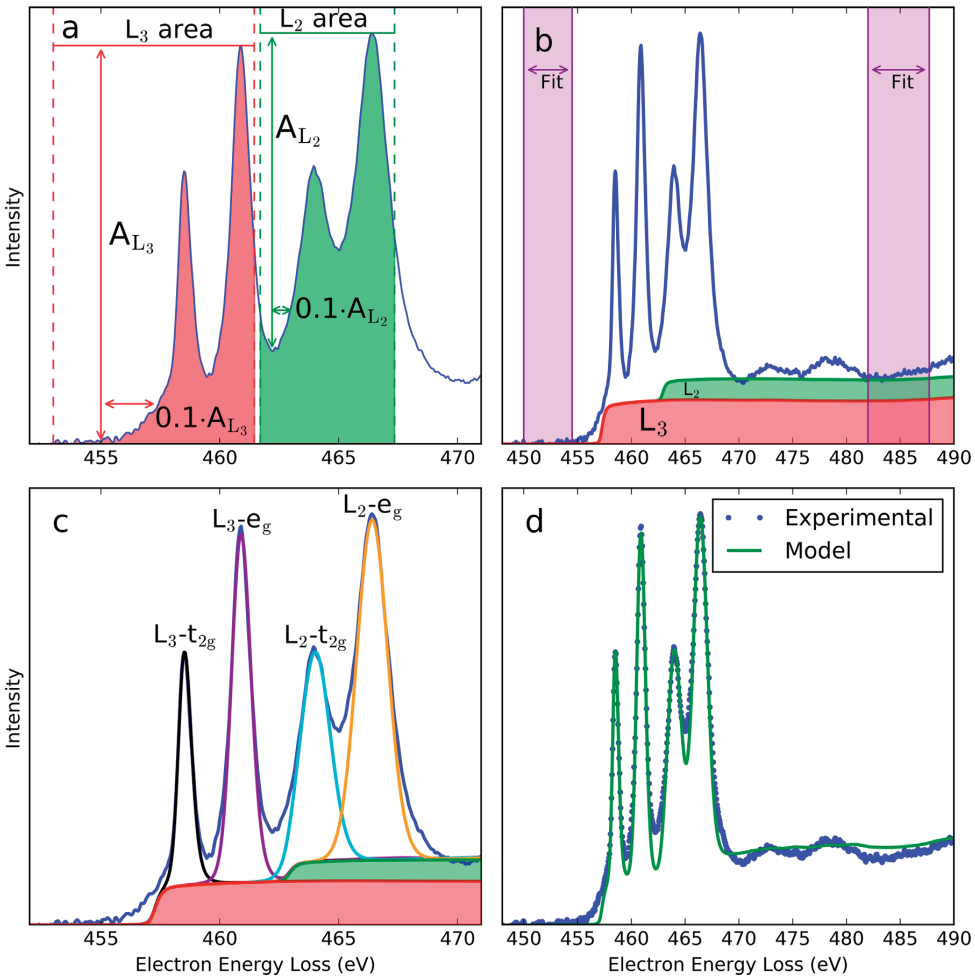

Fig. 2. Modelling of $SrTiO_3$ Ti-$L_{2,3}$ white lines. (a) Showing how the onset of the Ti-L_3 and L_2 Hartree–Slater core loss edges are calculated. The minimum and maximum intensities are found in the red (L_3) area, which gives the amplitude A_{L_3}. This amplitude times 0.1 gives the onset intensity, which is used to find the L_3 onset energy. The L_2 onset is found in the same way, using the green area. (b) Purple areas show the pre- and post-edge fitting areas for the intensity of the Hartree–Slater core loss edges. The L_2 Hartree–Slater edge intensity is locked to half the L_3 Hartree–Slater edge intensity. The resulting core loss edges are shown with the green and red areas. (c) The Ti-$L_{2,3}$ white lines fitted using four Gaussian distributions. (d) The full fitted model, which is a sum of all the components shown in (c). (For interpretation of the references to color in this figure caption, the reader is referred to the web version of this paper.)

which model the L_2 and L_3 ionization edges (Fig. 2b). The manganese $L_{2,3}$ peaks were modelled in the same fashion, but only by using two Gaussians and two Hartree–Slater edges. The oxygen-K edge was modelled using three Gaussians. The core loss ionization edge of the O-K edge was not modelled directly using its own component, due to the difficulty of setting a robust edge onset energy. However the changes in the fine structure were still picked up in a robust fashion using the Gaussians. For all core loss edges, one could use different components (such as Voigt functions) or add more Gaussians to potentially get better models. However, this would increase the amount of free variables, causing less robust fitting, which again could lead to misinterpretation of data. Thus the amount of components for each core loss edge was chosen so that, (a) they would accurately model the changes of the EELS fine structure and (b) they would fit the data robustly.

One advantage of the model based approach is that the low loss plasmon signal is convolved with the core loss signal to account for multiple scattering. Hence, possible artifacts introduced by more common deconvolution techniques are avoided. In addition, this will result in better fits, given that a suitable model of the core loss edges can be constructed. The steps for fitting the titanium-$L_{2,3}$ EELS fine structure are outlined below, similar to the process used by Tan et al. [31] to calculate the edge onset energy:

1. Calibrate the energy offset by using the zero loss peak (ZLP), which is acquired quasi-simultaneously.
2. Do principal component analysis (PCA) for increasing the signal-to-noise ratio [21].
3. Fit the power law background and freeze it.
4. Determine the Ti-L_3 ionization edge onset energy (Fig. 2a).
   (a) The edge onset energy is set to a percentage of the net height of the L_3 peak.
   (b) If this percentage value is set too low, the edge onset energy can be influenced by pre-edge noise. But if it is too high, the

edge onset energy can be affected by the shape of the fine structure. For the present datasets, 10% of the net height of the peak was chosen, in-line with Tan et al. [31].

5. The Ti-L_2 edge onset energy is set the same way as Ti-L_3, where the net height of the L_2 peak is calculated by using the lowest point between the $L_{2,3}$ peaks, and the highest point in the L_2 peaks (Fig. 2a).
6. Lock the edge onset energy for both Ti-L_2 and L_3.
7. Fit ionization edges to pre- and post-edge areas (Fig. 2b, purple regions). The L_2 ionization edge (green region) intensity is set to half the intensity of the L_3 [30] ionization edge (red region), due to that the $2p^{3/2}$ and $2p^{1/2}$ electron orbitals have four and two electrons, respectively.
8. Use four Gaussians to fit the white lines: firstly fitting each Gaussian in a narrow region around each peak, starting with the most intense (e_g), then fitting all the Gaussians simultaneously without any constraints.

An important consideration is the effect of mixed oxidation states on this method. For example, the Mn-$L_{2,3}$ EELS fine structure for a mix of 50% Mn^{+2} and 50% Mn^{+4} would be different compared to 100% Mn^{+3}. The former gives a signal that is a superposition of the spectra from Mn^{+2} and Mn^{+4}. This mixed Mn^{+2} and Mn^{+4} spectrum (with an average oxidation state of $+3$) is significantly different from the Mn^{+3} spectrum. Due to chemical shift the Mn^{+2} spectrum would be at lower energy loss compared to the Mn^{+4}, while the Mn^{+3} would be somewhere in the middle. Thus, the mixed oxidation state spectrum peak width would be larger than the single oxidation state spectrum, which would be detectable through the sigma value of the L_3 and L_2 Gaussians [32]. In co-junction with the Mn-L_3 core loss ionization edge onset [31], this could be a robust way of detecting mixed oxidation state systems. For the Mn-$L_{2,3}$ datasets analyzed in this work there was the opposite effect, a narrowing of the EELS fine structure.

2.3. Assessing beam damage

Using the parameters from the Gaussians discussed above, one can calculate attributes. These attributes are values like the Ti-$L_{2,3}$ e_g/t_{2g} ratio and Mn-$L_{2,3}$ energy separation, which can be used to calculate physical properties like oxidation states. To find when beam damage occurs in the material, one can find the point where the change in an attribute is significant, i.e. exceeds random variations. The beginning of the beam exposure is used as reference to set an initial value for the attribute for an undamaged region. For example between 0 and 10 nC/nm^2 in Fig. 5c. For the datasets analyzed in this work, the random noise in the attributes was relatively high (see Fig. 5c, blue transparent line) so the datasets were smoothed using a Gaussian blur (see Fig. 5c, orange line). Next, a calibration dataset with very low electron beam current pr. area was used to calculate the uncertainty for each of the attributes, these values are shown in Table 1 in the supporting information.

To know if the change of an attribute translates into a significant physical change is important. However, it is outside the scope of this work to find the oxidation states of Mn and Ti as a function of beam exposure. In addition, having a grasp on the uncertainty is important for knowing how sensitive the method is in detecting changes in the material. The sensitivity ranged from about 0.05 to 0.18 oxidation state, which makes it possible to detect physically relevant changes. The details of this are described in the supporting information.

Converting the attributes to physical properties can be done using literature values of materials with known oxidation states. For titanium, the oxidation state is determined by comparing the Ti-$L_{2,3}$ t_{2g}/e_g intensity ratio or the average center position of the four Ti-$L_{2,3}$ peaks with materials where the Ti-oxidation state is known. Here, spectra from $BaTi_{1-x}Nb_xO_3$ by Shao et al. [33] were used to get ballpark estimates of the relation between the t_{2g}/e_g intensity ratio and the oxidation state. The intensity ratio and the center difference between the O-K prepeak and peak B were also analyzed. The O peaks were less sensitive than the Ti-$L_{2,3}$ peaks to beam damage, and they did not show any significant changes as a function of changing Ti oxidation state. Similar values calculated for manganese is shown in the supporting information.

3. Results and discussion

To assess the sensitivity of STO to electron beam exposure, several locations in vicinity to each other were exposed to different electron doses. An EELS line scan was acquired across these exposed locations to systematically quantify the EEL spectra. The result of such an experiment at 200 kV is seen in Fig. 3. The HAADF STEM image has five exposed locations with increasing dose going from the left to the right. Dashed green lines are the signal from the exposed regions, and the solid blue line is the reference from a location that was not exposed prior to the line scan. For the two

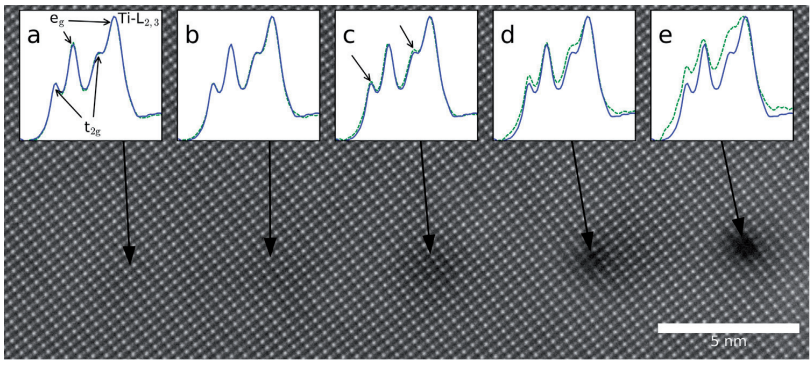

Fig. 3. STEM-HAADF image of STO after beam exposure at 200 kV in the points highlighted by the arrows. The leftmost area (a) having received the least amount of electron dose, and the rightmost (e) the most. After the beam exposures, a line scan was done across all the exposed points. Insets show the Ti-$L_{2,3}$ edge from an unexposed area (solid blue) and the exposed points (dashed green). The insets show an increasing amount of sample damage with increasing electron dose, as expected. No changes in HAADF intensity and the Ti-$L_{2,3}$ edge are observed in (a) and (b). In (c) there are some subtle changes, indicated by the arrows, in the form of increasing intensity in the t_{2g} peaks, and a small change in the HAADF intensity. (d) and (e) show larger changes in both the Ti-$L_{2,3}$ and the HAADF intensity. (For interpretation of the references to color in this figure caption, the reader is referred to the web version of this paper.)

least exposed locations, (a) and (b), there are no detectable changes in the EELS fine structure of Ti-$L_{2,3}$. For (c) there are some subtle changes highlighted with the arrows: the e_g-peaks increase slightly compared to the t_{2g}-peaks. In (d) and (e) there are significant changes in the EELS fine structure. These changes match well with the corresponding changes in the HAADF signal intensity. This is consistent with a removal of atoms through electron-beam sputtering [24], which leads to a thinner TEM foil. Electron beam sputtering is further confirmed by a strong decrease of the plasmon peak signal, seen in Fig. 2 in the supporting information. Even for (c), with subtle EELS fine structure changes, there is a slight decrease in the HAADF intensity. Hence, for STO a change in the HAADF intensity can be used to indicate beam damage. In Fig. 3 the entire dynamic range of the STEM-detector is used to visualize the contrast of STO. If other phases than STO are present in the STEM image (for instance vacuum or Pt), only a limited part of the detector's dynamic range will be used to display the contrast variations in STO, which can possibly wipe out contrast changes due to beam damage.

Beam damage was further studied as a function of acceleration voltage, and by also including the LSMO thin film. A combination of HAADF STEM-images and EEL spectra at both 80 and 200 kV for STO and LSMO is shown in Fig. 4. The exposed areas are highlighted with arrows. The insets show the EELS fine structure before (solid blue) and after (dashed green) the beam exposure experiment, for the B-cation (Ti-$L_{2,3}$ or Mn-$L_{2,3}$) and the O-K. As expected from Fig. 3, for the STO at 200 kV there is a clear reduction of HAADF intensity in co-junction with changes in the EELS fine structure. At 80 kV no changes were observed in either the HAADF intensity nor the EELS fine structure for STO, independent of probe intensities and exposure time. Electron beam induced damage in LSMO behaves very differently from beam damage in STO. This is demonstrated at 200 kV in Fig. 4c, where large changes in the Mn-$L_{2,3}$ and O-K edges were observed despite that no changes could be seen in the corresponding HAADF-images. The changes in the Mn-$L_{2,3}$, signified with an increase of the

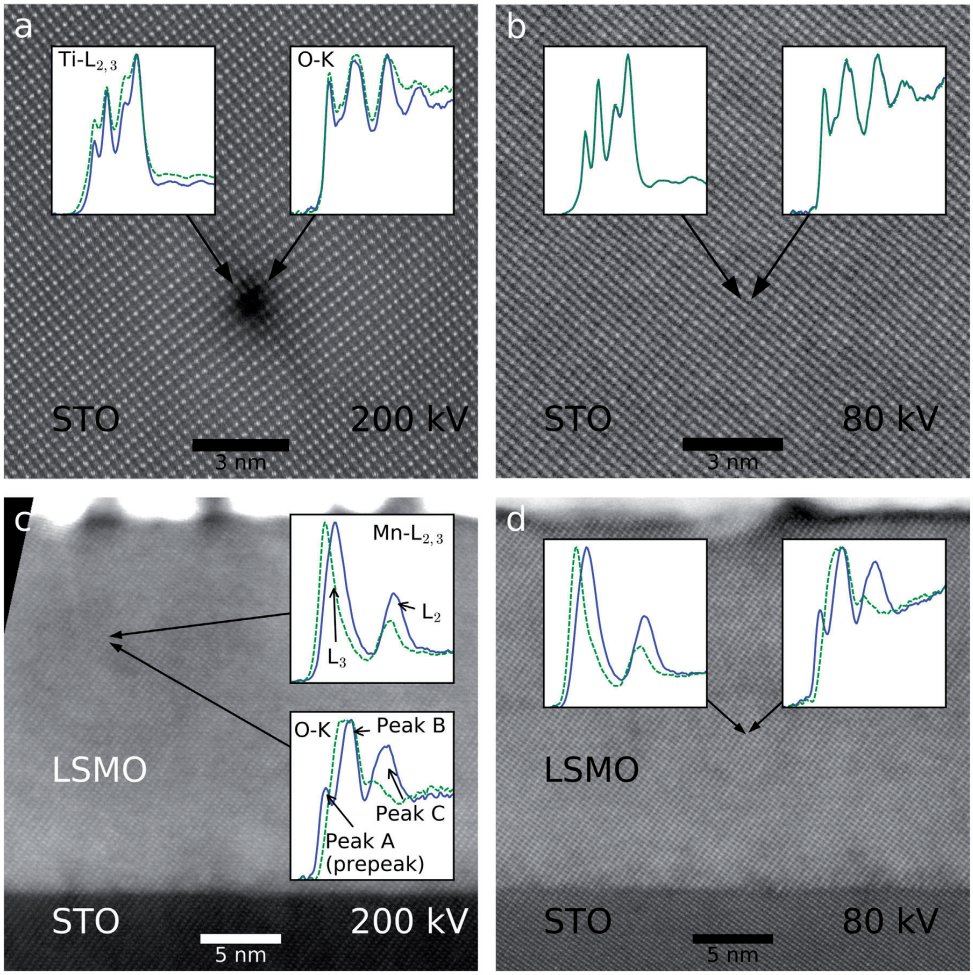

Fig. 4. STEM-HAADF images acquired after a long beam exposure, arrows highlighting the exposed points. Insets showing the B-cation $L_{2,3}$ and oxygen-K core loss EELS, before (solid blue) and after (dashed green) the beam exposure. (a) STO after exposure to a 200 kV electron beam, shows changes in the HAADF intensity and EELS fine structure. (b) STO after exposure to a 80 kV electron beam, showing no changes in HAADF and EELS. (c) and (d) LSMO after exposure to 200 and 80 kV electron beam, respectively, show no changes in HAADF intensity, but large changes in both EELS fine structures. Arrows in the insets in (c) highlight features in the EELS fine structure. (For interpretation of the references to color in this figure caption, the reader is referred to the web version of this paper.)

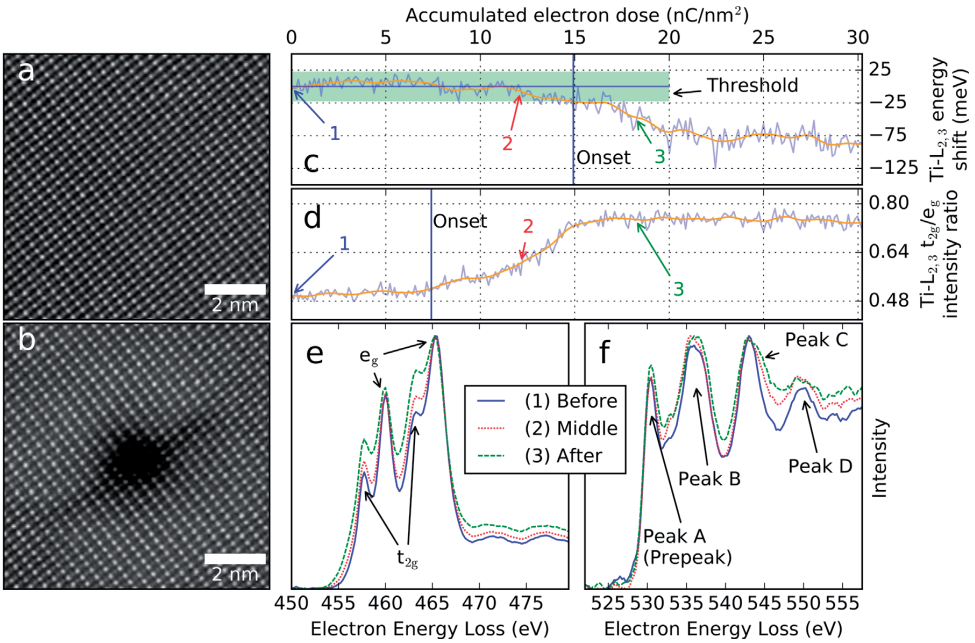

Fig. 5. Beam exposure experiment on $SrTiO_3$ at 200 kV acceleration voltage. (a) STEM-HAADF image of $SrTiO_3$, before the experiment. (b) Same as (a), but after the experiment. (c) Total energy shift of the Ti-$L_{2,3}$ white lines as a function of accumulated electron dose. The mean initial value is shown with the horizontal blue line, and the threshold is marked with the green transparent box. The onset is set where the smoothed attribute (orange line) goes outside the threshold. (d) Ratio of the Ti-$L_{2,3}$ e_g and t_{2g}, as a function of accumulated electron dose. (e) EEL spectra from the titanium-$L_{2,3}$ core loss edge, showing the changes in the EELS fine structure before, during and after the beam exposure marked with the arrows in (c) and (d). (f) Same as (e), but for the O-K core loss edge. For this specific probe current, none of the measured attributes in the O-K edge was significant. However, there are clear changes in the EELS fine structure signified by a reduction of peak D. (For interpretation of the references to color in this figure caption, the reader is referred to the web version of this paper.)

$L_{2,3}$-ratio, are consistent with a reduction of the Mn oxidation state [21,31]. For the O-K edge, a decrease of both the prepeak and peak C and an increase of peak B indicate that oxygen vacancies are created [17]. All these changes are consistent with oxygen being removed from the material: oxygen vacancies lead to less charge transfer from manganese, giving a lower Mn oxidation state. However, the low atomic number of oxygen compared to the cations makes the significant beam damage demonstrated in LSMO practically impossible to detect directly in the HAADF STEM images.

Continuous acquisition of core loss EEL spectra during accumulated beam exposure was used to determine beam damage as a function of electron dose. Such an experiment on STO at 200 kV is shown in Fig. 5, where the beam has exposed the same point for 3.3 min (a total of 30 nC/nm^2). Figs. 5a and b show HAADF STEM images before and after the beam exposure experiment. The EELS data processing method as explained in Section 2.2 was used to quantify the features in Ti-$L_{2,3}$ and O-K core loss edges. The results are shown in Figs. 5c and d. The chemical shift of the Ti-$L_{2,3}$ peak as a function of the accumulated electron dose is shown in Fig. 5c. No chemical shift is observed until about 14 nC/nm^2, and at higher dose there is a shift towards lower energy. This chemical shift is consistent with a change from Ti^{+4} towards Ti^{+3} [16]. In Fig. 5d the intensity ratio between the Ti-$L_{2,3}$ e_g and t_{2g} peaks (highlighted in Fig. 5e) is plotted. From about 7 nC/nm^2 electron dose there is a clear increase in the t_{2g}/e_g ratio, consistent with a decrease in the Ti oxidation state [16]. This behavior is observed in all beam exposure experiments of STO at 200 kV: the t_{2g}/e_g intensity ratio is the first detectable change in the fine structure, approximately at half of the electron dose compared to where changes are observed in the energy shift. Looking at the actual Ti-$L_{2,3}$ (Fig. 5e) fine

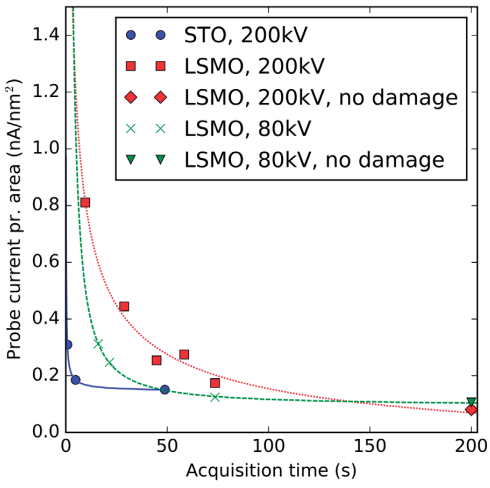

Fig. 6. Results from several beam exposure experiments, showing the onset of damage on the material as a function of probe current per area and exposure time. Green 'x' and red squares show the onset of damage on LSMO at 80 and 200 kV acceleration voltages, respectively. Blue circles show the same for STO at 200 kV, no beam damage was observed for STO at 80 kV. For sufficiently low probe current no damage was observed, even if the total electron dose was higher than the dose needed to get damage at higher probe currents. Some of these points are shown with the red diamond (LSMO 200 kV) and green triangle (LSMO 80 kV). The lines are power law fits as a guide to the eye, for showing the probe currents/acquisition times below the threshold beam damage. (For interpretation of the references to color in this figure caption, the reader is referred to the web version of this paper.)

structure at certain points in time in the exposure experiment (noted by arrows in (c) and (d)), there is a clear change consistent with the quantified values in Fig. 5c and d. All these changes are consistent with a shift from Ti^{4+} to Ti^{3+} [16]. The features quantified in the O-K core loss edge did not show any significant changes, so they are not presented here. However, as seen in Fig. 5f there are some subtle changes as a function of electron dose, mostly in peak D.

The same experiment was repeated for several probe currents, which were varied by changing the condenser apertures or spot sizes. The onset of beam damage for the different probe currents in STO and LSMO, for both 80 and 200 kV acceleration voltages, are presented in Fig. 6. No beam damage was observed for STO at 80 kV, so this is not included. Fig. 6 shows how long one can expose the sample with a specific current before beam damage is observed. To avoid beam damage, the combination of probe

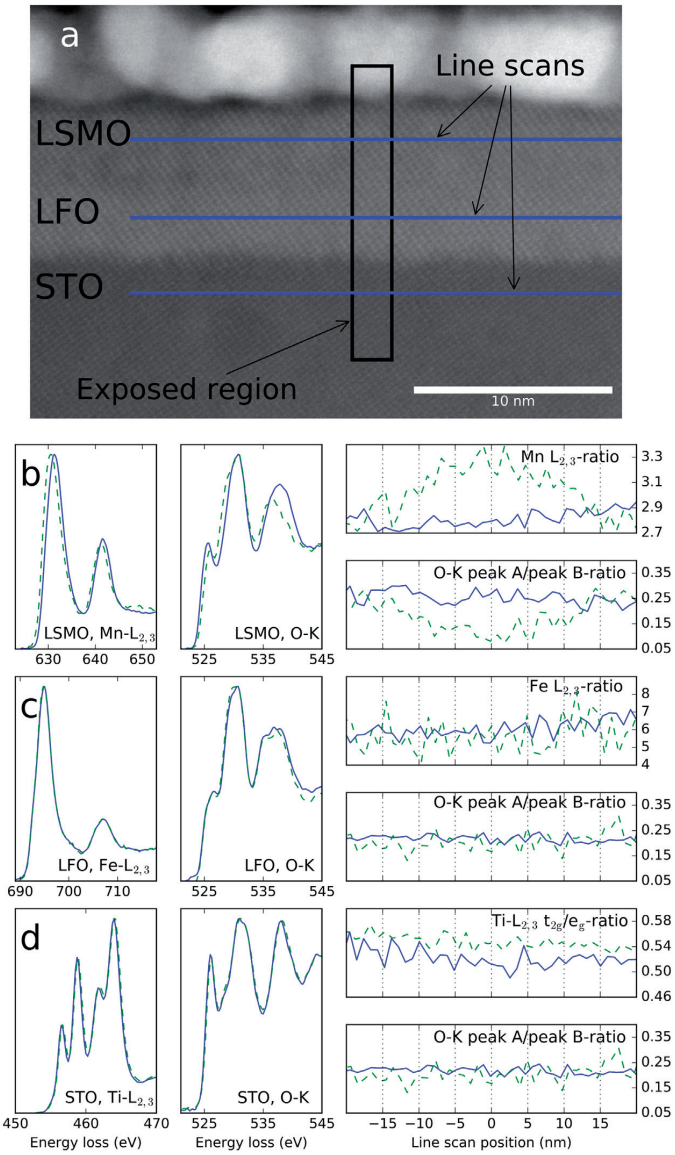

Fig. 7. Results of an electron beam exposure experiment at 80 kV on a LSMO(4 nm)/LFO(4 nm)/STO-(111) heterostructure. (a) STEM-HAADF image of the region. Three short exposure EELS line scans were acquired parallel to the films (blue lines) before and after exposing a 2 nm wide region across the substrate and films in the form of an EELS map (black rectangle). Comparisons of the line scans, before and after the exposure, are shown in (b), (c) and (d) for LSMO, LFO and STO, respectively. The leftmost figures show the B-cation $L_{2,3}$-edges, the middle figures the oxygen K-edge, and the rightmost figures the quantified data using EELS data processing method as explained in Section 2.2. For the LSMO shown in the (b) figures, there are changes in both the Mn-$L_{2,3}$ and O-K fine structure, consistent with the electron beam damage seen in Fig. 4. The changes in the EELS fine structure are about 20 nm wide, which is much wider than the exposed region. The LFO and STO in (c) and (d) do not show any significant changes. (For interpretation of the references to color in this figure caption, the reader is referred to the web version of this paper.)

current and acquisition time must be kept below the indicated lines. For sufficiently low probe currents no changes in the material were observed, so the data points at acquisition time = 200 s represents these. The power law fits in Fig. 6 are guidelines to the eye.

For all the beam exposure experiments on STO at 200 kV, the first observable changes were in the Ti-$L_{2,3}$ t_{2g}/e_g ratio. These changes were followed by a chemical shift of the Ti-$L_{2,3}$ peaks, and finally by a change of energy difference between the O-K prepeak and peak B. However, for the lowest probe currents (as seen in Fig. 5), the latter changes would not become visible until much later, or not at all within the exposure time. Therefore, the best way to check for beam damage in STO at 200 kV is to look for changes in the Ti-$L_{2,3}$ t_{2g}/e_g ratio. For the LSMO film, fine structure changes due to beam damage eventually set in at both 80 and 200 kV acceleration voltage. In all the experiments done with LSMO, the energy difference between the O-K prepeak and peak B was the first to show any observable changes. In the high probe current experiments, this was followed shortly by changes in the Mn-$L_{2,3}$ intensity ratio and increasing L_3 and L_2 energy difference. However in the low probe current experiments, no changes were observed in the Mn-$L_{2,3}$ until much later. Thus, the best way to check for beam damage in LSMO, is to monitor for a possible energy shift of the oxygen prepeak. Comparing the various onsets of beam damage, LSMO will be best characterized at 200 kV, while STO should be characterized at 80 kV. As discussed, beam damage in STO and LSMO behaves differently as a function of acceleration voltage. For STO, there is probably a critical voltage somewhere between 80 and 200 kV, beyond which knock-on-damage sets in, since no damage was observed at 80 kV even for very high probe currents. LSMO is more robust to knock-on-damage of the cations, but more sensitive to the introduction of oxygen vacancies [17].

A practical example of the effect of beam damage when doing EELS mapping is shown in Fig. 7. Here, a LSMO(4 nm)/LFO(4 nm)/STO-(111) heterostructure was exposed to a large electron beam dose at 80 kV in the form of an EELS map. Before and after the EELS map, three short exposure EELS line scans were acquired on the LSMO, LFO and STO parallel to the interface, shown in Fig. 7a as blue lines. EELS data from the line scans are shown in Fig. 7b, c and d, for LSMO, LFO and STO, respectively. Comparing the EELS fine structure from prior to and after the map, there are clear changes in the LSMO, but no significant changes in the LFO or STO. The changes in the LSMO EELS fine structure are consistent with the beam damage observed in Fig. 4. The electron beam induced oxygen vacancies in LSMO extend over a region (20 nm wide) that is much larger than the region (2 nm wide) exposed during acquisition of the EELS map. This is most likely caused by oxygen diffusing from the nearby unexposed LSMO regions into the exposed region and driven by the gradient in concentration of oxygen vacancies.

When doing these kinds of long exposure acquisitions, one must first check whether the electron beam damages the material. If damage is observed, one must try to mitigate it somehow. As the example above shows, electron beam damage in STO can be avoided by using 80 kV. However, since this is not a viable option for LSMO the beam dose must be reduced somehow. The easiest way is by simply reducing the dwell time, but this will only work to a certain point due to the signal-to-noise ratio becoming too low. One solution is to increase the spectrometer dispersion, which lead to more electron counts in each detector channel. This gives an increase in signal-to-noise, since the effects of detector shot noise will be reduced. On the downside, this reduces the energy resolution of the EELS data, making it harder to resolve the fine structure. Another solution is to expose a larger area: doing several line scans in different regions, and aligning them in post processing with respect to some feature (for example an interface), and summing them. In the thin film systems presented in this work, this would lead to a large loss of spatial resolution in the in-plane direction, and small loss of spatial resolution in the out-of-plane direction (depending on the alignment procedure). In practice, several of these workarounds should be combined when acquiring datasets from beam sensitive materials.

4. Conclusions

In the present work thresholds for electron beam damage have been determined as a function of acceleration voltage and probe current in $SrTiO_3$ and $La_{0.7}Sr_{0.3}MnO_3$. At 200 kV acceleration voltage, $SrTiO_3$ needs to be handled with great care to avoid beam damage that possibly can lead to misinterpretation of advanced STEM–EELS data. At typical probe currents, used for analytical characterization, changes in both the electron energy loss fine structure and high angle annular dark field contrast are quickly observed. The electron beam sputters the $SrTiO_3$ TEM foil, but also changes the oxidation state of Ti as observed both by a change in the Ti-$L_{2,3}$ ratio and by a chemical shift of the Ti-$L_{2,3}$ peaks. Hence, high electron dose characterization of $SrTiO_3$ should better be done at a low acceleration voltage since no electron beam damage was observed at 80 kV, independent of probe current and accumulated electron dose.

Electron beam damage occurred very differently in $La_{0.7}Sr_{0.3}MnO_3$ compared to in $SrTiO_3$. In $La_{0.7}Sr_{0.3}MnO_3$ the electron beam damage turned the material substoichiometry by creating oxygen vacancies. The loss of oxygen atoms significantly changed the oxidation state of Mn, which potentially can lead to wrong interpretations of electronic, magnetic and structural properties. These electron beam induced modifications of the material were observed by significant changes in the fine structure of both the O-K and the Mn-$L_{2,3}$ peaks, but not by any observable changes in any HAADF STEM images. Furthermore and unlike $SrTiO_3$, beam damage in $La_{0.7}Sr_{0.3}MnO_3$ occurred very similarly both at 80 and 200 kV.

Acknowledgment

The Research Council of Norway (RCN) is acknowledged for the support to the Norwegian Micro- and Nano-Fabrication Facility, NorFab (197413/V30). Partial funding for this work was obtained from the Norwegian PhD Network on Nanotechnology for Microsystems, which is sponsored by the RCN, Division for Science, under contract no. 190086/S10. Funding for TEM time is partly funded by the project NORTEM (Grant 197405) within the programme INFRASTRUCTURE of the RCN. NORTEM was co-funded by the RCN and the project partners NTNU, UiO and SINTEF. Ida Hjorth is acknowledged for fruitful discussions and proof-reading.

Appendix A. Supplementary data

Supplementary data associated with this paper can be found in the online version at http://dx.doi.org/10.1016/j.ultramic.2016.07.004.

References

[1] J. Mannhart, D.G. Schlom, Oxide interfaces – an opportunity for electronics, Science 327 (5973) (2010) 1607–1611, http://dx.doi.org/10.1126/science.1181862.
[2] G. Hammerl, N. Spaldin, Shedding light on oxide interfaces, Science 332 (6032)

(2011) 922–923, http://dx.doi.org/10.1126/science.1206247.
[3] L.W. Martin, Y.-H. Chu, R. Ramesh, Advances in the growth and characterization of magnetic, ferroelectric, and multiferroic oxide thin films, Mater. Sci. Eng.: R: Rep. 68 (4–6) (2010) 89–133, http://dx.doi.org/10.1016/j.mser.2010.03.001.
[4] E. Dagotto, T. Hotta, A. Moreo, Colossal magnetoresistant materials: the key role of phase separation, Phys. Rep. 344 (1) (2001) 1–153, http://dx.doi.org/10.1016/S0370-1573(00)00121-6.
[5] J.-S. Lee, D.A. Arena, T.S. Santos, C.S. Nelson, S.I. Hyun, J.H. Shim, C.-C. Kao, Controlling competing interactions at oxide interfaces: enhanced anisotropy in $La_{0.7}Sr_{0.3}MnO_3$ films via interface engineering, Phys. Rev. B 85 (23) (2012) 235125, http://dx.doi.org/10.1103/PhysRevB.85.235125.
[6] M.D. Biegalski, L. Qiao, Y. Gu, A. Mehta, Q. He, Y. Takamura, A. Borisevich, L.-Q. Chen, Impact of symmetry on the ferroelectric properties of $CaTiO_3$ thin films, Appl. Phys. Lett. 106 (16) (2015) 162904, http://dx.doi.org/10.1063/1.4918805.
[7] Q. He, R. Ishikawa, A.R. Lupini, L. Qiao, E.J. Moon, O. Ovchinnikov, S.J. May, M.D. Biegalski, A.Y. Borisevich, Towards 3d Mapping of BO_6 octahedron rotations at perovskite heterointerfaces, unit cell by unit cell, ACS Nano 9 (8) (2015) 8412–8419, http://dx.doi.org/10.1021/acsnano.5b03232.
[8] J. Gazquez, S. Bose, M. Sharma, M.A. Torija, S.J. Pennycook, C. Leighton, M. Varela, Lattice mismatch accommodation via oxygen vacancy ordering in epitaxial $La_{0.5}Sr_{0.5}CoO_3$-δ thin films, APL Mater. 1 (1) (2013) 012105, http://dx.doi.org/10.1063/1.4809547.
[9] M. Basletic, J.-L. Maurice, C. Carretero, G. Herranz, O. Copie, M. Bibes, E. Jacquet, K. Bouzehouane, S. Fusil, A. Barthelemy, Mapping the spatial distribution of charge carriers in $LaAlO_3$/$SrTiO_3$ heterostructures, Nat. Mater. 7 (8) (2008) 621–625, http://dx.doi.org/10.1038/nmat2223.
[10] S.I. Khartsev, P. Johnsson, A.M. Grishin, Colossal magnetoresistance in ultrathin epitaxial $La_{0.75}Sr_{0.25}MnO_3$ films, J. Appl. Phys. 87 (5) (2000) 2394, http://dx.doi.org/10.1063/1.372191.
[11] I. Hallsteinsen, J.E. Boschker, M. Nord, S. Lee, M. Rzchowski, P.E. Vullum, J.K. Grepstad, R. Holmestad, C.B. Eom, T. Tybell, Surface stability of epitaxial $La_{0.7}Sr_{0.3}MnO_3$ thin films on (111)-oriented $SrTiO_3$, J. Appl. Phys. 113 (18) (2013) 183512, http://dx.doi.org/10.1063/1.4804312.
[12] K.J. O'Shea, D.A. MacLaren, D. McGrouther, D. Schwarzbach, M. Jungbauer, S. Huhn, V. Moshnyaga, R.L. Stamps, Nanoscale mapping of the magnetic properties of (111)-oriented $La_{0.67}$ $Sr_{0.33}MnO_3$, Nano Lett. 15 (9) (2015) 5868–5874, http://dx.doi.org/10.1021/acs.nanolett.5b01953.
[13] H. Tan, S. Turner, E. Ycelen, J. Verbeeck, G. Van Tendeloo, 2d atomic mapping of oxidation states in transition metal oxides by scanning transmission electron microscopy and electron energy-loss spectroscopy, Phys. Rev. Lett. 107 (10) (2011) 107602, http://dx.doi.org/10.1103/PhysRevLett.107.107602.
[14] K. Kimoto, T. Asaka, T. Nagai, M. Saito, Y. Matsui, K. Ishizuka, Element-selective imaging of atomic columns in a crystal using STEM and EELS, Nature 450 (7170) (2007) 702–704, http://dx.doi.org/10.1038/nature06352.
[15] N. Nakagawa, H.Y. Hwang, D.A. Muller, Why some interfaces cannot be sharp, Nat. Mater. 5 (3) (2006) 204–209, http://dx.doi.org/10.1038/nmat1569.
[16] D.A. Muller, N. Nakagawa, A. Ohtomo, J.L. Grazul, H.Y. Hwang, Atomic-scale imaging of nanoengineered oxygen vacancy profiles in $SrTiO_3$, Nature 430 (7000) (2004) 657–661, http://dx.doi.org/10.1038/nature02756.
[17] L. Yao, S. Majumdar, L. Akaslompolo, S. Inkinen, Q.H. Qin, S. van Dijken, Electron-beam-induced perovskite-Brownmillerite-perovskite structural phase transitions in epitaxial $La_{2/3}Sr_{1/3}MnO_3$ films, Adv. Mater. 26 (18) (2014) 2789–2793, http://dx.doi.org/10.1002/adma.201305656.
[18] M. Haider, H. Rose, S. Uhlemann, E. Schwan, B. Kabius, K. Urban, A spherical-aberration-corrected 200 kV transmission electron microscope, Ultramicroscopy 75 (1) (1998) 53–60, http://dx.doi.org/10.1016/S0304-3991(98)00048-5.
[19] P.D. Nellist, M.F. Chisholm, N. Dellby, O.L. Krivanek, M.F. Murfitt, Z.S. Szilagyi, A. R. Lupini, A. Borisevich, W.H. Sides, S.J. Pennycook, Direct sub-angstrom imaging of a crystal lattice, Science 305 (5691) (2004) 1741, http://dx.doi.org/10.1126/science.1100965.
[20] P.S. Sankara Rama Krishnan, A.N. Morozovska, E.A. Eliseev, Q.M. Ramasse, D. Kepaptsoglou, W.-I. Liang, Y.-H. Chu, P. Munroe, V. Nagarajan, Misfit strain driven cation inter-diffusion across an epitaxial multiferroic thin film interface, J. Appl. Phys. 115 (5) (2014) 054103, http://dx.doi.org/10.1063/1.4862556.
[21] M. Varela, M.P. Oxley, W. Luo, J. Tao, M. Watanabe, A.R. Lupini, S.T. Pantelides, S.J. Pennycook, Atomic-resolution imaging of oxidation states in manganites, Phys. Rev. B 79 (8) (2009) 085117, http://dx.doi.org/10.1103/PhysRevB.79.085117.
[22] D.A. Muller, L.F. Kourkoutis, M. Murfitt, J.H. Song, H.Y. Hwang, J. Silcox, N. Dellby, O. L. Krivanek, Atomic-scale chemical imaging of composition and bonding by aberration-corrected microscopy, Science 319 (5866) (2008) 1073–1076, http://dx.doi.org/10.1126/science.1148820.
[23] S. Nishida, S. Kobayashi, A. Kumamoto, H. Ikeno, T. Mizoguchi, I. Tanaka, Y. Ikuhara, T. Yamamoto, Effect of local coordination of Mn on Mn-L2,3 edge electron energy loss spectrum, J. Appl. Phys. 114 (5) (2013) 054906, http://dx.doi.org/10.1063/1.4817425.
[24] R.F. Egerton, P. Li, M. Malac, Radiation damage in the TEM and SEM, Micron 35 (6) (2004) 399–409, http://dx.doi.org/10.1016/j.micron.2004.02.003.
[25] L.A.J. Garvie, A.J. Craven, Electron-beam-induced reduction of Mn4+ in manganese oxides as revealed by parallel EELS, Ultramicroscopy 54 (1) (1994) 83–92, http://dx.doi.org/10.1016/0304-3991(94)90094-9.
[26] L. Houben, M. Heidelmann, F. Gunkel, Spatial resolution and radiation damage in quantitative high-resolution STEM–EEL spectroscopy in oxides, Micron 43 (4) (2012) 532–537, http://dx.doi.org/10.1016/j.micron.2011.10.006.
[27] G.A. Botton, S. Lazar, C. Dwyer, Elemental mapping at the atomic scale using low accelerating voltages, Ultramicroscopy 110 (8) (2010) 926–934, http://dx.doi.org/10.1016/j.ultramic.2010.03.008.
[28] T. Manoubi, M. Tence, M.G. Walls, C. Colliex, Curve fitting methods for quantitative analysis in electron energy loss spectroscopy, Microsc. Microanal. Microstruct. 1 (1) (1990) 23–39, http://dx.doi.org/10.1051/mmm:019900010102300.
[29] Francisco de la Pena, Pierre Burdet, Tomas Ostasevicius, Mike Sarahan, Magnus Nord, Vidar Tonaas Fauske, Josh Taillon, Alberto Eljarrat, Stefano Mazzucco, Gael Donval, Luiz Fernando Zagonel, Michael Walls, Ilya Iyengar, HyperSpy 0.8.2, 2015, http://dx.doi.org/10.5281/zenodo.28025.
[30] C.C. Ahn, P. Rez, Inner shell edge profiles in electron energy loss spectroscopy, Ultramicroscopy 17 (2) (1985) 105–115, http://dx.doi.org/10.1016/0304-3991(85)90003-8.
[31] H. Tan, J. Verbeeck, A. Abakumov, G. Van Tendeloo, Oxidation state and chemical shift investigation in transition metal oxides by EELS, Ultramicroscopy 116 (2012) 24–33, http://dx.doi.org/10.1016/j.ultramic.2012.03.002.
[32] R.F. Egerton, Electron energy-loss spectroscopy in the TEM, Rep. Prog. Phys. 72 (1) (2009) 016502, http://dx.doi.org/10.1088/0034-4885/72/1/016502.
[33] Y. Shao, C. Maunders, D. Rossouw, T. Kolodiazhnyi, G.A. Botton, Quantification of the Ti oxidation state in $BaTi_{1-x}Nb_xO_3$ compounds, Ultramicroscopy 110 (8) (2010) 1014–1019, http://dx.doi.org/10.1016/j.ultramic.2010.05.006.

Paper III

Effect of Polar (111)-Oriented $SrTiO_3$ on Initial Perovskite Growth

Ingrid Hallsteinsen, Magnus Nord, Torstein Bolstad, Per-Erik Vullum, Jos E. Boschker, Paulo Longo, Ryota Takahashi, Randi Holmestad, Mikk Lippmaa, and Thomas Tybell

Crystal Growth & Design, 16 (4), 2357–2362, 2016

CRYSTAL GROWTH & DESIGN

Article

pubs.acs.org/crystal

Effect of Polar (111)-Oriented $SrTiO_3$ on Initial Perovskite Growth

Ingrid Hallsteinsen,[†] Magnus Nord,[‡] Torstein Bolstad,[†] Per-Erik Vullum,[‡,§] Jos E. Boschker,[†,#] Paulo Longo,[⊥] Ryota Takahashi,[∥] Randi Holmestad,[‡] Mikk Lippmaa,[∥] and Thomas Tybell*[,†]

[†]Department of Electronics and Telecommunications, Norwegian University of Science and Technology (NTNU), Trondheim, 7491, Norway

[‡]Department of Physics, Norwegian University of Science and Technology (NTNU), Trondheim, 7491, Norway

[§]SINTEF Materials and Chemistry, 7456 Trondheim, Norway

[∥]Institute for Solid State Physics, University of Tokyo, Chiba 277-8581, Japan

[⊥]Gatan Inc., 5794 W Las Positas Boulevard, Pleasanton, California 94588, United States

Supporting Information

ABSTRACT: In crystalline thin film growth a prerequisite is substrate surfaces with a stable and uniform structure and chemical composition. Various substrate treatments were used to obtain atomically smooth, step-and-terrace (111)-oriented $SrTiO_3$ with uniform cation layers at the surface, i.e., single termination. The surface control enables subsequent layer-by-layer epitaxial growth of perovskite thin films of $La_{0.7}Sr_{0.3}MnO_3$, $LaFeO_3$, and $BaTiO_3$. Reflection high-energy electron diffraction and electron energy loss spectroscopy revealed that a single chemically intermixed $(A,A')BO_3$ perovskite layer formed at the interface. As the terminating layer of (111) $SrTiO_3$ is polar, a surface reconstruction consisting of TiO_x surface layers is expected, and the intermixing at the interface can be understood as A′-cations from the film material compensating an A-cation deficient substrate surface during initial growth. This finding has important consequences for engineered interfaces between perovskite thin films and polar substrate facets.

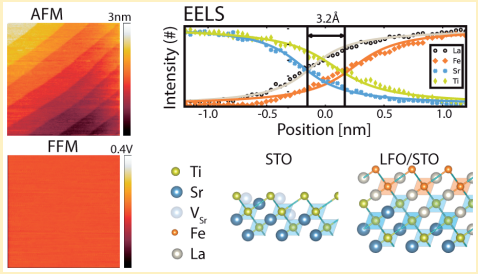

The development of atomically well-defined substrate surfaces is a major driving force behind controlled epitaxial growth and recent advances in complex oxide thin film synthesis.[1] As complex oxides exhibit strong structure−property coupling, epitaxy can be used to control the functionality of the film, utilizing strain or crystalline orientation. Different orientations of a substrate will result in interfaces where symmetry, surface polarity, and octahedral coupling differ, possibly affecting the electronic states of the epitaxial film at the interface. To exploit such effects, substrates of stoichiometric crystals with atomically flat surfaces of single termination and without major reconstructions are required.[2,3] $SrTiO_3$ (STO) and different rare-earth scandates have been widely used as substrate materials for perovskite thin film growth due to the good lattice match with materials of interest and chemical stability. The surfaces of these materials have been extensively studied since the 1990s, and high-quality (001)-oriented substrates are commercially available.[4−6] However, for (111)-oriented STO, well-defined single-terminated stoichiometric surfaces have been more difficult to obtain due to the polarity of the terminating surface.[3,7]

A schematic of the (111)-oriented STO surface is depicted in cross section and top views in Figure 1, panels a and b, respectively, where Ti is colored yellow, Sr blue, and O turquoise. The (111)-surface has a hexagonal symmetry, where the low-index in-plane crystallographic directions $[10\bar{1}]$ and $[11\bar{2}]$ are indicated in Figure 1b. Along the [111]-direction STO consists of alternating layers of SrO_3^{4-} and Ti^{4+}, which are each stacked in a "ABCABC..." manner as marked for the Ti^{4+} layers in Figure 1a,b. The distance between two equally terminated planes is $d_{111} = a/\sqrt{3} = 2.25$ Å (Figure 1a), where a represents the cubic lattice constant of STO (a = 3.905 Å). Ideally, single terminated STO(111) would solely have SrO_3^{4-} or Ti^{4+} as the uppermost layer, in the schematic a Ti-terminated layer is shown. Hence, STO(111) has layers of nominal charge +4/−4, while STO in the (001) orientation consists of layers of SrO and TiO_2 and is thus nonpolar. Since the surface energy of an ideal polar surface diverges,[8] polar surfaces tend to facet or form stabilizing reconstructions. This makes film growth on a STO(111) substrate more challenging than on nonpolar STO(001), with a tendency to form a disordered interface.[9−11]

We have earlier shown that by reducing the deposition temperature, it is possible to delay the onset of surface roughening, allowing for smooth surfaces in a certain thickness range.[12] Still, several reports point toward new phases and

Received: January 27, 2016
Revised: February 24, 2016
Published: March 1, 2016

DOI: 10.1021/acs.cgd.6b00143
Cryst. Growth Des. 2016, 16, 2357−2362

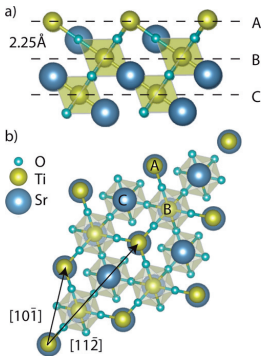

Figure 1. Schematic of an ideal cubic STO (111) Ti^{4+} terminated surface, with Ti in yellow, Sr in blue, and O in turquoise. The Ti^{4+} layers are indicated by dashed lines, and labeled A,B,C according to the "ABCABC..." stacking. (a) Cross-section view. The distance between two equivalent lattice planes is $d_{111} = a/\sqrt{3} = 2.25$ Å, where a is the cubic lattice constant of $SrTiO_3$ ($a = 3.905$ Å). (b) Top view. Arrows indicate the low-index in-plane crystallographic directions [10$\bar{1}$] and [11$\bar{2}$].

different reconstructions at the interface between a substrate and a (111)-oriented film.[7,13]

Substrates having uniform single terminations are necessary for obtaining structurally stable interfaces with a film material.[14] For (001)-oriented STO, a uniform TiO_2 termination can be achieved by selective wet etching in buffered hydrogen fluoride, which preferentially removes SrO from the surface.[4] For (111)-oriented STO there are several reported surface preparation methods pointing toward the possibility of having a stable single termination. For instance, annealing in a reducing atmosphere has been reported to give single terminated surfaces.[15] However, high-temperature treatment in a reducing atmosphere can result in oxygen deficiency, resulting in metallic conductivity and even ferromagnetic behavior.[16] Annealing in O_2-atmosphere and chemically etching with HCl/HNO_3 give a step-and-terrace surface structure with steps corresponding to 1/2 monolayer, indicating that the terminating layer alternates between the SrO_3^{4-} and Ti^{4+} layers on adjacent terraces.[17]

Several authors have reported single monolayer step-and-terrace structure for STO(111) by combining buffered hydrogen fluoride etching with high-temperature annealing in O_2 atmosphere.[18,19] As SrO_3^{-4} reacts with water to form $Sr(OH)_2$, while Ti^{4+} is not water-soluble, an almost identical result was reported by using deionized water as the etching reactant;[18,20] however the use of buffered hydrogen fluoride results in a more complete removal of Sr-related compounds.[18]

Here we present a study of how the polar surface of STO(111) influences the initial thin film growth. We discuss the effect of substrate preparation on thin film synthesis and how possible reconstructions affect the stoichiometry of the thin film/substrate interface, important for interface engineering of (111)-oriented thin films.

EXPERIMENTAL SECTION

Two different treatments of the (111)-oriented STO substrates (Shinkosha, 10 × 10 mm^2) are compared in this study, where deionized-water and buffered hydrofluoric acid are used as etching agents. Both etching chemicals have been reported to produce atomically smooth surfaces with a single terminating layer.[18] For both methods the substrates were cleaned prior to etching in acetone and ethanol for 5 min under ultrasonic agitation. Annealing was done under oxygen flow after the etching process with a ramp rate of 5 K/min. The first treatment method (DI) consists of immersing the substrates in 80 mL of deionized water at 70 °C under high ultrasonic agitation for 30 min before annealing at 1200 °C for 2 h. In the second treatment method (BHF), the substrates were immersed in deionized water at 70 °C and held under ultrasonic agitation for 5 min, before being dipped in buffered hydrofluoric acid for 45 s and rinsed in deionized water, ending with an annealing at 1050 °C for 1 h. The buffered hydrofluoric acid solution was NH_4F/HF 7:1, with a pH of 4.7. The annealing times and temperatures were chosen after optimization based on atomic force microscopy (AFM) investigations.

Ultrathin films of $La_{0.7}Sr_{0.3}MnO_3$ (LSMO), $LaFeO_3$ (LFO), and $BaTiO_3$ (BTO) were deposited by pulsed laser deposition at 520−580 °C in 0.35 mbar (0.01 mbar for BTO) of oxygen ambient with a KrF excimer laser (248 nm) at a fluence of ~2 J cm^{-2} and a repetition rate of 1 Hz. The substrate to target distance was 45 mm. After deposition the films were cooled to room temperature in 100 mbar of oxygen at a rate of 15 K/min. Reflection high energy electron diffraction (RHEED) was used to monitor the growth in situ. AFM (Veeco Nanoscope V) was used to study the surface topography. Friction force microscopy (FFM) with a cantilever spring constant of 0.9 N/m was used to study the termination of the substrates. Coaxial impact-

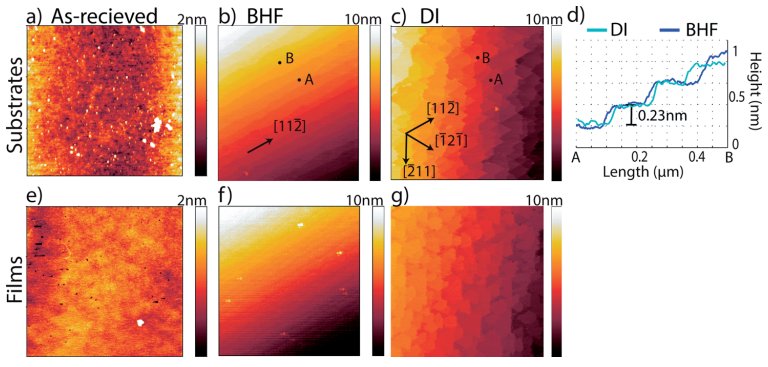

Figure 2. AFM images (tapping mode) of STO(111) surfaces with different pretreatments (a) as-received, (b) BHF, (c) DI, (d) Line profiles between points A and B extracted from (b) and (c). AFM images (tapping mode) of LSMO thin films (10 nm thick) grown on (e) as-received, (f) BHF, (g) DI treated substrates. All images areas are 3 × 3 μm^2.

DOI: 10.1021/acs.cgd.6b00143
Cryst. Growth Des. 2016, 16, 2357−2362

collision ion scattering spectroscopy (CAICISS) was used to investigate the chemical composition of the substrate surface. Scanning transmission electron microscopy (STEM) data were obtained on a double-corrected Jeol ARM200CF microscope equipped with a Gatan Quantum ER for electron energy loss spectroscopy (EELS). Cross section TEM lamellas were prepared by a FEI Helios Nanolab Dual-Beam Focused Ion Beam (FIB) using standard lift-out technique. All STEM- high angle annular dark field (HAADF) data were acquired at collection semiangles of 73−311 mrad, and for all EELS data an energy dispersion of 0.5 eV/channel and a collection semiangle of 66 mrad were used. All EELS analysis was performed using HyperSpy.[21]

RESULTS

An AFM image of an as-received substrate is shown in Figure 2a, revealing a relatively flat surface with a root-mean-square roughness of 0.36 nm. The surface is disordered with structures of multiples of half d_{111}, indicating mixed termination. Figure 2b,c shows substrate morphologies after annealing, which were pretreated with the BHF and DI methods, respectively. In both cases, ordered surfaces were obtained with a clear step-and-terrace structure. In Figure 2d AFM line scan profiles are shown for both BHF and DI treated substrates, revealing that both methods result locally in step-heights of 0.23 nm and flat terraces of 100−150 nm width, in agreement with the substrate miscut angle of 0.1°. The measured step height correspond to STO d_{111}, indicating that all terraces are terminated by identical atomic layers in accordance with the findings of Chang et al.[18]

A morphological difference is observed between substrates prepared with BHF and DI methods. The substrates pretreated with BHF (Figure 2b) reveal steps and terraces that are straight. However, substrates pretreated with DI, as in Figure 2c, have faceted step edges forming triangular sections. The step edges make a zigzag pattern, where the direction of the edge changes by 60° or 120°. On the basis of the crystal orientation of the substrate, the step edges tend to follow the crystallographic axes, as indicated in Figure 2b,c. For the BHF substrates the step edges are parallel to one of the three <11$\bar{2}$> in-plane directions in accordance with the miscut direction. This is also the case for the DI substrates, except that the step edges in this case make the zigzag pattern along all three <11$\bar{2}$> in-plane directions. We note that for STO(001) such faceted step edges have earlier been reported for Sr-rich terminations.[1] The morphologies of LSMO films of approximately 10 nm grown on as-received, BHF and DI substrates are compared in Figure 2e−g. The morphologies of the films replicate the substrate surfaces accurately, which means that the substrate surface is stable at the deposition temperature (500−600 °C) and acts as a mold for the film as long as the film grow layer by layer.[12]

To further investigate the termination and chemical composition of the substrates, friction force microscopy (FFM) was used. In Figure 3 we show the contact-mode topography and friction contrast for BHF (a, b) and DI (c, d) prepared substrate surfaces. For BHF substrates no significant friction contrast is observed, indicating no macroscopic chemical composition contrast on the surface. For the DI case, there is friction contrast visible, with two distinct levels compatible with areas of different cations. Comparing topography and friction data, it is a clear that the faceted terraces are split into triangles of different friction contrast. On the basis of comparison with FFM measurements of $SrTiO_3$ (001) surfaces, the dark contrast are inferred to be Sr-rich areas and the bright contrast Ti-rich areas.[22] AFM analysis also reveals that Sr-rich regions are rougher than the Ti-rich terraces, and

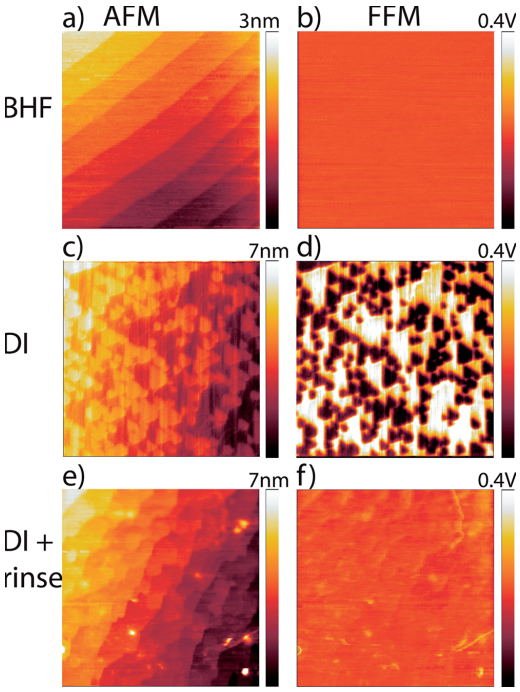

Figure 3. Contact mode AFM and FFM of STO(111) with different pretreatments: (a, b) BHF method, (c, d) DI method, and (e, f) The DI sample after an additional water rinse. The AFM and FFM images were acquired simultaneously, the image area is 3 × 3 μm^2.

that they lie approximately 1/2 and 3/2 d_{111} above the Ti-rich terraces.

One possible way for the substrate to stabilize the polar surface is by forming nonstoichiometric surface reconstructions.[3,24] Different substrate pretreatments have shown a variety of surface reconstructions on (111)-oriented STO,[25−28] where the polarity is screened by surface TiO_x layers. Angle-resolved CAICISS measurements were performed on DI and BHF treated substrates to test the chemical composition of the substrates. The time-of-flight surface composition analysis revealed increased presence of Sr on both DI and BHF prepared substrates as compared to as-received (see Supporting Information), suggesting the occurrence of Sr segregation during annealing. We note that the longer annealing time and higher annealing temperature for the DI (2 h, 1200 °C) compared to the BHF (1 h, 1050 °C) may lead to segregation of Sr,[23] and the reason for the difference in FFM. To test if the Sr signal corresponds to segregated atomic Sr on the surface, we rinsed the DI substrate with DI-water 70 °C for 2 min in ultrasonic bath, followed by 5 min on a hot plate of 100 °C to evaporate all the remaining liquids. The results shown in Figure 3e,f reveal that the faceted step-and-terrace structure is still present; however, the FFM data now gave a homogeneous contrast. We interpret this as atomic Sr being removed from Sr-rich areas, resulting in a single termination state.

In thin film epitaxy, the ad-atom mobility and possible growth mode depend on the chemical environment of the underlying layer.[1] Hence the growth of the first unit cell of a

DOI: 10.1021/acs.cgd.6b00143
Cryst. Growth Des. 2016, 16, 2357−2362

thin film on top of the substrate may indirectly identify the chemical environment of the substrate. Using substrates prepared by the BHF method and recording the intensity oscillations of the RHEED diffraction spots we investigate the growth of the first unit cells of a thin film. In Figure 4a RHEED

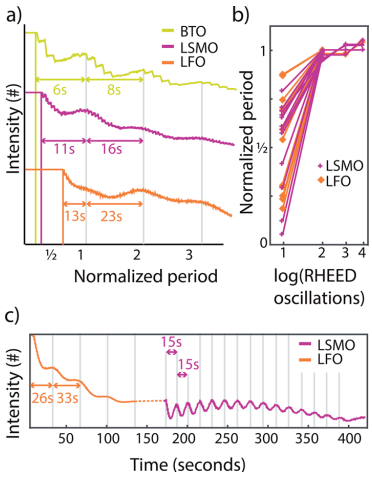

Figure 4. (a) RHEED intensity profiles for initial growth of LSMO, LFO, and BTO films on top of $SrTiO_3$(111) pretreated by BHF. The profiles are normalized to growth period. The first oscillation of all three examples has a shorter period than the rest. (b) Statistics of the period for the RHEED intensity profiles for initial growth of LSMO and LFO. The growth period is plotted against the logarithm of RHEED oscillations for clarity (c) RHEED intensity profile for a complete bilayer; LSMO/LFO/STO(111). The first oscillation for the second layer has the same growth period as the rest of the oscillations.

oscillations for different film materials are plotted. The maximum of each oscillation is taken as a complete layer, consistent with the longest intensity recovery time for each pulse indicating no phase shift.[29] For clarity the signals have been normalized to the growth period (number of laser pulses per RHEED oscillation) of each film material. As can be seen in Figure 4a, the growth period remains constant throughout the growth of the film except for the first complete layer. It is clear that for all three materials investigated here, the first RHEED oscillation is shorter than the growth period for the subsequent layers. In Figure 4b statistics for the first oscillation normalized to the growth period is shown, and the first layer has typically a growth period of 30−90% as compared to the subsequent layers. Hence, the amount of pulses needed to synthesize the first layer varies from film to film, but is observed to always be shorter than the growth period of the subsequent layers independent of film material or deposition parameters. Moreover, the growth period for the first layer is not consistent with half a period, which would indicate a change of termination, as observed for $SrRuO_3$ growth.[30,31] In Figure 4c a RHEED intensity plot for an LSMO/LFO/STO(111) epilayer is shown. It is clear that for the first LFO layer the corresponding RHEED oscillation has a shorter period (26 s) as compared to the subsequent layers (33 s). However, for the top LSMO film the first RHEED oscillation has the same period as for the subsequent layers, measured at 15 s for this particular sample. Hence we interpret that the shorter growth period at the substrate/thin film interface is an effect due to the substrate surface.

To further investigate the chemical interface between substrate and thin film, STEM and EELS investigations were performed across the substrate−film interface. The STEM data in Figure 5a indicate that the film is epitaxial, fully strained, and of high crystalline quality. Cross section composition analysis of the interface regions was obtained from EELS measurements across the LSMO/STO(111) and LFO/STO(111) interfaces, and is shown in Figure 5, panels b and c, respectively. Figure 5d

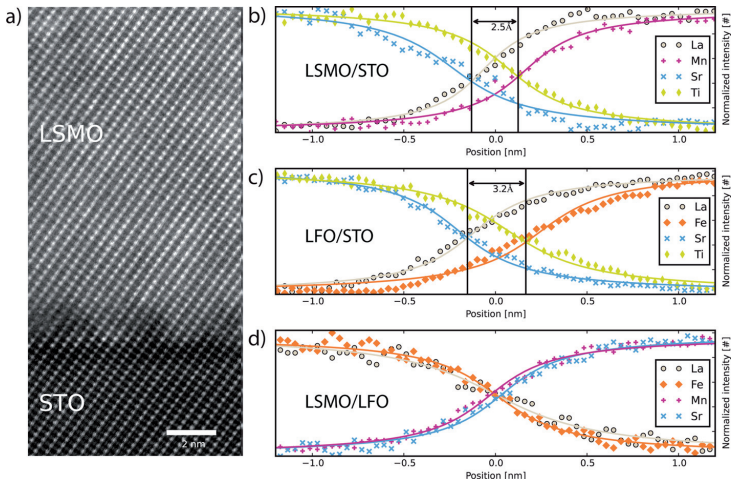

Figure 5. STEM-EELS characterization of film interfaces. (a) STEM-HAADF image of LSMO/STO(111) interface and EELS chemical line scans of (b) LSMO/STO(111), (c) LFO/STO(111), and (d) LSMO/LFO(111) interfaces. The EELS line scans has been normalized to 100% at each side of the interface.

DOI: 10.1021/acs.cgd.6b00143
Cryst. Growth Des. 2016, 16, 2357−2362

shows the LSMO/LFO(111) interface in the epilayer for comparison. For clarity the EELS intensities have been normalized to 100% at each side (see Supporting Information for non-normalized data). As can be seen, neither interface is compositionally abrupt toward the STO substrate. The signal for the substrate A-cation, Sr, decreases before the B-cation signal, Ti. Correspondingly, the A-cation signal from the thin films, La, increases before the B-cation signals, Fe/Mn, respectively. The distance between the change in A and B-cation signals is determined to be 0.25−0.3 nm, corresponding to the distance between two subsequent A-cation layers in the (111)-orientation. The spatial resolution of the EELS signal is determined to be 0.15 nm by the width of fitted Gaussian curves for the atomically resolved EELS map. Hence, the EELS measurements reveal that the layer at the interface between film and substrate is a mixture of cations, with B-cations from the substrate and A-cations from the film. Interestingly, interfaces between subsequent epitaxial interfaces grown on (111)-oriented substrates do not have this distance between A and B-cation signals (Figure 5d); hence this interface is more chemically abrupt.

Taken together, the EELS measurements reveal that the BHF substrate surfaces are Ti-rich, consistent with a surface reconstruction consisting of 1−2 TiO_x layers to screen the polarity. Figure 6a shows a model of a Sr-deficient STO(111) surface with Ti-termination, where transparent blue circles at Sr positions depict Sr-vacancies in the top two Sr-layers. The nonstoichiometric surface affects the stoichiometry of the initially grown materials on the substrate and in Figure 6b we display a model interface between a LFO thin film and the Sr-deficient STO(111) surface. As can be seen, La now fills the position of the Sr-vacancies, effectively making a one d_{111} thick distinct (La,Sr)TiO_3 perovskite layer, as confirmed by EELS (Figure 5b,c). The presence of an intermixed layer is in agreement with the RHEED data for the different systems investigated. The shorter period for the first RHEED oscillation indicate that less material is needed to fill the first layer. We note that the exact Sr surface composition will decide the period of the first oscillation, which therefore can vary from substrate to substrate. The model only takes into account crystalline atoms; hence, we do not include the potentially observed atomic surface Sr at the STO surface. We note that in this model the first B-cation layer in the film is stoichiometric with respect to the A/B ratio. This model is in accordance with reports on surface reconstructions in (111), where density functional theory and experiments show that surface TiO_x layers compensate for the polarity.[32,33]

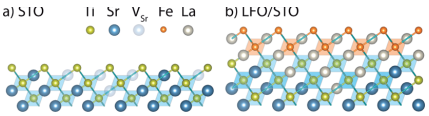

Figure 6. Model of (111)-oriented STO/film interface (a) Substrate surface with Sr-deficient top layers and (b) interface with LFO, where La-atoms has filled in the Sr-vacancies, yielding a (La,Sr)TiO_3 layer at the interface. Atoms are colored accordingly; Ti atoms are yellow, Sr blue, Sr vacancies transparent blue, La gray, Fe orange. Oxygens are shown as octahedral.

In conclusion, we have shown that the polar (111)-oriented STO surface can be pretreated to form single terminated, atomically smooth surfaces with both deionized water and buffered hydrogen fluoride, which promotes structurally abrupt interfaces and layer-by-layer film growth. However, the chemical interface between film and substrate is not abrupt, and one layer of chemical A-cation intermixing is found. We note that the effect is due to the substrate, and robust to the type perovskite thin film deposited. If the exact level of Sr surface vacancies can be controlled, the one interatomic thick (A,A′)BO_3 interface layer could be utilized to establish particular interface properties.

■ ASSOCIATED CONTENT

Supporting Information

The Supporting Information is available free of charge on the ACS Publications website at DOI: 10.1021/acs.cgd.6b00143.

More information on CAICISS analysis and non-normalized EELS data (PDF)

■ AUTHOR INFORMATION

Corresponding Author

*E-mail: thomas.tybell@iet.ntnu.no.

Present Address

#Paul-Drude-Institut für Festkörperelektronik, Hausvogteiplatz 5-7, 10117 Berlin, Germany.

Notes

The authors declare no competing financial interest.

■ ACKNOWLEDGMENTS

This project was partially supported by the Norwegian Research Council under Project Number 221860 and 231290, and by JSPS Grants-in-Aid for Scientific Research Nos. 25706022 and 26105002. M.N. is supported by the Project NORTEM (Grant 197405) within the Programme INFRASTRUCTURE of the Research Council of Norway (RCN). NORTEM was cofunded by the RCN and the project partners NTNU, UiO, and SINTEF.

■ REFERENCES

(1) Sanchez, F.; Ocal, C.; Fontcuberta, J. Tailored surfaces of perovskite oxide substrates for conducted growth of thin films. *Chem. Soc. Rev.* **2014**, *43* (7), 2272−2285.

(2) Zubko, P.; Gariglio, S.; Gabay, M.; Ghosez, P.; Triscone, J.-M. Interface Physics in Complex Oxide Heterostructures. *Annu. Rev. Condens. Matter Phys.* **2011**, *2*, 141−165.

(3) Nakagawa, N.; Hwang, H. Y.; Müller, D. A. Why some interfaces cannot be sharp. *Nat. Mater.* **2006**, *5* (3), 204−209.

(4) Kawasaki, M.; Takahashi, K.; Maeda, T.; Tsuchiya, R.; Shinohara, M.; Ishiyama, O.; Yonezawa, T.; Yoshimoto, M.; Koinuma, H. Atomic Control of the SrTiO3 Crystal Surface. *Science* **1994**, *266* (5190), 1540−2.

(5) Lippmaa, M.; Takahashi, K.; Ohtomo, A.; Ohashi, S.; Ohnishi, T.; Nakagawa, N.; Sato, T.; Iwatsuki, M.; Koinuma, H.; Kawasaki, M. Atom technology for Josephson tunnel junctions: SrTiO3 substrate surface. *Mater. Sci. Eng., B* **1998**, *56* (2−3), 111−116.

(6) Koster, G.; Kropman, B. L.; Rijnders, G.; Blank, D. H. A.; Rogalla, H. Quasi-ideal strontium titanate crystal surfaces through formation of strontium hydroxide. *Appl. Phys. Lett.* **1998**, *73* (20), 2920−2922.

(7) Blok, J. L.; Wan, X.; Koster, G.; Blank, D. H. A.; Rijnders, G. Epitaxial oxide growth on polar (111) surfaces. *Appl. Phys. Lett.* **2011**, *99* (15), 151917.

(8) Tasker, P. W. The stability of ionic crystal surfaces. *J. Phys. C: Solid State Phys.* **1979**, *12* (22), 4977.

(9) Lee, M. K.; Eom, C. B.; Tian, W.; Pan, X. Q.; Smoak, M. C.; Tsui, F.; Krajewski, J. J. Synthesis and properties of epitaxial thin films of c-

DOI: 10.1021/acs.cgd.6b00143
Cryst. Growth Des. 2016, 16, 2357−2362

axis oriented metastable four-layered hexagonal BaRuO3. *Appl. Phys. Lett.* **2000**, *77* (3), 364−366.
(10) Rubi, D.; Vlooswijk, A. H. G.; Noheda, B., Growth of flat $SrRuO_3$ (111) thin films suitable as bottom electrodes in heterostructures. *Thin Solid Films* **2009***517*, 1904−1907.10.1016/j.tsf.2008.09.106
(11) Chakraverty, S.; Ohtomo, A.; Okude, M.; Ueno, K.; Kawasaki, M. Epitaxial Structure of (001)- and (111)-Oriented Perovskite Ferrate Films Grown by Pulsed-Laser Deposition. *Cryst. Growth Des.* **2010**, *10* (4), 1725−1729.
(12) Hallsteinsen, I.; Boschker, J. E.; Nord, M.; Lee, S.; Rzchowski, M.; Vullum, P. E.; Grepstad, J. K.; Holmestad, R.; Eom, C. B.; Tybell, T. Surface stability of epitaxial La0.7Sr0.3MnO3 thin films on (111)-oriented SrTiO3. *J. Appl. Phys.* **2013**, *113* (18), 183512.
(13) Middey, S.; Rivero, P.; Meyers, D.; Kareev, M.; Liu, X.; Cao, Y.; Freeland, J. W.; Barraza-Lopez, S.; Chakhalian, J. Polarity compensation in ultra-thin films of complex oxides: The case of a perovskite nickelate. *Sci. Rep.* **2014**, *4*, 6819.
(14) Tybell, T.; Eom, C. B. Synthesis of epitaxial multiferroic oxide thin films. In *Multifunctional Oxide Heterostructures*; Tsymbal, E. Y.; Dagotto, E. R. A.; Eom, C.-B.; Ramesh, R., Eds. Oxford University Press: Oxford, U.K., 2012.
(15) Tanaka, H.; Kawai, T. Surface structure of reduced SrTiO3 (111) observed by scanning tunneling microscopy. *Surf. Sci.* **1996**, *365*, 437−442.
(16) Liu, Z. Q.; Lü, W. M.; Lim, S. L.; Qiu, X. P.; Bao, N. N.; Motapothula, M.; Yi, J. B.; Yang, M.; Dhar, S.; Venkatesan, T.; Ariando. Reversible room-temperature ferromagnetism in Nb-doped SrTiO single crystals. *Phys. Rev. B: Condens. Matter Mater. Phys.* **2013**, *87* (22), 220405.
(17) Doan, T.-D.; Giocondi, J. L.; Rohrer, G. S.; Salvador, P. A. Surface engineering along the close-packed direction of SrTiO3. *J. Cryst. Growth* **2001**, *225*, 178−182.
(18) Chang, J.; Park, Y.-S.; Kim, S.-K. Atomically flat single-terminated SrTiO3(111) surface. *Appl. Phys. Lett.* **2008**, *92*, 152910.
(19) Biswas, A.; Rossen, P. B.; Yang, C.-H.; Siemons, W.; Jung, M.-H.; Yang, I. K.; Ramesh, R.; Jeong, Y. H. Universal Ti-rich termination of atomically flat SrTiO3 (001), (110), and (111) surfaces. *Appl. Phys. Lett.* **2011**, *98* (5), 051904.
(20) Connell, J. G.; Isaac, B. J.; Ekanayake, G. B.; Strachan, D. R.; Seo, S. S. A. Preparation of atomically flat SrTiO3 surfaces using a deionized-water leaching and thermal annealing procedure. *Appl. Phys. Lett.* **2012**, *101* (25), 251607.
(21) Peña, F. d. l.; Burdet, P.; Ostasevicius, T.; Sarahan, M.; Nord, M.; Fauske, V. T.; Taillon, J.; Eljarrat, A.; Mazzucco, S.; Donval, G.; Zagonel, L. F.; Walls, M. *hyperspy: HyperSpy 0.8.2*.
(22) Iwahori, K.; Watanabe, S.; Komeda, T.; Kawai, M.; Saito, A.; Kuwahara, Y.; Aono, M. Force Microscopy Study of SrTiO 3 (001) Surfaces with Single Atomic-Layer Steps. *Jpn. J. Appl. Phys.* **1999**, *38* (6S), 3946.
(23) Ohnishi, T.; Shibuya, K.; Lippmaa, M.; Kobayashi, D.; Kumigashira, H.; Oshima, M.; Koinuma, H. Preparation of thermally stable TiO2-terminated SrTiO3(100) substrate surfaces. *Appl. Phys. Lett.* **2004**, *85* (2), 272−274.
(24) Russell, B. C.; Castell, M. R. Surface of Sputtered and Annealed Polar SrTiO3(111): TiOx-Rich (n × n) Reconstructions. *J. Phys. Chem. C* **2008**, *112*, 6538−6545.
(25) Chiaramonti, A. N.; Lanier, C. H.; Marks, L. D.; Stair, P. C. Time, temperature, and oxygen partial pressure-dependent surface reconstructions on SrTiO3(1 1 1): A systematic study of oxygen-rich conditions. *Surf. Sci.* **2008**, *602* (18), 3018−3025.
(26) Haruyama, Y.; Aiura, Y.; Bando, H.; Nishihara, Y.; Kato, H. Annealing temperature dependence on the electronic structure of the reduced SrTiO3 (111) surface. *J. Electron Spectrosc. Relat. Phenom.* **1998**, *88*−*91*, 695−699.
(27) Tanaka, H.; Kawai, T. Surface structure of reduced SrTiO3(111) observed by scanning tunneling microscopy. *Surf. Sci.* **1996**, *365* (2), 437−442.
(28) Yin, Y.; Wang, J.; Zhu, H.; Lv, K.; Wu, X. S. Structural distortion and charge redistribution in $SrTiO_3$ (111) polar surfaces. *Vacuum* **2015**, *120* (Part A), 83−88.
(29) Sullivan, M. C.; Ward, M. J.; Gutiérrez-Llorente, A.; Adler, E. R.; Joress, H.; Woll, A.; Brock, J. D. Complex oxide growth using simultaneous in situ reflection high-energy electron diffraction and x-ray reflectivity: When is one layer complete? *Appl. Phys. Lett.* **2015**, *106* (3), 031604.
(30) Rijnders, G.; Blank, D. H. A.; Choi, J.; Eom, C.-B. Enhanced surface diffusion through termination conversion during epitaxial SrRuO3 growth. *Appl. Phys. Lett.* **2004**, *84* (4), 505−507.
(31) Chang, J.; Park, Y.-S.; Lee, J.-W.; Kim, S.-K. Layer-by-layer growth and growth-mode transition of SrRuO3 thin films on atomically flat single-terminated SrTiO3 (111) surfaces. *J. Cryst. Growth* **2009**, *311*, 3771−3774.
(32) Herger, R.; Willmott, P. R.; Bunk, O.; Schlepütz, C. M.; Patterson, B. D.; Delley, B.; Shneerson, V. L.; Lyman, P. F.; Saldin, D. K. Surface structure of $SrTiO_3$(001). *Phys. Rev. B: Condens. Matter Mater. Phys.* **2007**, *76* (19), 195435.
(33) Marks, L. D.; Chiaramonti, A. N.; Rahman, S. U.; Castell, M. R. Transition from Order to Configurational Disorder for Surface Reconstructions on $SrTiO_3$(111). *Phys. Rev. Lett.* **2015**, *114* (22), 226101.

DOI: 10.1021/acs.cgd.6b00143
Cryst. Growth Des. 2016, 16, 2357−2362

Paper IV

Atomap: a new software tool for the automated analysis of atomic resolution images using 2-dimensional Gaussian fitting

Magnus Nord, Per Erik Vullum, Ian MacLaren, Thomas Tybell, and Randi Holmestad

Submitted to Advanced Structural and Chemical Imaging

Atomap: a new software tool for the automated analysis of atomic resolution images using 2-dimensional Gaussian fitting

Magnus Nord[1,2,*] Per Erik Vullum[1,3] Ian MacLaren[2]
Thomas Tybell[4] Randi Holmestad[1]

[1]Department of Physics, Norwegian University of Science and Technology, Trondheim, Norway.

[2]School of Physics and Astronomy, University of Glasgow, Glasgow, United Kingdom.

[3]Materials and Chemistry, SINTEF, Trondheim, Norway.

[4]Department of Electronics and Telecommunications, Norwegian University of Science and Technology, Trondheim, Norway.

Abstract

Scanning transmission electron microscopy (STEM) data with atomic resolution can contain a large amount of information about the structure of a crystalline material. Often this information is hard to extract, due to the large number of atomic columns and large differences in intensity from sublattices consisting of different elements. In this work we present a free and open source software tool

*Corresponding author: magnunor@gmail.com

for analysing both the position and shapes of atomic columns in STEM images, by using 2-D elliptical Gaussian distributions. The software is tested on variants of the perovskite oxide structure. By firstly fitting the most intense atomic columns then subtracting them, information on all the projected sublattices can be obtained. From this, we can extract changes in the lattice parameters and shape of A-cations from annular dark field images of perovskite oxide heterostructures. Using annular bright field images, shifts in oxygen column positions are also quantified in the same heterostructure. Also, the precision of determining the position of atomic columns is compared between STEM data acquired using standard acquisition, and STEM images obtained as an image stack averaged using non-rigid registration.

Keywords: Quantitative STEM, strain mapping, image processing, oxygen octahedral distortion, non-rigid registration

1 Background

Scanning Transmission Electron Microscopy (STEM) together with correction of geometric aberrations in the probe forming optics allow routine acquisition of atomic resolution images with sub-Å resolutions [1, 2]. These images contain a wealth of information about the crystal structure of a material. Specifically: (i) The position of the atom columns in High Angle Annular Dark Field (HAADF) images can be determined quantitatively and used for structure solution [3–6] and structure of defects [7]. (ii) The position of the atom columns can be used to get local changes of lattice parameters [8]. (iii) In HAADF STEM the intensity of an atomic column is related to the atomic number of the elements in the atomic columns, and the number of atoms in the columns [9]. Simulations are often needed to interpret the intensity quantitatively as there are complicating effects from sample orientation [10], material phase [10], defects [11] and strain

[12] in the material. By combining HAADF STEM with simulations one can extract compositional and thickness information, in some cases even counting all the atoms [10]. (iv) Even information about the structure parallel to the electron beam can be inferred from the shape of the columns [13]. With the wealth of information in these images, having robust and quantitative methods for analysing them is just as important as acquiring them.

In addition to STEM-HAADF imaging, which is best for heavier elements, it is also important to be able to image and quantify the positions of lighter elements. For example, in perovskite oxides it is vital to be able to accurately map the position of the oxygen columns [14]. In recent years, STEM imaging using either Bright Field (BF) [8, 15, 16] or Annular Bright Field (ABF) [17, 18] conditions has been useful for revealing oxygen atom columns in such oxides.

Of special interest is the oxygen structure across interfaces in heterostructures [19], since this is very hard to probe with other techniques. In perovskite oxides the oxygen positions can be used to infer the oxygen octahedral tilting pattern [20], which is important for understanding the macroscopic functional properties of the material, and may well be affected by constraints from coherent interfaces [8, 18].

A commonly used method for quantifying changes in lattice parameter is geometrical phase analysis (GPA) [21]. GPA is based on Fourier transforming atomic resolution images and placing masks around two non-collinear Bragg spots. Historically, this method has been used with High-Resolution TEM (HRTEM) [21, 22]. However, with the advent of STEM aberration correctors it has also seen extensive use on STEM-images [5, 6, 23]. While this is a fast and easy way to calculate deformation of a lattice, it can introduce artefacts and the spatial resolution is limited to 1 unit cell [23] due to it being based on Fourier transforming the image data. Ideally it would be preferable to use real space

methods, which do not require the use of Fourier transforms. One possibility is to use the centre of mass for each bright column which is usually robust [24], but this has the limitation that it only gives the centre positions of the atomic columns. Alternatively, the fitting of a 2-D Gaussian to the bright column will give both the width, ellipticity, amplitude and more precise centre position [24]. But for this to work successfully, reasonable initial values are needed.

Several software tools for real space analysis exist: Ranger [25], qHAADF [26], iMtools [27], StatSTEM [28] and Oxygen octahedra picker [29]. These methods have been used in several works: using centre of mass combined with principal component analysis (PCA) [13], pattern matching [30], iMtools using 2-D Gaussians [4, 31], and Matlab with the Image Processing Toolbox [10]. Recent work has also used computer vision based techniques to characterize the local structure [32].

Since STEM images can show several thousand atomic columns, automation is an important aspect for analysis methods. Ideally such methods should require as little manual input as possible, since this allows analysis of large images containing several thousand atomic columns. This is important for three reasons: (i) the more information, the better, (ii) researcher time is valuable, computing time is cheap, (iii) large sample sizes allows for a more statistical approach to data analysis. The automation should ideally do the peak finding and position refinements. In addition, it should also construct relations between the atoms. For example, for an image of a monocrystalline material, the atoms belonging to the same monolayer should automatically be identified. This enables rapid analysis of parameters like distances between monolayers, and changes in lattice parameters.

In addition, this framework should be free and open source [33]. This avoids the processing steps being hidden in a "black box", and allows for other re-

searchers to improve and extend the functionality.

In this work we present Atomap, a new free and open source software package for automatic analysis of the position and shape of atomic columns in STEM images. By using a variety of peak finding and position refinements, even light elements such as oxygen can be accurately quantified. We start by outlining the method by showing the different processing steps on a $SrTiO_3$ (STO) substrate. Next, the method is applied to extract structural information from different perovskite oxide heterostructures. In specific, the position of sublattices in the crystal structure, the shape of atomic columns and superstructures in oxygen atomic planes are determined.

2 Computational and Experimental Methods

The focus of this work is the analysis of atomic resolution STEM images of perovskite oxides. These materials are in the form of ABO_3. The A-site is a larger cation like strontium or lanthanum, the smaller B-site is typically a transition metal like manganese or titanium, and the O is oxygen. A-site cations are usually the heaviest element in the structure, the B-site cations the second heaviest, and oxygen the lightest. The heterostructures studied were $La_{0.7}Sr_{0.3}MnO_3$ (LSMO) on $LaFeO_3$ (LFO) on (111)-oriented STO:Nb and LSMO on (111)-oriented STO:Nb. TEM-samples were prepared as thin sections perpendicular to the $[1\bar{1}0]$-direction of the STO. Deposition [34,35] of the films and the preparation of the TEM specimens [36] are described in more detail elsewhere.

An example of a typical STEM image is shown in Fig. 1 (top left). The first aim of the method is to extract the position and shape for all the different atomic columns in these kinds of images. Secondly, we want to find the relations between the different atomic columns. In essence, the process of fitting one sublattice can be summed up in 3 steps: i) Find the positions of all the atomic

columns you want to examine. ii) Refine the positions using center of mass until they are close enough for the 2-D Gaussian fitting to work robustly. iii) Fit the atomic columns using a 2-D elliptical Gaussian function $I(x, y)$. This is defined by,

$$I(x,y) = I_0 + A\exp\left(-\left(a(x-x_0)^2 - 2b(x-x_0)(y-y_0) + c(y-y_0)^2\right)\right) \quad (1)$$

$$a = \frac{\cos^2\theta}{2\sigma_x^2} + \frac{\sin^2\theta}{2\sigma_y^2}$$

$$b = -\frac{\sin 2\theta}{4\sigma_x^2} + \frac{\sin 2\theta}{4\sigma_y^2}$$

$$c = \frac{\sin^2\theta}{2\sigma_x^2} + \frac{\cos^2\theta}{2\sigma_y^2}$$

where I_0 is the background, A the amplitude, x_0, y_0 the center positions, σ_x, σ_y the sigmas and θ the rotation. The background I_0 is set to the minimum intensity value of the region around the atomic column.

Additional sublattices are found by having *a priori* knowledge on where they are located in relation to the first sublattice, as explained below.

2.1 Initial positions and refinements

To exemplify this we show the procedure to find the positions of all sublattices in a STO crystal projected along the $[1\bar{1}0]$-direction. While this demonstrates the use of this method on a specific crystal structure along a specific projection, the software should work for any kind of atomic structure or projection, as long as the atomic columns are clearly resolved. Comments on how to adapt this for other structures and projections are outlined in section 2.5.

2.1.1 A-cations

Firstly the original ADF image (Fig. 1, top left) is filtered. This involves doing a local averaging, where a Gaussian convolution of the image is made and subtracted from the original image. Next, 1-D PCA [37] denoises the modified image to reduce random noise. The outcome is a filtered ADF image with flatter contrast and less noise. The A-cations in the filtered ADF image are located by using a peak finding method which finds the most intense local features, where each feature has be to separated by a minimum distance.

Next, these initial A-cation positions are refined by using the original ADF image. This is done by finding the center of mass for a circular area centered at the current position with a radius of 40% of the distance to the closest A-cation neighbor. The result of this refinement is shown in the "A-cation positions" image in Fig. 1. These A-cation positions are used as initial values for fitting 2-D Gaussians to every A-cation atomic column in the original ADF image.

The refined positions of the A-cations are the input parameters to further determine the 2-D symmetry of the atomic structure. For each A-cation the distance and direction to the 10 nearest neighbors are calculated. Next, using a similar peak finding process as explained earlier, all the repeating nearest neighbors are found. The "Nearest neighbor statistics" to the bottom left in Fig. 1 shows the real space nearest neighbor distance and direction, which give information similar to an FFT: the 2-D symmetry of this specific projection of the 3-D crystal structure. In essence, this gives all the major crystallographic directions perpendicular to the electron beam. Using these unique crystallographic directions, atom columns which belong to the same atom planes are grouped. This collection of atom columns is called an atom plane, and in one image there will be many parallel atom planes. These atom planes are defined by a vector perpendicular to the line spanned by the collection of atomic columns. Thus,

the atom planes shown in Fig. 1 (bottom left) are called the (110) atom planes. The line spanned by these atom planes are in the [001]-direction. If we consider 6 different crystallographic directions, we'll get 6 different groups of parallel atom planes, and each atom column will be in 6 different atom planes.

2.1.2 B-cations

Fitting Gaussians to the B-cations is more challenging, due to the A-cations being more intense. To get robust fitting of the B-cations, the intensity from the A-cations is removed from the original ADF image. This is done by subtracting the 2-D Gaussians fitted to the A-cations. The original ADF image with the A-cations subtracted is shown in the top centre of Fig. 1. This leaves the B-cations as the most intense feature in the ADF image.

The initial positions of the B-cation atomic columns are placed between each A-cation pair in the (110) atom planes. This is shown for one A-cation atom plane in Fig. 1 (bottom left), with the B-cation initial positions marked with red circles.

Using the initial B-cation positions and the ADF image with the A-cations removed, the B-cation positions are refined using center of mass the same way as for the A-cations. The refined positions are used as initial values when doing Gaussian fitting for the B-cations. The 2-D symmetry and atom planes for the B-cations are constructed in the same way as for the A-cations. This process is shown in the middle column of Fig. 1, where the resulting B-cation (001) atom planes are shown.

2.1.3 Oxygen

The rightmost column in Fig. 1 shows how the oxygen positions are determined. The oxygen initial positions are placed between each pair of B-cations in the (001) atom planes, shown with the blue circles in the lower center image in Fig.

1. In ADF imaging the oxygen is much less intense compared to the heavier A and B cations, so ABF imaging is utilized. Such an image is shown to the top right in Fig. 1 (Original ABF), which has been acquired simultaneously with the ADF image. In the ABF image the oxygen is visible, but still the least intense of the atomic columns. Using the initial A and B cation positions from the ADF image, 2-D Gaussians are fitted to the A and B cations in the ABF image and subtracted. The image contrast is further inverted, to create a modified ABF image where the oxygen columns are the most intense features in the image. Using this modified ABF image and the initial oxygen positions, the positions are refined using the center of mass, fitting the 2-D Gaussians and finding the 2-D symmetry.

The end result gives the location of all the atom columns in the image, as shown to the lower right in Fig. 1.

2.2 Finding distances between atomic columns

Having an accurate position for all the atomic columns is the first step towards making measurements of distances between columns or interplanar spacings. Having already grouped the atom columns into atomic planes, it is trivial to find the spacings in the (001)- and (110)-planes. The distances between neighbouring atomic columns in the (001)-planes correspond to the (110) interplanar spacing as these are orthogonal (Fig. 2a). Similarly, the interplanar distances for the (110)-planes are found by using the distances between the atomic columns in the (001)-planes. The case is less straightforward for (111)-planes, as neighboring atomic columns (of the same cation type) along the orthogonal $(11\overline{2})$-plane will be 3 monolayers apart. The interplanar spacing is the distance between one monolayer and its neighbor. To find this, a line is interpolated through the atomic columns in a (111)-plane. From an atomic column in the neighbouring

(111)-plane, the shortest distance from the atomic column to this line is found. This is the (111) interplanar spacing at this point, as shown to the bottom right in Fig. 2a. Repeating this for every atomic column and its neighbor atom plane gives a 2-D map of the monolayer distances.

In the perovskites, a common structural change is unit cell doubling along a specific direction as a result of oxygen octahedral tilting [20]. Depending on the tilt pattern, this will result in the oxygen columns shifting. An example of this is shown in Fig. 2b, where there is an obvious oxygen superstructure along the black line signified by alternating distances between the oxygen columns in the [001]-direction. One useful way of quantifying this is finding how much the oxygen atom deviates from the centrosymmetric position in a cubic perovskite structure. This displacement, D, is found by determining the distance from an atom to the next (N) and the previous (P) atoms in the atom plane, and divide the difference (N-P) by 4. This gives the distance the oxygen atom deviates from a centrosymmetric position, and is shown in the inset in Fig. 2b. For a cubic structure D is 0, while for bulk LFO D is 0.39 Å.

2.3 Atomic column shape

Having fitted every atomic column with a rotating elliptical 2-D Gaussian (Eq. 1), one can extract information about the shape of the atomic column. This shape can reveal information about the structure parallel to the electron beam [19], and in some materials the position of light elements by using the shape of the heavier atomic columns [13]. With the 6 parameters defined in Eq. 1, one can use the σ_x and σ_y to calculate the ellipticity for the atomic column which is a measure of how elongated the atomic column is. We define the ellipticity

(ϵ) as,

$$\epsilon = \begin{cases} \frac{\sigma_x}{\sigma_y}, & \text{if } \sigma_x > \sigma_y \\ \frac{\sigma_y}{\sigma_x}, & \text{if } \sigma_y > \sigma_x \end{cases} \tag{2}$$

giving an ϵ which always is greater or equal to 1. An ϵ of 1 would be a perfectly circular atomic column, while $\epsilon = 2$ is an atomic column where one side is twice as long as the other side.

Similarly, one can use θ to find the direction of the ellipticity. We define this direction as ρ,

$$\rho = \begin{cases} \theta, & \text{if } \sigma_x > \sigma_y \\ \theta + \frac{\pi}{2}, & \text{if } \sigma_y > \sigma_x \end{cases} \tag{3}$$

which means ρ will be the angle between the positive x-axis and the longest σ. In addition, ρ will always be between 0 and π due to the symmetry of the 2-D Gaussian.

2.4 The software implementation

This program is implemented in the Python (3.x) programming language, and both the source code and instructions on how to install it is available at `http://atomap.org`. It relies heavily on the fitting and modelling routines implemented in HyperSpy [38]. Currently the program is optimized for analysing STEM-images of perovskite oxides materials projected along a <110> direction. However, it is trivial to adapt it for any structure as discussed below in section 2.5. Extending the code should be easy, and requests for both new features and assistance in adapting for other structures are welcome on the issue tracker (`http://atomap.org/issue`) or by email to the corresponding author. The software and source code is distributed under the free and open source GNU General Public License v3.0.

The program is sorted into several classes: **atom_position**, **atom_plane**, **sublattice** and **atom_lattice**. **atom_position** is the position of a single atomic column, and contains variables like position, σ, θ, and other information about the shape of the atomic column. **atom_plane** contains all the **atom_positions** which belong to the same atomic plane. **sublattice** contains all the **atom_positions** and **atom_planes** belonging to the same sublattice, like the A-cations in Fig. 1. **atom_lattice** contains all the **sublattices**, so in Fig. 1 this would include the A-cations, B-cations and oxygen sublattices. The **atom_lattice** class can be saved and loaded, saving all the **atom_position** parameters.

One current limitation is that the whole image given to the program must have a similar crystal structure. For example a perovskite heterostructure shown in Fig. 4, 5 and 6 works fine, due to the structures being sufficiently similar. A perovskite oxide film grown on Si would however not work. Similarly, if there are any amorphous parts in the image, local bright features could be identified as atomic positions by the peak finding function. One simple solution is to crop the images, so only the same crystal structure is within the image given to the program. This could probably be automated, which would allow for automatic determination of regions with different structures. For example in an aluminium alloy, one would be able to automatically figure out which regions are aluminum matrix and which are precipitates.

2.5 Adapting for other structures and projections

The first step in using the program is finding a value for the smallest separation for the first sublattice. It is important to find a good value for this variable, as having either too many or too few atoms in the first sublattice will confuse the symmetry finder. In the example discussed in section 2.1, this value is half the

separation between the A-cations in the $[1\bar{1}0]$-direction. The projected (110) spacing is 2.76 Å for STO. However, half the value (1.38 Å) did not work very well, which is caused by the scanning distortions and sample drift image during acquisition. So a value slightly less than half the smallest separation should work reliably. For the STO in Fig. 1: approximately 1.3 Å. This value is used for the atom column separation in the peak finding function. For only fitting a single sublattice, this will be enough for the program to work.

Finding a second sublattice requires some *a priori* knowledge. For a perovskite oxide in the $[1\bar{1}0]$-projection (Fig. 1), one would specify that the atoms in the second sublattice are found between the atom columns in the (110)-atomic planes for the first sublattice.

All this is documented on the webpage (`http://atomap.org`), which includes examples for how to do this.

3 Results and discussion

To test the processing method, datasets from epitaxial perovskite oxide heterostructures are used. Firstly, the effects of imaging conditions and image registration on the results are tested. Then, a comparison is made between the current method and GPA. Finally, the fitting of non-circular elliptical columns is tested.

All directions and atom planes are given in the pseudocubic coordinate system.

3.1 Uncertainty and reducing scanning distortions

It is clear that the reliability and the uncertainty of the peak fitting technique will be connected to how clearly the different atomic columns can be resolved. An important aspect of this is scanning distortions, as the electron probe is

susceptible to both mechanical, electrical and magnetic disturbances, both from noise within the microscope system, as well as extraneous disturbances from the surrounding environment, and these will have some influence, even in the best designed microscope rooms [39]. One way to reduce the effects of these distortions is to acquire several fast images of the same area, register them and sum them afterwards [39]. In earlier studies, this was simply performed by rigid registration of the images, which takes out the effect of any drift, and simply averages out any local distortions (at the cost of a slight deterioration of the resolution) [4]. A better approach is to perform rigid registration to remove the effects of drift, followed by non-rigid registration to remove the effects of short period instabilities in the scanning system [40, 41]. To investigate the effect of short acquisition and alignment, as opposed to recording a single scan at a longer dwell time, we analysed two different STEM-ADF images from the same session taken along the $[1\bar{1}0]$ cubic direction of a sample of STO: (i) acquired as a single image using a pixel dwell time of 38.5 µs (line synced) with the image shown in Fig. 3a. (ii) acquired as an image stack of 20 images with dwell time of 2 µs per pixel (i.e. almost the same total acquisition time per pixel) which is then processed using Smart Align [41]. This aligned stack is shown in Fig. 3b. Clearly, the aligned stack appears a little sharper and less noisy than the single long acquisition image, but to quantify the effects of this difference on atom spacing measurements, the images were quantified as set out above in Sec. 2.2 and some comparative results are shown in Fig. 3c-h. A distribution of distances between the atoms parallel to the [111] (vertical in image) and $[11\bar{2}]$ (horizontal in image) crystallographic directions of STO are shown in Fig. 3(c) and (d): these directions are parallel to the slow and fast scan directions, respectively. As these data are from a region of a pure STO sample far away from any interfaces, there should be no variations in the distance between the

planes. Therefore, these plots should be essentially a measure of the uncertainty in the measurements, which we define as one standard deviation in the spread of the distances. The difference between the single scanned image and the Smart Align image is very obvious, especially for the slow scan direction. In this case, the uncertainty is reduced from $\approx$ 16 pm to 7 pm. For the fast scan direction, the reduction in uncertainty is much less: from 7.5 to 5.9 pm.

Similar measurements for distances between the atomic planes in the slow and fast scan direction is shown in Fig. 3e and f, respectively. Compared to (c) and (d), this is in effect averaging over many atomic columns. The uncertainty in the slow scan direction for the single scanned image is clearly much larger, and comparing the normal and Smart Align datasets, there is a massive reduction in the uncertainty from about 7 pm to 1 pm. For the fast scan direction, the uncertainty in the single scan image is less, as might be expected, although there is a big negative spike at one point, which is typical for the kind of local disturbance that often arises in atomic resolution images. In this case, the uncertainty is reduces from about 5 pm to 1 pm. Thus, it should be possible using non-rigid registration to make measurements of A-site (or other heavy, bright atom) plane spacings with about 1 pm precision.

One interesting effect is the decrease of uncertainty between the individual atomic columns and atomic planes for the single scanned image and the Smart Align image. For the fast scan atomic column uncertainty there is a small improvement for the aligned stack (7.5 to 5.9 pm). While for the atomic planes uncertainty there is a much larger improvement (5 to 1 pm). This is most likely due to the scanning distortions being correlated when acquiring a single scanned image using line synchronization. When acquiring an image stack with a short pixel dwell time of 2 µs these scanning distortions are much less correlated. Since finding the distances between the atom planes consist of averaging the positions

of many atomic columns, the uncorrelated noise in the image stack is averaged out.

Lastly, the interplanar spacings for the different sublattices are shown in Fig. 3g and h. Here, a similar STO Smart Align ADF dataset has been used to estimate the A- and B-cation uncertainty levels, and an ABF dataset has been used to estimate the oxygen uncertainty levels. The average distances between the interplanar spacings are calculated for the A-cations, B-cations and oxygen. For all atom types in both fast and slow scan directions, the uncertainty is about 1.0-1.4 pm.

In view of the fact that the non-rigid registration method gives clearly superior results, all datasets in the following sections are acquired as image stacks and processed using Smart Align, then processed using the method outlined in section 2.1.

3.2 Strain analysis: Comparison to GPA

As stated in the introduction, GPA is a commonly used technique for characterizing distances between atomic columns in atomic resolution (S)TEM images [21]. Fig. 4 shows a comparison between GPA and the method explained in this work, for an epitaxial LSMO/STO-(111) heterostructure. (a) shows a STEM-ADF image and FFTs from the LSMO (top inset) and STO (bottom inset). The fast Fourier transform (FFT) of the LSMO region have extra $\{\frac{1}{2}\frac{1}{2}\frac{1}{2}\}$ spots (circled in red) which are not present in the STO region. These superstructure spots indicate doubling of the unit cell along the [111]- and $[11\overline{1}]$-directions in the LSMO. GPA is performed by using the {111} and $\{11\overline{2}\}$ FFT spots utilizing the STO substrate far away from the interface as a reference. This data is then summed in the [111]-direction, giving the average out-of-plane distance as a function of distance from the LSMO/STO-interface (Fig. 4b, green dashed

line). Using the method explained in section 2.2, the average distance between the A-cation monolayers in the [111]-direction is calculated as a function of the distance from the interface (Fig. 4b, blue line). Comparing the two line profiles, they both show the same general trends: larger lattice size in the STO, and smaller in the LSMO, with a slight lattice size increase at about 8 nm into the film. However, the unit cell doubling observed in the FFT is only visible in the real space method. This is due to the choice of the mask in the GPA, since the one used to get the data in Fig. 4 did not include the superstructure spots. It could be possible to use the $\left\{\frac{1}{2}\frac{1}{2}\frac{1}{2}\right\}$ spots to do the GPA, instead of the $\{111\}$ and $\{11\bar{2}\}$. This could show the presence of the unit cell doubling, but the regions where these peaks are not present would not yield any information. For example the STO substrate, and the regions in the LSMO film without the unit cell doubling.

3.3 Mapping oxygen octahedral tilting

Fig. 5a shows an ABF image of the LSMO/LFO/STO-(111) heterostructure, where there is a "zig-zag" pattern of the oxygen columns along the [110]-direction in the LFO layer. This displacement from the centrosymmetric position can be quantified using the method discussed in section 2.2. An example of this is shown in Fig. 5b, where the [001]-direction displacement is calculated for all the oxygen columns. The displacement in the LFO layer takes the form of an alternating long and short displacement in the [001]-direction. To give a better visualization, the displacement is set to zero at the A-cation positions, leading to the checkerboard pattern seen in Fig. 5b. An average of the displacements as a function of distance from the LFO/STO interface is shown in Fig. 5c. This shows both a clear superstructure and the variation in the displacement across the film. This can then be used to infer parameters such as the octahedral

tilting pattern and bond angles.

One important caveat with using ABF imaging is the relationship between real and measured atom column positions is not always intuitive [42]. For example, if the sample is slightly tilted off the zone axis the atomic positions can shift. This effect varies with respect to thickness, atomic number, collection angle and convergence angle [42]. Thus to properly analyse the atomic positions, image simulations coupled with careful considerations of the experimental parameters are required. However, the measured atomic positions are still useful as first approximations, even if further work with image simulations is required to ensure that the conclusions are robust.

3.4 Ellipticity

As discussed in section 2.3, one can also use the shape of the atomic columns to extract structural information [13]. An example of this is seen in Fig. 6a, which shows A-cation ellipticity in the LSMO/LFO/STO-(111) heterostructure imaged using STEM-ADF. In the LFO layer there is a clear elongation of the A-cation sites, annotated with the blue ellipses. By fitting elliptical 2-D Gaussians (Eq. 1) to every A-cation, this elongation can be quantified with ϵ (Eq. 2) and ρ (Eq. 3). Where ϵ is $\frac{\sigma_{Longest}}{\sigma_{Shortest}}$, and ρ is the angle between the positive x-axis and $\sigma_{Longest}$. Having these values for every A-cation, one can visualize these in a vector plot (Fig. 6b). Here, the length of the arrows is given by ϵ, and the direction by ρ. There is a clear difference in the LFO-layer, which has an elongation close to the [111]-direction. This is even more apparent with the vector plot Fig. 6c and the ϵ plot in Fig. 6d, which takes the average of the data as a function of distance from the interface. The ellipticity is constant in the STO substrate until the LSMO/STO-interface, where it increases to its maximum about 2 nm into the film, and decays gradually in the LSMO film to

the same level as in the STO substrate.

As discussed in section 2.3, there are many different variables which can affect ellipticity of the atomic columns. So for the vector plots in (b) and (c), a systematic average ϵ and ρ "background" has been subtracted. This noise level was determined from the STO substrate ($\approx 0.12\ \epsilon$ in the [111]-direction), where the ellipticity should be 1. This systematic background is most likely due to a variety of factors: sample drift, misalignment, having the sample slight off-axis and residual scanning distortions. Especially the latter is present in this dataset, as horizontal "streaks" visible in some of the atomic columns (Fig. 6a). These are still present, even though the image was made by averaging an image stack. This is due to the fast scan being in the same direction for all the images in the image stack. One solution is rotating the fast scan direction by 90 degrees in every second image in the image stack, which will average out this scanning distortion. Another effect can be the 2-D Gaussian fitting itself, where overlap from the neighboring atomic columns can influence the fitting. For example in Fig. 6, the B-cations might add a slight component towards the [001]-direction.

4 Conclusion

In summary, we have developed a free and open source software package for automatically quantifying the positions and shapes of atomic columns in atomic resolution STEM images. By utilizing a model based approach with 2-D Gaussians the most intense atomic columns are subtracted, and all the sublattices in a STEM image can be analysed separately. Furthermore, the projected 2-D symmetry is automatically extracted by finding the major symmetry axes. This is used to organize the atomic columns in atomic planes, which facilitates the analysis of interplanar distances. By using images where the scanning distortions had been reduced using non-rigid registration, a precision of 6 pm could be

obtained for distances between single atomic columns, and 1.2 pm for distances between atomic planes.

The software has been tested on HAADF and ABF STEM images of perovskite oxide heterostructures. The displacement of oxygen columns in ABF images was quantified. By using elliptical 2-D Gaussians, the projected shape of the A-cation atomic columns was extracted. The software should be easily adaptable for any atomic resolution STEM image, as long as the atoms are clearly resolved.

5 Acknowledgement

We acknowledge Bernhard Schaffer for developing the StackBuilder script plugin for Digital Micrograph, which was used for acquiring image stacks for processing using Smart Align, and Duncan Johnstone for implementing support for modelling 2-D data in HyperSpy. We also acknowledge Lewys Jones for help and support in how to use the Smart Align software. Furthermore, Ingrid Hallsteinsen in acknowledged for supplying the perovskite heterostructure sample materials. The Research Council of Norway (RCN) is acknowledged for the support to the Norwegian Micro- and Nano-Fabrication Facility, NorFab (197413/V30). Partial funding for this work was obtained from the Norwegian PhD Network on Nanotechnology for Microsystems, which is sponsored by the RCN, Division for Science, under contract no. 190086/S10. Funding for TEM time is partly funded by the project NORTEM (Grant 197405) within the programme INFRASTRUCTURE of the RCN. NORTEM was co-funded by the RCN and the project partners NTNU, UiO and SINTEF. Ida Hjorth is acknowledged for fruitful discussions and proof-reading.

References

[1] O.L. Krivanek, N. Dellby, and A.R. Lupini. Towards sub-Å electron beams. *Ultramicroscopy*, 78(1–4):1 – 11, 1999.

[2] Uwe Falke, Andrew Bleloch, Meiken Falke, and Steffen Teichert. Atomic structure of a (2x1) reconstructed $NiSi_2$/Si(001) interface. *Phys. Rev. Lett.*, 92:116103, Mar 2004.

[3] Thomas Lunkenbein, Frank Girgsdies, Anna Wernbacher, Johannes Noack, Gudrun Auffermann, Akira Yasuhara, Achim Klein-Hoffmann, Wataru Ueda, Maik Eichelbaum, Annette Trunschke, Robert Schlögl, and Marc G. Willinger. Direct imaging of octahedral distortion in a complex molybdenum vanadium mixed oxide. *Angewandte Chemie International Edition*, 54(23):6828–6831, 2015.

[4] Ian MacLaren, Rafael Villaurrutia, Bernhard Schaffer, Lothar Houben, and Aimé Peláiz-Barranco. Atomic-scale imaging and quantification of electrical polarisation in incommensurate antiferroelectric lanthanum-doped lead zirconate titanate. *Advanced Functional Materials*, 22(2):261–266, 2012.

[5] M. Nord, P. E. Vullum, M. Moreau, J. E. Boschker, S. M. Selbach, R. Holmestad, and T. Tybell. Structural phases driven by oxygen vacancies at the $La_{0.7}Sr_{0.3}MnO_3/SrTiO_3$ hetero-interface. *Applied Physics Letters*, 106(4):041604, January 2015.

[6] J. Gazquez, Shameek Bose, M. Sharma, M. A. Torija, S. J. Pennycook, C. Leighton, and M. Varela. Lattice mismatch accommodation via oxygen vacancy ordering in epitaxial $La_{0.5}Sr_{0.5}CoO_{3-\delta}$ thin films. *APL Materials*, 1(1):012105, 2013.

[7] Ian MacLaren, Li Qiu Wang, Bernhard Schaffer, Quentin M. Ramasse, Alan J. Craven, Sverre M. Selbach, Nicola A. Spaldin, Shu Miao, Kambiz Kalantari, and Ian M. Reaney. Novel nanorod precipitate formation in neodymium and titanium codoped bismuth ferrite. *Advanced Functional Materials*, 23(6):683–689, 2013.

[8] A. Y. Borisevich, H. J. Chang, M. Huijben, M. P. Oxley, S. Okamoto, M. K. Niranjan, J. D. Burton, E. Y. Tsymbal, Y. H. Chu, P. Yu, R. Ramesh, S. V. Kalinin, and S. J. Pennycook. Suppression of Octahedral Tilts and Associated Changes in Electronic Properties at Epitaxial Oxide Heterostructure Interfaces. *Physical Review Letters*, 105(8), August 2010.

[9] S.J. Pennycook and D.E. Jesson. High-resolution z-contrast imaging of crystals. *Ultramicroscopy*, 37(1):14 – 38, 1991.

[10] James M. LeBeau, Scott D. Findlay, Leslie J. Allen, and Susanne Stemmer. Standardless atom counting in scanning transmission electron microscopy. *Nano Letters*, 10(11):4405–4408, 2010.

[11] David A. Muller, Naoyuki Nakagawa, Akira Ohtomo, John L. Grazul, and Harold Y. Hwang. Atomic-scale imaging of nanoengineered oxygen vacancy profiles in $SrTiO_3$. *Nature*, 430(7000), August 2004.

[12] Sean Hillyard and John Silcox. Detector geometry, thermal diffuse scattering and strain effects in ADF STEM imaging. *Ultramicroscopy*, 58(1):6 – 17, 1995.

[13] Albina Y. Borisevich, Oleg S. Ovchinnikov, Hye Jung Chang, Mark P. Oxley, Pu Yu, Jan Seidel, Eugine A. Eliseev, Anna N. Morozovska, Ramamoorthy Ramesh, Stephen J. Pennycook, and Sergei V. Kalinin. Mapping octahedral tilts and polarization across a domain wall in $BiFeO_3$ from

Z-contrast scanning transmission electron microscopy image atomic column shape analysis. *ACS Nano*, 4(10):6071–6079, 2010.

[14] C. L. Jia. Atomic-Resolution Imaging of Oxygen in Perovskite Ceramics. *Science*, 299(5608):870–873, February 2003.

[15] James M. LeBeau, Adrian J. D'Alfonso, Scott D. Findlay, Susanne Stemmer, and Leslie J. Allen. Quantitative comparisons of contrast in experimental and simulated bright-field scanning transmission electron microscopy images. *Phys. Rev. B*, 80:174106, Nov 2009.

[16] Ian MacLaren, LiQiu Wang, Owen Morris, Alan J. Craven, Robert L. Stamps, Bernhard Schaffer, Quentin M. Ramasse, Shu Miao, Kambiz Kalantari, Iasmi Sterianou, and Ian M. Reaney. Local stabilisation of polar order at charged antiphase boundaries in antiferroelectric $(Bi_{0.85}Nd_{0.15})(Ti_{0.1}Fe_{0.9})O_3$. *APL Mater.*, 1(2), 2013.

[17] S.D. Findlay, N. Shibata, H. Sawada, E. Okunishi, Y. Kondo, and Y. Ikuhara. Dynamics of annular bright field imaging in scanning transmission electron microscopy. *Ultramicroscopy*, 110(7):903 – 923, 2010.

[18] Ryotaro Aso, Daisuke Kan, Yuichi Shimakawa, and Hiroki Kurata. Octahedral tilt propagation controlled by a-site cation size at perovskite oxide heterointerfaces. *Crystal Growth & Design*, 14(5):2128–2132, 2014.

[19] Qian He, Ryo Ishikawa, Andrew R. Lupini, Liang Qiao, Eun J. Moon, Oleg Ovchinnikov, Steven J. May, Michael D. Biegalski, and Albina Y. Borisevich. Towards 3d mapping of BO_6 octahedron rotations at perovskite heterointerfaces, unit cell by unit cell. *ACS Nano*, page 150729113150000, July 2015.

[20] A. M. Glazer. The classification of tilted octahedra in perovskites. *Acta Crystallographica Section B*, 28(11):3384–3392, Nov 1972.

[21] M. J. Hÿtch, E. Snoeck, and R. Kilaas. Quantitative measurement of displacement and strain fields from HREM micrographs. *Ultramicroscopy*, 74(3):131–146, 1998.

[22] Martin J Hÿtch, Jean-Luc Putaux, and Jean-Michel Pénisson. Measurement of the displacement field of dislocations to 0.03 Å by electron microscopy. *Nature*, 423(6937):270–273, 2003.

[23] Yuanyuan Zhu, Colin Ophus, Jim Ciston, and Haiyan Wang. Interface lattice displacement measurement to 1pm by geometric phase analysis on aberration-corrected HAADF STEM images. *Acta Materialia*, 61(15):5646–5663, September 2013.

[24] Stephen M. Anthony and Steve Granick. Image Analysis with Rapid and Accurate Two-Dimensional Gaussian Fitting. *Langmuir*, 25(14):8152–8160, July 2009.

[25] Ranger | Lewys Jones's Research. `http://lewysjones.com/software/ranger/`.

[26] HREM qHAADF. `https://www.hremresearch.com/Eng/PressRelease/PressRelease_qHAADF2.htm`.

[27] imtools. `http://www.er-c.org/centre/software/imtools.htm`.

[28] A. De Backer, K.H.W. van den Bos, W. Van den Broek, J. Sijbers, and S. Van Aert. Statstem: An efficient approach for accurate and precise model-based quantification of atomic resolution electron microscopy images. *Ultramicroscopy*, 171:104 – 116, 2016.

[29] Yi Wang, Ute Salzberger, Wilfried Sigle, Y. Eren Suyolcu, and Peter A. van Aken. Oxygen octahedra picker: A software tool to extract quantitative information from stem images. *Ultramicroscopy*, 168:46 – 52, 2016.

[30] Jian-Min Zuo, Amish B. Shah, Honggyu Kim, Yifei Meng, Wenpei Gao, and Jean-Luc Rouviére. Lattice and strain analysis of atomic resolution z-contrast images based on template matching. *Ultramicroscopy*, 136:50 – 60, 2014.

[31] L. Houben, A. Thust, and K. Urban. Atomic-precision determination of the reconstruction of a tilt boundary in by aberration corrected hrtem. *Ultramicroscopy*, 106(3):200 – 214, 2006.

[32] Nouamane Laanait, Maxim Ziatdinov, Qian He, and Albina Borisevich. Identifying local structural states in atomic imaging by computer vision. *Advanced Structural and Chemical Imaging*, 2(1):14, 2016.

[33] Nick Barnes. Publish your computer code: it is good enough. *Nature*, 467(7317):753–753, 2010.

[34] I. Hallsteinsen, J. E. Boschker, M. Nord, S. Lee, M. Rzchowski, P. E. Vullum, J. K. Grepstad, R. Holmestad, C. B. Eom, and T. Tybell. Surface stability of epitaxial $La_{0.7}Sr_{0.3}MnO_3$ thin films on (111)-oriented $SrTiO_3$. *Journal of Applied Physics*, 113(18), 2013.

[35] Ingrid Hallsteinsen, Magnus Nord, Torstein Bolstad, Per-Erik Vullum, Jos E. Boschker, Paulo Longo, Ryota Takahashi, Randi Holmestad, Mikk Lippmaa, and Thomas Tybell. Effect of polar (111)-oriented $srtio_3$ on initial perovskite growth. *Crystal Growth & Design*, 16(4):2357–2362, 2016.

[36] Magnus Nord, Per Erik Vullum, Ingrid Hallsteinsen, Thomas Tybell, and Randi Holmestad. Assessing electron beam sensitivity for $SrTiO_3$ and

$La_{0.7}Sr_{0.3}MnO_3$ using electron energy loss spectroscopy. *Ultramicroscopy*, 169:98 – 106, 2016.

[37] Stijn Lichtert and Jo Verbeeck. Statistical consequences of applying a pca noise filter on eels spectrum images. *Ultramicroscopy*, 125:35 – 42, 2013.

[38] Francisco de la Peña, Pierre Burdet, Vidar Tonaas Fauske, Tomas Ostasevicius, Mike Sarahan, Magnus Nord, Josh Taillon, Duncan Johnstone, Alberto Eljarrat, Stefano Mazzucco, Jan Caron, Eric Prestat, Gaël Donval, Luiz Fernando Zagonel, Michael Walls, and iygr. hyperspy: HyperSpy 0.8.4. 2016.

[39] David A. Muller, Earl J. Kirkland, Malcolm G. Thomas, John L. Grazul, Lena Fitting, and Matthew Weyland. Room design for high-performance electron microscopy. *Ultramicroscopy*, 106(11–12):1033 – 1040, 2006.

[40] Benjamin Berkels, Peter Binev, Douglas A. Blom, Wolfgang Dahmen, Robert C. Sharpley, and Thomas Vogt. Optimized imaging using non-rigid registration. *Ultramicroscopy*, 138:46 – 56, 2014.

[41] Lewys Jones, Hao Yang, Timothy J. Pennycook, Matthew S. J. Marshall, Sandra Van Aert, Nigel D. Browning, Martin R. Castell, and Peter D. Nellist. Smart Align—a new tool for robust non-rigid registration of scanning microscope data. *Advanced Structural and Chemical Imaging*, 1(1), December 2015.

[42] Dan Zhou, Knut Müller-Caspary, Wilfried Sigle, Florian F. Krause, Andreas Rosenauer, and Peter A. van Aken. Sample tilt effects on atom column position determination in abf–stem imaging. *Ultramicroscopy*, 160:110 – 117, 2016.

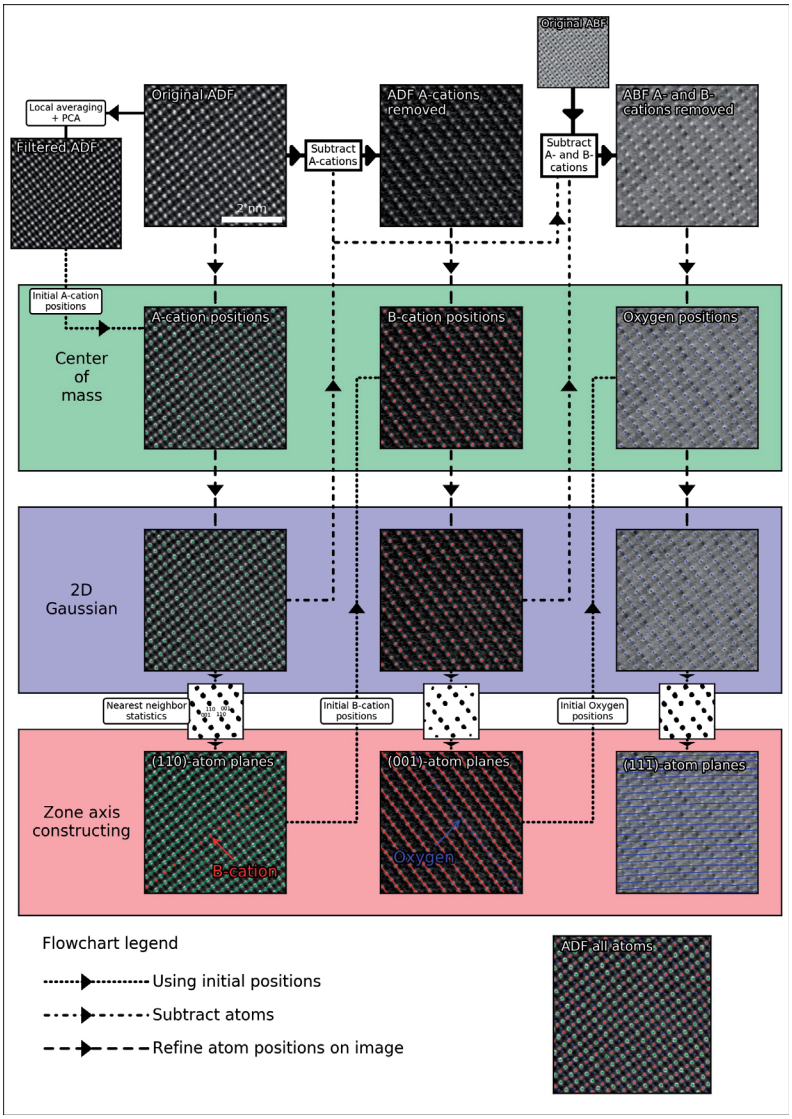

Figure 1: Processing steps for locating and fitting 2-D Gaussians to every atomic column in a perovskite oxide using STEM-ADF and STEM-ABF data acquired with the electron beam parallel to the $[1\bar{1}0]$ direction.

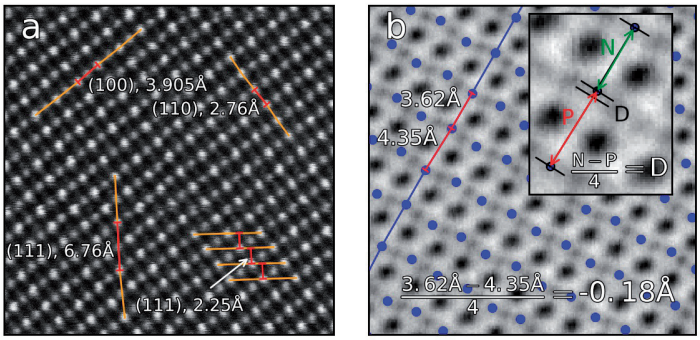

Figure 2: Quantifying distances between atomic columns. (a) Distances between atoms in different directions, here shown on A-cation atom columns. For the [001] and [110] directions, simply taking the difference between each following atom in an orthogonal atom plane gives the interplanary spacing. For the [111] direction, going to the next atom in an $(11\bar{2})$ atom plane jumps 3 (111) atom planes. Instead, the interplanar distance is found by finding the shortest distance between an atom and the line spanned by the neighboring (111)-atom plane. (b) Calculating displacement (D) from a centrosymmetric position between atomic columns, here shown on oxygen columns. The inset shows how the distance difference is calculated for oxygen atoms in the [001]-direction for a LFO film. The distance to the next (N) and previous (P) atom is calculated, as shown with the green and red double headed arrows

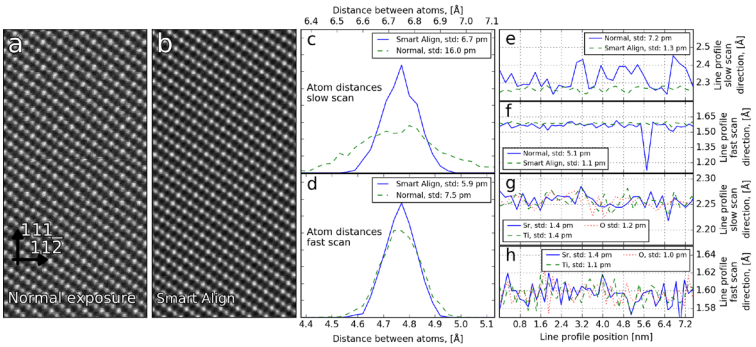

Figure 3: Quantifying the uncertainty in measurements of atomic spacings as a consequence of image acquisition methodology: (a) Conventional HAADF-STEM image recorded at 38.5 µs per pixel and (b) Image constructed by rigid and non-rigid registration of 20 HAADF-STEM images recorded at 2 µs per pixel; (c) Distribution of distances between Sr atoms along the slow scan direction ([111]), comparing the normal exposure from (a) and the Smart Align dataset in (b). (d) same as (c), but for the fast scan direction ([11$\bar{2}$]). (e) (111) plane spacings of Sr atoms along the slow scan direction, showing an improvement in the uncertainty from 7.2 to 1.3 pm standard deviation when processing the image using Smart Align; (f) (11$\bar{2}$) plane spacings of Sr atoms along the fast scan direction, showing an improvement in the uncertainty from 5.1 to 1.1 pm. (g) and (h): similar to (d) and (e), but comparing uncertainty for the different sublattices from a different dataset processed using Smart Align. Both the slow scan direction (g) and the fast scan direction (h) showing a uncertainty of 1.0 to 1.4 pm for all three sublattices.

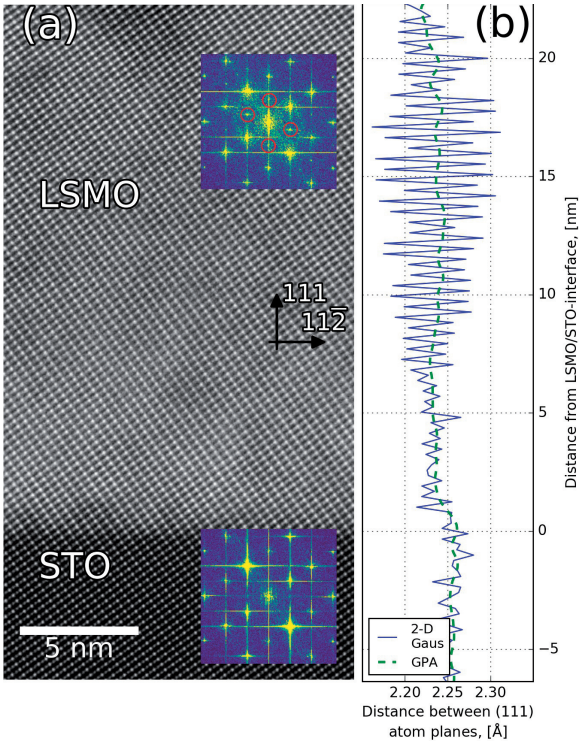

Figure 4: Comparison of geometrical phase analysis (GPA) and the method outlined in this work for determining the out-of-plane lattice parameter. (a) STEM-HAADF image of a LSMO film grown on STO-(111). Top inset is an FFT of the LSMO region, showing a clear superstructure compared to the STO substrate FFT in the lower inset. (b) Average interplanar distance for the A-cation (111) atom planes as a function of distance from the LSMO/STO interface. The blue solid line shows the result from the method outlined in this paper, and the dashed green line from GPA.

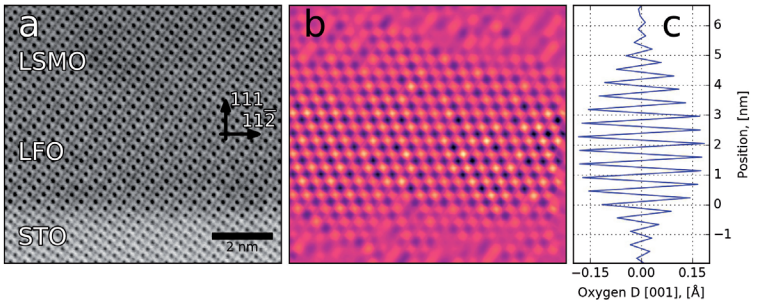

Figure 5: Finding the displacement, D, of oxygen atomic columns in the [001]-direction, compared to centrosymmetric positions in a cubic structure. (a) STEM-ABF image of LSMO/LFO/STO-(111) heterostructure. (b) Map of the deviation in oxygen position from primitive perovskite calculated using the method outlined in section 2.2. (c) Average value of the displacement for each plane as a function of distance from the LFO/STO-interface.

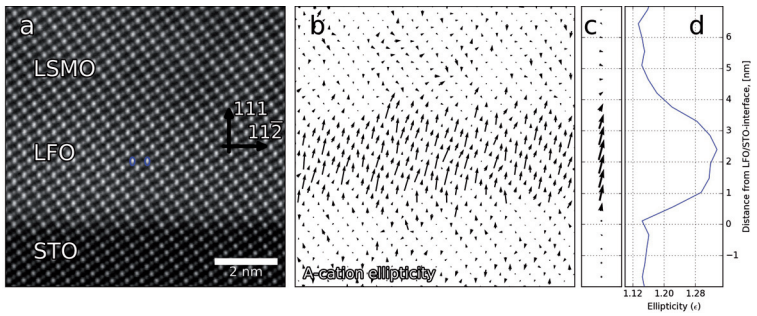

Figure 6: Mapping ellipticity (ϵ) and rotation (ρ) of A-cation atomic columns in the LSMO/LFO/STO-(111) heterostructure. (a) STEM-ADF image of the heterostructure. There is a clear elongation of the A-cation atomic columns in the LFO layer (blue ellipses), compared to the STO and LSMO. (b) ϵ and ρ of the individual A-cations plotted as arrows. (c) Same as in (b), but summed as a function of distance from the LFO/STO-interface. (d) ϵ as a function of distance from the LFO/STO interface.

Paper V

Concurrent magnetic and structural reconstructions at the interface of (111)-oriented $La_{0.7}Sr_{0.3}MnO_3/LaFeO_3$

I. Hallsteinsen, M. Moreau, A. Grutter, M. Nord, P. E. Vullum, D. A. Gilbert, T. Bolstad, J. K. Grepstad, R. Holmestad, S. M. Selbach, A. T. N'Diaye, B. J. Kirby, E. Arenholz, and T. Tybell

Physical Review B, 94, 201115(R) (2016)

Supplementary material for this paper is included in part IV, the Appendix.

RAPID COMMUNICATIONS

PHYSICAL REVIEW B **94**, 201115(R) (2016)

Concurrent magnetic and structural reconstructions at the interface of (111)-oriented $La_{0.7}Sr_{0.3}MnO_3/LaFeO_3$

I. Hallsteinsen,[1,2] M. Moreau,[1] A. Grutter,[3] M. Nord,[4] P.-E. Vullum,[4,5] D. A. Gilbert,[3] T. Bolstad,[1] J. K. Grepstad,[1] R. Holmestad,[4] S. M. Selbach,[6] A. T. N'Diaye,[2] B. J. Kirby,[3] E. Arenholz,[2] and T. Tybell[1,*]

[1]*Department of Electronics and Telecommunications, NTNU—Norwegian University of Science and Technology, Trondheim 7491, Norway*
[2]*Advanced Light Source, Lawrence Berkeley National Laboratory, Berkeley, California 94720, USA*
[3]*Center for Neutron Research, National Institute of Standards and Technology, Gaithersburg, Maryland 20899, USA*
[4]*Department of Physics, NTNU—Norwegian University of Science and Technology, Trondheim 7491, Norway*
[5]*SINTEF Materials and Chemistry, Trondheim 7491, Norway*
[6]*Department of Material Science and Engineering, NTNU—Norwegian University of Science and Technology, Trondheim 7491, Norway*

(Received 6 July 2016; published 21 November 2016)

We observe an induced switchable magnetic moment of $1.6 \pm 0.40\,\mu_B$/Fe for the nominally antiferromagnetic $LaFeO_3$ extending two to four interface layers into the non–charge transfer system $La_{0.7}Sr_{0.3}MnO_3/LaFeO_3/SrTiO_3(111)$. Simultaneously a mismatch of oxygen octahedra rotations at the interface implies an atomic reconstruction of reduced symmetry at the interface, reaching two to five layers into $LaFeO_3$. Density functional theory of a structure with atomic reconstruction and different correlation strength shows a ferrimagnetic state with a net Fe moment at the interface. Together these results suggest that engineered oxygen octahedra rotations, affecting the local symmetry, affect electron correlations and can be used to promote magnetic properties.

DOI: 10.1103/PhysRevB.94.201115

Interface engineering of oxides is used to promote novel properties such as metallic conduction between two insulators [1,2], and ferromagnetism (FM) between non-FM materials [3,4]. Tailoring magnetic interfaces in a controlled manner is considered a cornerstone of further development of spintronic devices [5]. Until now much attention has been on modified magnetic states due to charge transfer; for example, in superlattices of $CaRuO_3/CaMnO_3$ and $LaNiO_3/LaMnO_3$, charge transfer results in double exchange between Mn^{3+}/Mn^{4+} and induced FM at the interface [6–8]. In $(Y, Ca)Ba_2Cu_3O_7/La_{0.67}Ca_{0.33}MnO_3$ depletion of charge from the Cu-O layers leads to a reconstruction into a FM orbital-ordered system [4]. However, induced FM at Fe has also been observed in nominally nonferromagnetic materials adjacent to $La_{0.7}Sr_{0.3}MnO_3$ (LSMO) [9,10], even though the d^5 electronic state of Fe^{3+} prohibits charge transfer. Atomic reconstructions at interfaces, resulting in novel tilt patterns of the oxygen octahedra, have previously been associated with the emergence of new ferroelectric states [11,12], while the coupling between atomic reconstructions and magnetism is relatively unexplored, despite the importance to spintronic device applications [13,14]. The interface between antiferromagnetic (AF) $LaFeO_3$ (LFO) and the half-metal FM LSMO holds promise from an engineering perspective, as charge transfer to the d^5 Fe^{3+} is prohibited, while atomic reconstructions due to a mismatch in tilt patterns is expected. The tilt patterns of their oxygen octahedra are not directly compatible, with LFO (S.G. 62, *Pbnm*) and LSMO (S.G. 167, $R\bar{3}c$) having $a^-a^-c^+$ and $a^-a^-a^-$ rotations (Glazer notation), respectively [15]. This mismatch must be accommodated at the interface, likely through atomic reconstructions. In this Rapid Communication, we address how the mismatch in octahedral rotations is accommodated through structural relaxations at the interface leading to the emergence of FM in LFO, in (111)-oriented LSMO/LFO/$SrTiO_3$ (STO) heterostructures. As all the rotation directions of the oxygen octhadera have both in-plane and out-of-plane components at a (111)-oriented interface it is expected that the change from $a^-a^-c^+$ to $a^-a^-a^-$ rotation would have a larger impact on the structure than for a (001)-oriented interface. Indeed we show large rotational changes at the LSMO/LFO interface, no substantial charge transfer, and an induced switchable moment at the Fe atoms. The length scale of structural as well as magnetic reconstructions extends three to five layers into LFO, and the induced magnetic moment is an order of magnitude larger than previously reported for LSMO/LFO(001) [9].

Epitaxial heterostructures of LSMO/LFO/STO(111) were deposited by pulsed laser deposition (PLD) with LSMO and LFO thicknesses of 16 d_{111} monolayers (3.6 nm) each, 7.2 nm in total. Deposition parameters are described in Refs. [16–18], resulting in fully strained (111)-oriented films with atomically smooth step-and-terrace surfaces (see the Supplemental Material [19]). The atomic structure was analyzed by scanning transmission electron microscopy (STEM) using high-angle annular dark-field (HAADF), annular bright field (ABF), and electron energy loss spectroscopy (EELS). Scanning distortions were reduced by using nonrigid registration [20] and EELS processing was done using HYPERSPY [19,21]. Density functional theory (DFT) calculations were done with the Vienna *ab initio* simulation package (VASP) using the PBE-sol functional and a plane-wave cutoff energy of 550 eV [22–24]. The projected augmented wave - Perdew Burke Ernzerhof (PAW-PBE) potentials supplied with VASP for La, Sr, Mn, Fe, and O with electron configurations $4s^24p^65d^16s^2$, $4s^24p^65s^2$, $3d^54s^2$, $3d^64s^2$, and $2s^22p^4$ respectively were used and different configurations of La and Sr in LSMO were tested [25]. Hubbard U of 10 and 3 eV were applied to the La 4f and Mn 3d orbitals, respectively [26]. Calculations of LFO were done with a 60-atom $\sqrt{2} \times \sqrt{6} \times 2\sqrt{3}$

*Corresponding author: thomas.tybell@ntnu.no

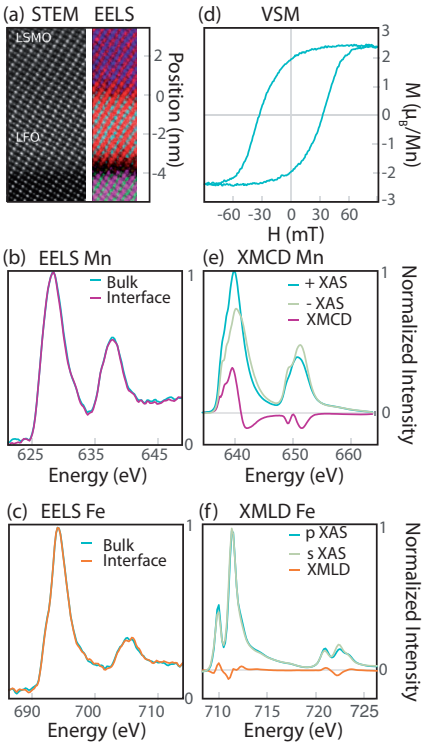

FIG. 1. (a) STEM HAADF image (left) and EELS map (right) colored by element, i.e., La (red), Mn (purple), Fe (turquoise), Sr (pink), and Ti (green). (b,c) show EELS spectra of $L_{2,3}$ edge of Mn (Fe) at the interface [purple (orange)] and in the center of the layer (turquoise). (d) Hysteresis curve of the bilayer recorded at 50 K. (e,f) XA of different circular (linear) polarization and XMCD (XMLD) spectra of Mn (Fe) L edge.

supercell, while the interface was modeled with 12/12 (LFO/LSMO) 240-atom $\sqrt{2} \times \sqrt{6} \times 8\sqrt{3}$ supercells, with corresponding gamma-centered k-point mesh of $4 \times 3 \times 2$ and $4 \times 3 \times 1$, respectively. The in-plane lattice parameters were locked to the calculated equilibrium value of STO, while the out-of-plane lattice parameter and atomic positions were relaxed until the forces on the ions were below 0.01 eV/Å.

To investigate charge transfer across the interface, Bader charges [27] were calculated for LSMO/LFO supercells. For Fe, a small change in Bader charge, 3.03+ from 3+ in bulk, is observed in the unit cell closest to the interface. A small change in Fe valence is expected for Fe-terminated LFO, since this layer effectively corresponds to a mixed LSFO layer, while for the opposite termination the calculations reveal no change in Fe valence. For Mn the Bader charge is increased to 3.375+ (from 3.3+) at the interface, indicating an increased amount of Mn^{4+}. Experimental STEM HAADF reveal that the heterostructure is epitaxial, fully strained, and of high crystalline quality and EELS maps reveal a sharp LSMO/LFO interface with no substantial intermixing of cations [Fig. 1(a)], unlike the LFO/STO interface which is intermixed [18,19]. A comparison of EELS spectra at the bulk and at the interface reveals no change in the Mn and Fe valence state, indicating no charge transfer within the measurement sensitivity [Figs. 1(b) and 1(c)].

The magnetic ground state of the thin films was probed using a vibrating sample magnetometer after a 2 T field cooling to 50 K from room temperature; in Fig. 1(d) a hysteresis at 50 K is shown. The saturation magnetization is 2.4 μ_B/Mn, assuming Mn as the only contribution to the magnetic signal and the coercive field is 37.5 mT. The Curie temperature, T_c, was 275 K [19]. X-ray magnetic circular dichroism (XMCD) and x-ray magnetic linear dichroism (XMLD) spectroscopy were measured at beamline 4.0.2 and 6.3.1 at the Advanced Light Source (ALS) and I1011 at MaxLab II. The spectra shown were measured in total-electron-yield mode by monitoring the sample drain current, with the x rays incident at 30° to the sample surface. Using an eight-pole electromagnet, XMCD was measured with an applied field of ±0.3 T parallel to the x-ray beam. For XMLD, s and p polarization of the beam was used. Figures 1(e) and 1(f) depict the absorption spectra for the Mn and Fe L edge, respectively, with spectral shapes in agreement with reported spectra for single-layer films with $Mn^{3.3+}$ and Fe^{3+} valence state [28,29]. XMCD/XMLD was adopted to probe the element-specific FM/AF; Mn XMCD spectra confirm FM ordering (30% XMCD) and Fe XMLD spectra indicate AF ordering with 5% XMLD (similar to single-layer LFO). LFO in bulk is a G-type AF, with fully spin polarized (111) planes. The coercive field of the bilayer is increased compared to single layers of LSMO [30]; however, no exchange bias was observed. The dichroism of Fe indicates a canted out-of-plane AF axis, in agreement with (111) $(La,Sr)FeO_3$, which also exhibited no exchange bias [31].

Having established the magnetic states for the individual constituents of the heterostructure we turn to structural effects at the interface, focusing on the LFO. Figure 2(a) shows schematics of the oxygen octahedral rotations for STO ($a^0a^0a^0$), LFO ($a^-a^-c^+$), and LSMO ($a^-a^-a^-$). At the LSMO/LFO interface half of the octahedra match (tilt the same way), while the other half do not (tilt the opposite way). STEM HAADF and ABF imaging along the $[1\bar{1}0]$-zone axis were used to probe the atomic positions [Figs. 2(b) and 2(d)]. In Fig. 2(c) the eccentricity (deviation from a circle) of the A-cation columns are plotted as a function of position with respect to the LSMO/LFO interface. In LFO a large eccentricity is expected due to the distortion of the unit cell. As expected, the eccentricity peaks in the center of the LFO layer, and is reduced near both interfaces. However, the change is not abrupt, and two to three layers of LFO close to the LSMO interface have a reduced eccentricity compared to the center of the LFO. Another measure of deviation from the cubic structure is the displacement of the oxygen columns along the [100] direction, where LFO should have a displacement of 35 pm. In Fig. 2(e) it is clear that the amplitude of the displacements decreases throughout both interfaces, beginning roughly at the second layer of LFO, hence these layers have a reduced displacement. Combining the oxygen displacement and A-cation eccentricity data, the analysis suggests that two to three interface layers of LFO have a reduced distortion compared to bulk. DFT simulations of the octahedral rotation angle along the c axis (γ) across the LSMO/LFO interface

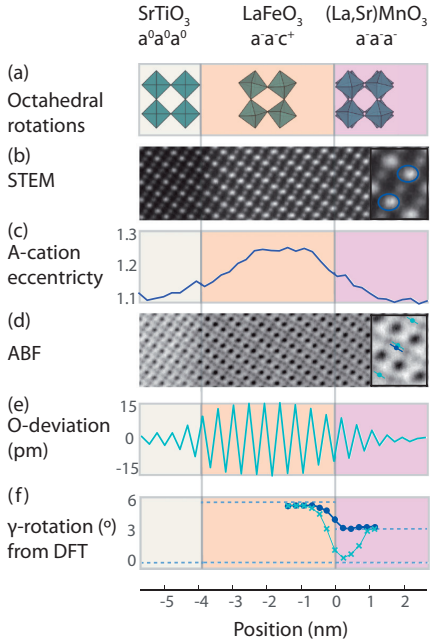

FIG. 2. (a) Schematic of the octahedral rotations in STO ($a^0a^0a^0$), LFO ($a^-a^-c^+$), and LSMO ($a^-a^-a^-$) shown from the [001] direction [33]. (b) STEM-HAADF image. Inset shows the enlarged view of the elliptical form of the La columns in LFO. (c) Plot of the *A*-cation eccentricity (d) STEM-ABF image. Inset shows an enlarged view of oxygen positions in the layer (turquoise) and the deviation from a cubic structure (blue). (e) Plot of the oxygen column displacement along [100], integrated for monolayers in the [111] direction. (f) Plot of the calculated γ rotation for matched (dark blue) and mismatched (turquoise) octahedra. All plots are shown as a depth profile through the bilayer, and are matched to the TEM images as shown by the gray lines and colored boxes.

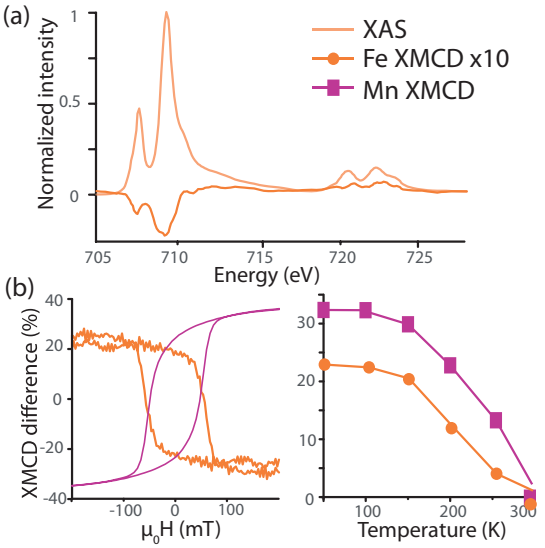

FIG. 3. (a) XA and XMCD spectra at the Fe *L* edge. (b) Field (left) and temperature (right) dependence of Fe *L*3 XMCD (orange) and Mn *L*3 XMCD (purple).

are presented in Fig. 2(f), where the matching octahedra (dark blue) and the nonmatching octahedra (light blue) evolve differently. While the rotations of the matched octahedra relax to the bulk value for both materials, the rotation angle of the mismatched octahedra drops toward zero. The tilt pattern at the interface is hence close to the $a^-a^-c^0$ tilt pattern for half the octahedra. The reduced rotation angle prevails two to four layers into the LFO, in accordance with the experimental data.

To investigate if the observed structural changes at the interface have influence on the magnetic properties, XMCD spectroscopy probing ferromagnetic order was performed at the Fe *L* edge [Fig. 3(a)]. We observe a circular dichroism signal of approximately 2% of the Fe L3 normalized absorption peak (XA) signal at 50 K. Measurements were done with alternating polarization of the x rays under a static field and in remanence, as well as with alternating field with a static polarization resulting in the same magnitude and shape of the dichroism signal. Monitoring the field dependence of the Fe and Mn *L*3 XMCD in hysteresis loops [Fig. 3(c)] reveals that Mn and Fe are antiparallel and with equal coercive fields of approximately 70 mT at 50 K. This is in agreement with Bruno *et al.* [9], who demonstrated an induced FM moment in LFO with an antiparallel coupling to LSMO for LSMO/LFO(001). In Fig. 3(d) we have plotted the temperature dependence of the Mn and Fe *L*3 XMCD. The Fe XMCD signal follows that of Mn, with a comparable T_c, although the Néel temperature of LFO is much higher (740 K). The similar coercive field and Curie temperature observed for both Mn and Fe strongly suggest that the FM moment of Fe is stabilized by a coupling with the LSMO layer. Although FM systems also have a XMLD response the Fe-XMLD signal is larger than the XMCD signal for Fe, implying a predominantly AF LFO layer.

In order to investigate the depth profile of the magnetic structure we used polarized neutron reflectivity (PNR) performed using the PBR beamline at NIST Center for Neutron Research. Measurements were conducted at 50 K after field cooling in 700 mT, using an in-plane measurement field of 700 mT. The spin of the incident neutrons was polarized parallel or antiparallel to the in-plane magnetic field *H*, and the specular reflectivity was measured as a function of wave-vector transfer along the surface normal Q_z. The model-fitted non-spin-flip reflectivities are depicted in Fig. 4(a). In this scattering geometry the non-spin-flip reflectivity is a function of the nuclear and magnetic scattering length density (SLD) depth profiles, where the magnetic SLD is directly proportional to the magnetization component parallel to *H*, and not sensitive to AF ordering. We find a splitting of the two channels, indicating sensitivity to the sample magnetization. The PNR data were modeled using the REFL1D software package [32], and the resulting depth profile is shown in Fig. 4(b). It is clear that LSMO is FM with a positive magnetic SLD throughout the film, while at the LFO interface the magnetic SLD is negative for several layers, before relaxing to 0. Hence,

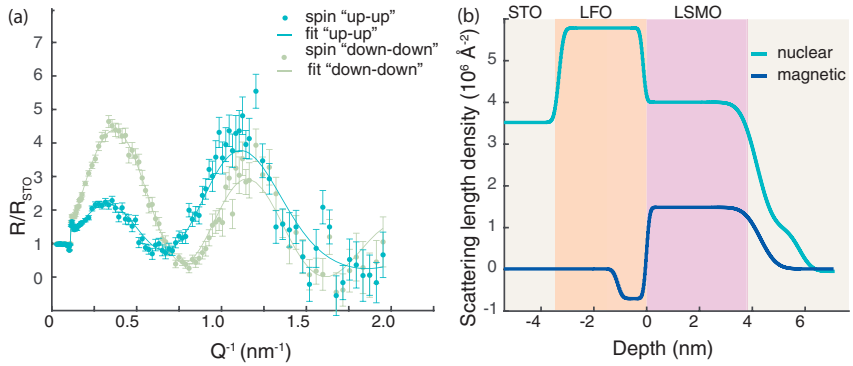

FIG. 4. (a) Neutron reflectivity (crosses) and fits (line) measured in the non-spin-flip geometry, with neutrons polarized with spin up (blue) and spin down (green) with respect to the external field. (b) Magnetic and nuclear depth profile derived from the neutron scattering data.

the LFO has clearly a remanent moment at the interface antiparallel to the LSMO, in agreement with the XMCD measurements. For comparison, we also fit the PNR to a model with zero net magnetization in the LFO layer, which resulted in a significantly poorer fit (see [19]). The fitted PNR model with a 95% confidence interval shows that the induced moment reaches between 0.64 and 1.19 nm (three to five d_{111} monolayers) into LFO. The FM moment of LSMO was found to be $3.1 \pm 0.06\,\mu_B$/Mn, while the LFO moment was found to be $1.6 \pm 0.40\,\mu_B$/Fe. However, the value is smaller than the nominal AF moment of $4.5\,\mu_B$/Fe, suggesting a canted AF or ferrimagnetic state at the interface.

The length scales of the induced FM moment and the structural reconstruction are both around two to five layers into LFO. *G*-type AF order is found to be 313 meV/f.u. lower in energy than FM order from DFT calculations on pure LFO. Although this confirms that *G*-type AF is very stable in bulk LFO, a different local symmetry is enforced at the (111)-LFO/LSMO interface, possibly affecting the electron correlations. By taking the Hubbard U enforced on Fe as a measure of the correlation strength, we compare the energy difference between the FM and AF states for different rotation patterns [Fig. 5(a)]. Interestingly, we find that as U_{Fe} approaches zero a FM state is stabilized. This ferromagnetic state is stable for the $a^-a^-a^0$ rotations resembling the tilt pattern observed at the interface [Fig 2(e)], but not for the bulk $a^-a^-c^+$ rotations. For a 12/12 LFO/LSMO superlattice, including the effects of the interface and symmetry mismatch, the lowest energy is still found for the bulk *G*-type AF. FM-ordered Fe layers at the interface are metastable with an energy cost of ∼45 meV/Fe for each FM layer, and the lowest value for parallel Mn and Fe moments. With a nominal U_{Mn} of 3 eV, Bader charge analysis revealed that the Mn closest to the LFO has a larger fraction of Mn^{4+} compared to the rest of the cell, inconsistent with the EELS measurements. To impose a 3.3+ Mn valence increased values of Hubbard U at the interface ($U_{Mn,I}$) are investigated, which result in an AF ground state with a FM moment at the interface. As seen in Fig. 5(b), the net FM moment for Fe increases with increasing $U_{Mn,I}$. For pure LFO a net FM moment was found for decreased U_{Fe}; in Fig. 5(b) we plot the effect of lowering U_{Fe} for the two Fe layers closest to the interface ($U_{Fe,I}$), keeping U_{Mn} constant at 3 eV. The result is a switchable moment which is increased as $U_{Fe,I}$ is lowered. In the right panel of Fig. 5(b) these two effects are combined; with the Fe moments as a function of $U_{Fe,I}$ with $U_{Mn,I} = 5$ eV. As we reduce the $U_{Fe,I}$ and increase $U_{Mn,I}$ we reduce the degree of electron localization of the Fe 3*d* electrons and obtain a net FM Fe moment. Though the AF structure is not affected by the direction of the Mn, the FM Fe moment is switchable and antiparallel to the Mn moment,

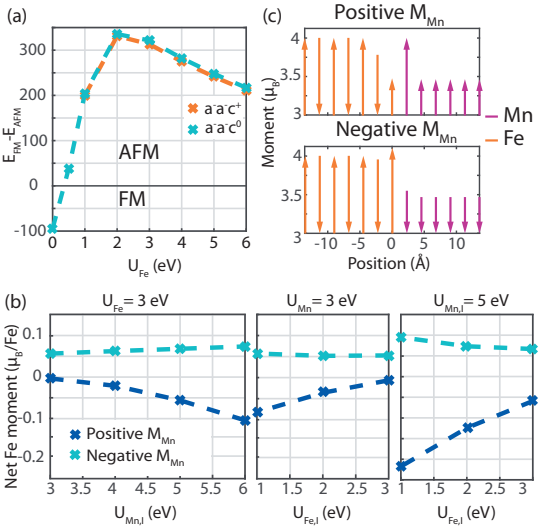

FIG. 5. (a) Energy difference between FM and AF order of LFO as a function of Hubbard U for different rotation patterns. A positive value means that AF ordering is preferred. Note that the $a^-a^-c^+$ rotation is not stable for $U < 1$ eV. (b) Net Fe moment as a function of $U_{Mn,I}$ and $U_{Fe,I}$ in the LSMO/LFO supercell. The first panel shows the dependence on $U_{Mn,I}$ with U_{Fe} constant 3 eV, the second panel $U_{Fe,I}$ with $U_{Mn} = 3$ eV, and the third pane $U_{Fe,I}$ with $U_{Mn,I} = 5$ eV. (c) Atomic magnetic moments as a function of distance from the LSMO/LFO(111) interface with $U_{Mn,I} = 5$ eV and $U_{Fe,I} = 1$ eV.

in agreement with experimental results. The DFT calculations reveal a ferrimagnetic ordering of LFO adjacent to the interface [Fig. 5(c)], where the Fe moment decreases with each layer as we draw nearer to the interface. With $U_{\mathrm{Mn,I}} = 5\,\mathrm{eV}$ and $U_{\mathrm{Fe,I}} = 1\,\mathrm{eV}$ we find a FM moment from $-0.22\,\mu_B$/Fe to $0.09\,\mu_B$/Fe. As we switch the direction of the Mn moment the effect on the Fe moment is not symmetric; the induced moment is lower when the Mn moment is parallel to the second layer of Fe as compared to the first Fe layer. This can be understood for the reason that the degree of localization is mainly reduced on the Fe layer that matches the Mn moment, and this effect is reduced with the separation from the LSMO interface [19]. The DFT calculations are consistent with a change of the LFO and LSMO symmetry resulting in a ferrimagnetic LFO ground state AF coupled to LSMO, with the magnitude of the moment sensitive to the correlation strength.

In summary, the noncompatible oxygen octahedral rotations of (111)-oriented LFO and LSMO result in atomic reconstructions at the interface, inducing $a^-a^-c^0$ octahedral rotation symmetry in the last two to four LFO layers near the interface. These reconstructions affect the electron correlations, as inferred from DFT modeling leading to a ferrimagnetic LFO ground state with AF coupling between the FM Fe and Mn. This finding is supported by XMCD, XMLD, and PNR data. This work shows the importance of structural distortions at epitaxial interfaces in forming magnetic states, and highlights the need to better understand the effect of interfaces on correlation strengths.

T.T. and T.B. acknowledge Research Council of Norway Grant No. 231290. M.N. is supported by the Project NORTEM (Grant No. 197405) within the Programme INFRA- STRUCTURE of the Research Council of Norway. The Norwegian Metacenter for Computational Science (UNINETT Sigma2) was acknowledged for providing computational resources for DFT calculations through Project No. NN9301K. The Advanced Light Source is supported by the Director, Office of Science, Office of Basic Energy Sciences, of the U.S. Department of Energy under Contract No. DE-AC02-05CH11231. Part of this work was performed at the I1011 beamline at MAX II, Sweden, and we thank Gunnar Öhrwall for his assistance at the beamline.

[1] A. Ohtomo and H. Y. Hwang, Nature **427**, 423 (2004).
[2] H. Y. Hwang, Y. Iwasa, M. Kawasaki, B. Keimer, N. Nagaosa, and Y. Tokura, Nat. Mater. **11**, 103 (2012).
[3] A. Brinkman, M. Huijben, M. van Zalk, J. Huijben, U. Zeitler, J. C. Maan, W. G. van der Wiel, G. Rijnders, D. H. A. Blank, and H. Hilgenkamp, Nat. Mater. **6**, 493 (2007).
[4] J. Chakhalian, J. W. Freeland, G. Srajer, J. Strempfer, G. Khaliullin, J. C. Cezar, T. Charlton, R. Dalgliesh, C. Bernhard, G. Cristiani, H.-U. Habermeier, and B. Keimer, Nat. Phys. **2**, 244 (2006).
[5] M. Gibert, P. Zubko, R. Scherwitzl, J. Íñiguez, and J.-M. Triscone, Nat. Mater. **11**, 195 (2012).
[6] K. S. Takahashi, M. Kawasaki, and Y. Tokura, Appl. Phys. Lett. **79**, 1324 (2001).
[7] A. J. Grutter, H. Yang, B. J. Kirby, M. R. Fitzsimmons, J. A. Aguiar, N. D. Browning, C. A. Jenkins, E. Arenholz, V. V. Mehta, U. S. Alaan, and Y. Suzuki, Phys. Rev. Lett. **111**, 087202 (2013).
[8] M. Gibert, M. Viret, A. Torres-Pardo, C. Piamonteze, P. Zubko, N. Jaouen, J.-M. Tonnerre, A. Mougin, J. Fowlie, S. Catalano, A. Gloter, O. Stéphan, and J.-M. Triscone, Nano Lett. **15**, 7355 (2015).
[9] F. Y. Bruno, M. N. Grisolia, C. Visani, S. Valencia, M. Varela, R. Abrudan, J. Tornos, A. Rivera-Calzada, A. A. Ünal, S. J. Pennycook, Z. Sefrioui, C. Leon, J. E. Villegas, J. Santamaria, A. Barthélémy, and M. Bibes, Nat. Commun. **6**, 6306 (2015).
[10] P. Yu, J. S. Lee, S. Okamoto, M. D. Rossell, M. Huijben, C. H. Yang, Q. He, J. X. Zhang, S. Y. Yang, M. J. Lee, Q. M. Ramasse, R. Erni, Y. H. Chu, D. A. Arena, C. C. Kao, L. W. Martin, and R. Ramesh, Phys. Rev. Lett. **105**, 027201 (2010).
[11] H. Wang, J. Wen, D. J. Miller, Q. Zhou, M. Chen, H. N. Lee, K. M. Rabe, and X. Wu, Phys. Rev. X **6**, 011027 (2016).
[12] E. J. Moon, R. Colby, Q. Wang, E. Karapetrova, C. M. Schlepütz, M. R. Fitzsimmons, and S. J. May, Nat. Commun. **5**, 5710 (2014).
[13] Z. Liao, M. Huijben, Z. Zhong, N. Gauquelin, S. Macke, R. J. Green, S. Van Aert, J. Verbeeck, G. Van Tendeloo, K. Held, G. A. Sawatzky, G. Koster, and G. Rijnders, Nat. Mater. **15**, 425 (2016).
[14] A. J. Grutter, A. Vailionis, J. A. Borchers, B. J. Kirby, C. L. Flint, C. He, E. Arenholz, and Y. Suzuki, Nano Lett. **16**, 5647 (2016).
[15] A. M. Glazer, Acta Crystallogr., Sect. B **28**, 3384 (1972).
[16] I. Hallsteinsen, J. E. Boschker, M. Nord, S. Lee, M. Rzchowski, P. E. Vullum, J. K. Grepstad, R. Holmestad, C. B. Eom, and T. Tybell, J. Appl. Phys. **113**, 183512 (2013).
[17] J. E. Boschker, E. Folven, A. F. Monsen, E. Wahlström, J. K. Grepstad, and T. Tybell, Cryst. Growth Des. **12**, 562 (2012).
[18] I. Hallsteinsen, M. Nord, T. Bolstad, P.-E. Vullum, J. E. Boschker, P. Longo, R. Takahashi, R. Holmestad, M. Lippmaa, and T. Tybell, Cryst. Growth Des. **16**, 2357 (2016).
[19] See Supplemental Material at http://link.aps.org/supplemental/10.1103/PhysRevB.94.201115 for more information about deposition, transmission electron microscopy measurements, spin-polarized neutron reflection measurements, and density functional theory calculations.
[20] L. Jones, H. Yang, T. J. Pennycook, M. S. J. Marshall, S. Van Aert, N. D. Browning, M. R. Castell, and P. D. Nellist, Adv. Struct. Chem. Imaging **1**, 1 (2015).
[21] F. de la Peña, P. Burdet, T. Ostasevicius, M. Sarahan, M. Nord, V. T. Fauske, J. Taillon, A Eljarrat, S Mazzucco, G. Donval, L. F. Zagonel, M. Walls, and I. Iyengar, HYPERSPY 0.8.2 (2015).
[22] G. Kresse and D. Joubert, Phys. Rev. B **59**, 1758 (1999).
[23] G. Kresse and J. Furthmüller, Phys. Rev. B **54**, 11169 (1996).
[24] J. P. Perdew, A. Ruzsinszky, G. I. Csonka, O. A. Vydrov, G. E. Scuseria, L. A. Constantin, X. Zhou, and K. Burke, Phys. Rev. Lett. **100**, 136406 (2008).
[25] D. S. Mark, M. C. Adam, M. R. James, and J. M. Steven, J. Phys.: Condens. Matter **26**, 505502 (2014).
[26] S. L. Dudarev, G. A. Botton, S. Y. Savrasov, C. J. Humphreys, and A. P. Sutton, Phys. Rev. B **57**, 1505 (1998).

[27] G. Henkelman, A. Arnaldsson, and H. Jónsson, Comput. Mater. Sci. **36**, 354 (2006).

[28] J. Lüning, F. Nolting, A. Scholl, H. Ohldag, J. W. Seo, J. Fompeyrine, J. P. Locquet, and J. Stöhr, Phys. Rev. B **67**, 214433 (2003).

[29] Y. Takamura, R. V. Chopdekar, E. Arenholz, and Y. Suzuki, Appl. Phys. Lett. **92**, 162504 (2008).

[30] I. Hallsteinsen, E. Folven, F. K. Olsen, R. V. Chopdekar, M. S. Rzchowski, C. B. Eom, J. K. Grepstad, and T. Tybell, APL Mater. **3**, 062501 (2015).

[31] Y. Jia, R. V. Chopdekar, E. Arenholz, A. T. Young, M. A. Marcus, A. Mehta, and Y. Takamura, Phys. Rev. B **92**, 094407 (2015).

[32] http://www.ncnr.nist.gov/reflpak

[33] K. Momma and F. Izumi, J. Appl. Crystallogr. **44**, 1272 (2011).

Part III

Conclusion and outlook

Chapter 4

Conclusion

The aim of this project has been to study the interfaces of perovskite oxide heterostructures, to better understand the physics of these material systems. To achieve this Transmission Electron Microscopy was utilized to study the crystal and electronic structure at the ångstrom level. This has been facilitated by work on improving the data analysis tools for both STEM imaging and EELS.

In Paper I, the $La_{0.7}Sr_{0.3}MnO_3$ thin films grown on $SrTiO_3$-(001) were characterized using STEM-HAADF and STEM-EELS. The HAADF data was analysed using GPA, which showed a region with elongated unit cell in the LSMO film. This region started at the LSMO/STO interface, and extended about 3 nm into the LSMO film. Studying the EELS data, the same region was found to contain reduced oxygen content and a lower manganese oxidation state. Coupled with DFT calculations, this was attributed to a brownmillerite phase in this region. Furthermore, after 1.5 years an ordered brownmillerite structure had formed in the same region.

Paper II studied how electron beam damage affects LSMO and STO at 80 and 200 kV acceleration voltages. It shows how the two materials respond differently to being subject to a sharp and intense electron beam. i) LSMO had large changes in O-K and Mn-$L_{2,3}$ ELNES at both 80 and 200 kV, but no changes in the HAADF image. This is consistent with oxygen being removed from the crystal structure by the electron beam. ii) STO showed no signs of beam damage at 80 kV, but large changes in both EELS and HAADF at 200 kV. In addition, the low loss EELS showed a large reduction in thickness as a function of beam exposure. This is consistent with material being sputtered away by the electron beam. iii) The exposed LSMO area was 2 nm, but the effects of the exposure extended to a 20 nm wide area. In relation to data processing, the paper presents a way to quantitatively analyse the fine structure in core loss edges using the model based approach. This is done by implementing a method for quantitatively setting the

core loss edge onsets, which is in the process of being integrated into HyperSpy.

Paper III used the EELS processing methodology developed during the work with Paper II to explore the effects of cation intermixing at the interface. Here, LSMO/STO-(111) and LSMO/LFO/STO-(111) were analysed with STEM-EELS and STEM-HAADF. The EELS data showed that on the film/STO-interface, there was a 0.25-0.3 nm layer with intermixing of the A- and B-cations from the substrate and film. This intermixing was not seen at the interface of the LSMO/LFO thin films. The intermixing was attributed to the polar nature of the (111)-STO surface.

The aim of Paper IV was to improve the data analysis of atomic resolution STEM images. Specifically, we show how to accurately and quantitatively find the position of the oxygen atomic columns in perovskite oxide materials. This was a challenge, due to oxygen commonly being the lightest element in the perovskite oxides. This was solved by using the modelling framework of HyperSpy, where the more intense atomic columns were fitted with 2-D Gaussians and removed from the data. Furthermore, by using nearest neighbor statistics, major symmetry axes were automatically found, and atomic planes constructed. Then, calculation of average distance maps ("strain maps") became trivial.

In Paper V, both the improved EELS processing methodology from Paper II and the improved STEM image methodology from Paper IV were utilized on an LSMO (4 nm)/LFO (4 nm)/STO-(111) bilayer system. Here, the oxidation state of Fe and Mn were studied using STEM-EELS, revealing no significant difference between the bulk of the film and the interfaces. Ergo, no significant variations in the oxidation state of either manganese or iron in the LSMO/LFO bilayer were found. Next, the shape and position of the A-cation and oxygen atomic columns were examined using high-resolution STEM-HAADF, ABF and the method from Paper IV, showing structural distortions at the LSMO/LFO interface, that were not present in either LSMO or LFO films.

Chapter 5

Outlook

There are aspects of this work which can lead towards new research avenues.

One possible extension of the beam exposure investigation in Paper II, is examining more materials at several acceleration voltages. The paper only did an in-depth study of LSMO and STO, so other commonly studied perovskite oxides such as $LaFeO_3$, $La_{1-x}Ca_xMnO_3$, $LaAlO_3$ and LSMO with different doping amounts would be of interest. Also studying the effect of several acceleration voltages would be useful, since some of the commonly used ones were not examined: 60, 100, 120, 300 kV. This could give a map for material tolerance to beam intensity.

Another possible study would be to further examine the LSMO/LFO/STO-(111) thin film system, and other bilayer systems. This could include analysing a system where the different thin film layers have different thicknesses, to better understand the strain relaxation mechanisms in these kinds of systems. For example by using the open source Atomap software presented in Paper IV, a great deal of information about the oxygen octahedron tilt pattern can be extracted. This can shed some light on the structure of the interface, which is hard to determine with other types of microscopy techniques.

The Atomap functionalities themselves can be extended, especially towards more statistical approaches, and the use of PCA to study the shapes of atomic columns. This processing outputs a large amount of possible parameters, such as position, ellipticity, distance to all neighboring atoms, projected unit cell volume and angles. With such a large amount of values, one can easily employ more statistical approaches to label and sort the different atomic columns. This would again make it much easier to automatically process and analyse larger datasets.

Another important aspect is the increasing popularity of open data. Open data is important, since it allows for other researchers to analyse the same data with different analysis methods, which reduces the duplication of work. It is also

important for reproducibility, since it allows for other researchers to run analysis on the data to check if the data processing and interpretation of the data is correct. In addition, having access to high quality reference data makes it much easier for people developing new analysis tools to check their methods against datasets with known structure and properties. Luckily, more and more funders are starting to require that all data used in published research is uploaded to an open data repository, so anyone can access this data.

Closely linked to open data, is the increasing popularity of open source software for use in research. This does not mean only using open source software made by other people, but publishing their own internal software tools or contributing to software projects. This is especially important in an academic environment, where the majority of the software development is done by temporarily employed PhD or Post Docs. Normally, the analysis tools developed by these temporary employees would just remain on a hard drive after their position or project ended. By instead contributing to an open source project, other people could benefit and improve upon the work. This avoids work duplication, and lowers the barriers of entry for doing advanced analysis. In addition, using open source software means better reproducibility since one can check exactly how data processing produces the results.

From a material physics perspective, one goal is to get a more comprehensive understanding of the perovskite oxide heterostructures. Especially, how the thin film material adapts to being grown on a substrate, and how the thin film affects the substrate material close to the interface. This knowledge could make it possible to tailor-make functional properties, by tuning chemical and structural parameters such as doping, film thickness and substrate orientation. The development of such a comprehensive understanding will include information obtained using STEM and EELS. HyperSpy and Atomap can be important tools for analysis of such data since they are openly available. Interesting systems to study could be nano-patterned thin film systems[77] and other thin film systems with complicated domain structures.

Bibliography

[1] J. Mannhart and D. G. Schlom. "Oxide Interfaces–An Opportunity for Electronics". en. In: *Science* 327.5973 (Mar. 2010). DOI: 10.1126/science.1181862.

[2] G. Hammerl and N. Spaldin. "Shedding Light on Oxide Interfaces". en. In: *Science* 332.6032 (May 2011). DOI: 10.1126/science.1206247.

[3] L. W. Martin, Y.-H. Chu, and R. Ramesh. "Advances in the growth and characterization of magnetic, ferroelectric, and multiferroic oxide thin films". en. In: *Materials Science and Engineering: R: Reports* 68.4-6 (May 2010). DOI: 10.1016/j.mser.2010.03.001.

[4] Elbio Dagotto, Takashi Hotta, and Adriana Moreo. "Colossal magnetoresistant materials: the key role of phase separation". In: *Physics Reports* 344.1 (2001). DOI: 10.1016/S0370-1573(00)00121-6.

[5] J. Wang, J. B. Neaton, H. Zheng, V. Nagarajan, S. B. Ogale, B. Liu, D. Viehland, V. Vaithyanathan, D. G. Schlom, U. V. Waghmare, N. A. Spaldin, K. M. Rabe, M. Wuttig, and R. Ramesh. "Epitaxial $BiFeO_3$ Multiferroic Thin Film Heterostructures". In: *Science* 299.5613 (2003), pp. 1719–1722. DOI: 10.1126/science.1080615.

[6] I. Hallsteinsen, J. E. Boschker, M. Nord, S. Lee, M. Rzchowski, P. E. Vullum, J. K. Grepstad, R. Holmestad, C. B. Eom, and T. Tybell. "Surface stability of epitaxial $La_{0.7}Sr_{0.3}MnO_3$ thin films on (111)-oriented $SrTiO_3$". In: *Journal of Applied Physics* 113.18, 183512 (2013). DOI: 10.1063/1.4804312.

[7] H. W. Jang, D. A. Felker, C. W. Bark, Y. Wang, M. K. Niranjan, C. T. Nelson, Y. Zhang, D. Su, C. M. Folkman, S. H. Baek, S. Lee, K. Janicka, Y. Zhu, X. Q. Pan, D. D. Fong, E. Y. Tsymbal, M. S. Rzchowski, and C. B. Eom. "Metallic and Insulating Oxide Interfaces Controlled by Electronic Correlations". en. In: *Science* 331.6019 (Feb. 2011). DOI: 10.1126/science.1198781.

[8] Ch Renner, G Aeppli, B-G Kim, Yeong-Ah Soh, and S-W Cheong. "Atomic-scale images of charge ordering in a mixed-valence manganite". In: *Nature* 416.6880 (2002), pp. 518–521. DOI: 10.1038/416518a.

[9] Jak Chakhalian, JW Freeland, G Srajer, J Strempfer, G Khaliullin, JC Cezar, T Charlton, R Dalgliesh, Ch Bernhard, G Cristiani, et al. "Magnetism at the interface between ferromagnetic and superconducting oxides". In: *Nature Physics* 2.4 (2006), pp. 244–248. DOI: 10.1038/nphys272.

[10] I. Hallsteinsen, E. Folven, F. K. Olsen, R. V. Chopdekar, M. S. Rzchowski, C. B. Eom, J. K. Grepstad, and T. Tybell. "Crystalline symmetry controlled magnetic switching in epitaxial (111) $La_{0.7}Sr_{0.3}MnO_3$ thin films". In: *APL Mater.* 3.6, 062501 (2015). DOI: 10.1063/1.4907877.

[11] D. B. Williams and C. B. Carter. *Transmission Electron Microscopy*. United States of America: Springer, 2009. DOI: 10.1007/978-0-387-76501-3.

[12] Max Haider, Harald Rose, Stephan Uhlemann, Eugen Schwan, Bernd Kabius, and Knut Urban. "A spherical-aberration-corrected 200kV transmission electron microscope". In: *Ultramicroscopy* 75.1 (1998). DOI: 10.1016/S0304-3991(98)00048-5.

[13] P. D. Nellist, M. F. Chisholm, N. Dellby, O. L. Krivanek, M. F. Murfitt, Z. S. Szilagyi, A. R. Lupini, A. Borisevich, W. H. Sides, and S. J. Pennycook. "Direct Sub-Angstrom Imaging of a Crystal Lattice". en. In: *Science* 305.5691 (Sept. 2004). DOI: 10.1126/science.1100965.

[14] R Erni. *Aberration-Corrected Imaging in Transmission Electron Microscopy*. Singapore: Imperial Collage Press, 2010.

[15] David A. Muller, Earl J. Kirkland, Malcolm G. Thomas, John L. Grazul, Lena Fitting, and Matthew Weyland. "Room design for high-performance electron microscopy". In: *Ultramicroscopy* 106.11–12 (2006), pp. 1033–1040. DOI: 10.1016/j.ultramic.2006.04.017.

[16] Lewys Jones, Hao Yang, Timothy J. Pennycook, Matthew S. J. Marshall, Sandra Van Aert, Nigel D. Browning, Martin R. Castell, and Peter D. Nellist. "Smart Align—a new tool for robust non-rigid registration of scanning microscope data". en. In: *Advanced Structural and Chemical Imaging* 1.1 (Dec. 2015). DOI: 10.1186/s40679-015-0008-4.

[17] F.-T. Huang, A. Gloter, M.-W. Chu, F. C. Chou, G. J. Shu, L.-K. Liu, C. H. Chen, and C. Colliex. "Scanning Transmission Electron Microscopy Using Selective High-Order Laue Zones: Three-Dimensional Atomic Ordering in Sodium Cobaltate". In: *Phys. Rev. Lett.* 105 (12 Sept. 2010), p. 125502. DOI: 10.1103/PhysRevLett.105.125502.

[18] S.J. Pennycook and D.E. Jesson. "High-resolution Z-contrast imaging of crystals". In: *Ultramicroscopy* 37.1 (1991), pp. 14–38. DOI: 10.1016/0304-3991(91)90004-P.

[19] David A. Muller, Naoyuki Nakagawa, Akira Ohtomo, John L. Grazul, and Harold Y. Hwang. "Atomic-scale imaging of nanoengineered oxygen vacancy profiles in $SrTiO_3$". In: *Nature* 430.7000 (Aug. 2004). DOI: 10.1038/nature02756.

[20] J. M. LeBeau, S. D. Findlay, L. J. Allen, and S. Stemmer. "Quantitative STEM: Experimental Methods and Applications". In: *Journal of Physics: Conference Series* 371.1 (2012), p. 012053. DOI: 10.1088/1742-6596/371/1/012053.

[21] S.J. Pennycook. "Structure determination through Z-contrast microscopy". In: *Microscopy, Spectroscopy, Holography and Crystallography with Electrons*. Ed. by Gianluca Calestani Peter W. Hawkes Pier Georgio Merli and Marco Vittori-Antisari. Vol. 123. Advances in Imaging and Electron Physics. Elsevier, 2002, pp. 173–206. DOI: 10.1016/S1076-5670(02)80063-5.

[22] Eiji Okunishi, Hidetaka Sawada, and Yukihito Kondo. "Experimental study of annular bright field (ABF) imaging using aberration-corrected scanning transmission electron microscopy (STEM)". In: *Micron* 43.4 (2012), pp. 538–544. DOI: 10.1016/j.micron.2011.10.007.

[23] Ryotaro Aso, Daisuke Kan, Yuichi Shimakawa, and Hiroki Kurata. "Octahedral Tilt Propagation Controlled by A-Site Cation Size at Perovskite Oxide Heterointerfaces". In: *Crystal Growth & Design* 14.5 (2014), pp. 2128–2132. DOI: 10.1021/cg500285m.

[24] S.D. Findlay, N. Shibata, H. Sawada, E. Okunishi, Y. Kondo, and Y. Ikuhara. "Dynamics of annular bright field imaging in scanning transmission electron microscopy". In: *Ultramicroscopy* 110.7 (2010), pp. 903–923. DOI: 10.1016/j.ultramic.2010.04.004.

[25] Naoya Shibata, Scott D Findlay, Yuji Kohno, Hidetaka Sawada, Yukihito Kondo, and Yuichi Ikuhara. "Differential phase-contrast microscopy at atomic resolution". In: *Nature Physics* 8.8 (2012), pp. 611–615. DOI: 10.1038/nphys2337.

[26] Matus Krajnak, Damien McGrouther, Dzmitry Maneuski, Val O' Shea, and Stephen McVitie. "Pixelated detectors and improved efficiency for magnetic imaging in STEM differential phase contrast". In: *Ultramicroscopy* 165 (2016), pp. 42–50. DOI: 10.1016/j.ultramic.2016.03.006.

[27] Ray F Egerton. *Electron energy-loss spectroscopy in the electron microscope*. Springer Science & Business Media, 2011. DOI: 10.1007/978-1-4419-9583-4.

[28] Ondrej L. Krivanek, Tracy C. Lovejoy, Niklas Dellby, and R.W. Carpenter. "Monochromated STEM with a 30 meV-wide, atom-sized electron probe". In: *Microscopy* 62.1 (2013), pp. 3–21. DOI: 10.1093/jmicro/dfs089.

[29] M. Varela, M. P. Oxley, W. Luo, J. Tao, M. Watanabe, A. R. Lupini, S. T. Pantelides, and S. J. Pennycook. "Atomic-resolution imaging of oxidation states in manganites". In: *Physical Review B* 79.8 (Feb. 2009). DOI: 10.1103/PhysRevB.79.085117.

[30] D. A. Muller, L. F. Kourkoutis, M. Murfitt, J. H. Song, H. Y. Hwang, J. Silcox, N. Dellby, and O. L. Krivanek. "Atomic-Scale Chemical Imaging of Composition and Bonding by Aberration-Corrected Microscopy". In: *Science* 319.5866 (Feb. 2008). DOI: 10.1126/science.1148820.

[31] Haiyan Tan, Jo Verbeeck, Artem Abakumov, and Gustaaf Van Tendeloo. "Oxidation state and chemical shift investigation in transition metal oxides by EELS". In: *Ultramicroscopy* 116 (May 2012). DOI: 10.1016/j.ultramic.2012.03.002.

[32] Shuji Nishida, Shunsuke Kobayashi, Akihito Kumamoto, Hidekazu Ikeno, Teruyasu Mizoguchi, Isao Tanaka, Yuichi Ikuhara, and Takahisa Yamamoto. "Effect of local coordination of Mn on Mn-$L_{2,3}$ edge electron energy loss spectrum". en. In: *Journal of Applied Physics* 114.5 (2013). DOI: 10.1063/1.4817425.

[33] P. S. Sankara Rama Krishnan, Anna N. Morozovska, Eugene A. Eliseev, Quentin M. Ramasse, Demie Kepaptsoglou, Wen-I. Liang, Ying-Hao Chu, Paul Munroe, and V. Nagarajan. "Misfit strain driven cation inter-diffusion across an epitaxial multiferroic thin film interface". en. In: *Journal of Applied Physics* 115.5 (Feb. 2014). DOI: 10.1063/1.4862556.

[34] Ingrid Hallsteinsen, Magnus Nord, Torstein Bolstad, Per-Erik Vullum, Jos E. Boschker, Paulo Longo, Ryota Takahashi, Randi Holmestad, Mikk Lippmaa, and Thomas Tybell. "Effect of Polar (111)-Oriented $SrTiO_3$ on Initial Perovskite Growth". In: *Crystal Growth & Design* 16.4 (2016), pp. 2357–2362. DOI: 10.1021/acs.cgd.6b00143.

[35] Naoyuki Nakagawa, Harold Y. Hwang, and David A. Muller. "Why some interfaces cannot be sharp". In: *Nature Materials* 5.3 (Mar. 2006). DOI: 10.1038/nmat1569.

[36] Akira Ohtomo, DA Muller, JL Grazul, and H Yu Hwang. "Artificial charge-modulationin atomic-scale perovskite titanate superlattices". In: *Nature* 419.6905 (2002), pp. 378–380. DOI: 10.1038/nature00977.

[37] Manoubi, Tahar, Tencé, Marcel, Walls, Michael Gerard, and Colliex, Christian. "Curve fitting methods for quantitative analysis in electron energy loss spectroscopy". In: *Microsc. Microanal. Microstruct.* 1.1 (1990), pp. 23–39. DOI: 10.1051/mmm:019900010102300.

[38] M. J. Hÿtch, E. Snoeck, and R. Kilaas. "Quantitative measurement of displacement and strain fields from HREM micrographs". In: *Ultramicroscopy* 74.3 (1998), pp. 131–146. DOI: 10.1016/S0304-3991(98)00035-7.

[39] Yuanyuan Zhu, Colin Ophus, Jim Ciston, and Haiyan Wang. "Interface lattice displacement measurement to 1pm by geometric phase analysis on aberration-corrected HAADF STEM images". en. In: *Acta Materialia* 61.15 (Sept. 2013), pp. 5646–5663. DOI: 10.1016/j.actamat.2013.06.006.

[40] Yi Wang, Ute Salzberger, Wilfried Sigle, Y. Eren Suyolcu, and Peter A. van Aken. "Oxygen octahedra picker: A software tool to extract quantitative information from STEM images". In: *Ultramicroscopy* 168 (2016), pp. 46–52. DOI: 10.1016/j.ultramic.2016.06.001.

[41] A. De Backer, K.H.W. van den Bos, W. Van den Broek, J. Sijbers, and S. Van Aert. "StatSTEM: An efficient approach for accurate and precise model-based quantification of atomic resolution electron microscopy images". In: *Ultramicroscopy* 171 (2016), pp. 104–116. DOI: 10.1016/j.ultramic.2016.08.018.

[42] AlbinaY. Borisevich, Oleg S. Ovchinnikov, Hye Jung Chang, Mark P. Oxley, Pu Yu, Jan Seidel, Eugine A. Eliseev, Anna N. Morozovska, Ramamoorthy Ramesh, Stephen J. Pennycook, and Sergei V. Kalinin. "Mapping Octahedral Tilts and Polarization Across a Domain Wall in $BiFeO_3$ from Z-Contrast Scanning Transmission Electron Microscopy Image Atomic Column Shape Analysis". In: *ACS Nano* 4.10 (2010), pp. 6071–6079. DOI: 10.1021/nn1011539.

[43] Qian He, Ryo Ishikawa, Andrew R. Lupini, Liang Qiao, Eun J. Moon, Oleg Ovchinnikov, Steven J. May, Michael D. Biegalski, and Albina Y. Borisevich. "Towards 3D Mapping of BO_6 Octahedron Rotations at Perovskite Heterointerfaces, Unit Cell by Unit Cell". In: *ACS Nano* 9.8 (2015), pp. 8412–8419. DOI: 10.1021/acsnano.5b03232.

[44] Tony Hey and Mike C Payne. "Open science decoded". In: *Nature Physics* 11.5 (2015), pp. 367–369. DOI: 10.1038/nphys3313.

[45] Nick Barnes. "Publish your computer code: it is good enough". In: *Nature* 467.7317 (2010), pp. 753–753. DOI: 10.1038/467753a.

[46] Andreas Prlić and James B Procter. "Ten simple rules for the open development of scientific software". In: *PLoS Comput Biol* 8.12 (2012), e1002802. DOI: 10.1371/journal.pcbi.1002802.

[47] Helen D. Megaw. "Crystal Structure of Barium Titanate". In: *Nature* 155 (Apr. 1945), pp. 484–485. DOI: 10.1038/155484b0.

[48] D. Taylor. "Thermal expansion data. VIII: Complex oxides, ABO_3, the perovskites". In: *British ceramic. Transactions and journal* 84.6 (1985), pp. 181–188.

[49] P.E. Vullum. "Ferroelastic $LaCoO_3$-based Polycrystalline Ceramics". PhD thesis. NTNU, 2005.

[50] James M. Rondinelli and Nicola A. Spaldin. "Structure and Properties of Functional Oxide Thin Films: Insights From Electronic-Structure Calculations". In: *Advanced Materials* 23.30 (2011), pp. 3363–3381. DOI: 10.1002/adma.201101152.

[51] J. H. Haeni, P. Irvin, W. Chang, R. Uecker, P. Reiche, Y. L. Li, S. Choudhury, W. Tian, M. E. Hawley, B. Craigo, A. K. Tagantsev, X. Q. Pan, S. K. Streiffer, L. Q. Chen, S. W. Kirchoefer, J. Levy, and D. G. Schlom. "Room-temperature ferroelectricity in strained $SrTiO_3$". In: *Nature* 430.7001 (Aug. 2004). DOI: 10.1038/nature02773.

[52] Marta Gibert, Pavlo Zubko, Raoul Scherwitzl, Jorge Íñiguez, and Jean-Marc Triscone. "Exchange bias in $LaNiO_3$–$LaMnO_3$ superlattices". In: *Nat Mater* 11 (3 2012). DOI: 10.1038/nmat3224.

[53] V. Nagarajan, C. S. Ganpule, H. Li, L. Salamanca-Riba, A. L. Roytburd, E. D. Williams, and R. Ramesh. "Control of domain structure of epitaxial $PbZr_{0.2}Ti_{0.8}O_3$ thin films grown on vicinal (001) $SrTiO_3$ substrates". In: *Applied Physics Letters* 79.17 (2001), pp. 2805–2807. DOI: 10.1063/1.1402645.

[54] E. Dagotto. "When Oxides Meet Face to Face". In: *Science* 318.5853 (Nov. 2007). DOI: 10.1126/science.1151094.

[55] J.-S. Lee, Y. W. Xie, H. K. Sato, C. Bell, Y. Hikita, H. Y. Hwang, and C.-C. Kao. "Titanium dxy ferromagnetism at the $LaAlO_3/SrTiO_3$ interface". In: *Nature Materials* 12.8 (June 2013). DOI: 10.1038/nmat3674.

[56] A-M Haghiri-Gosnet and J-P Renard. "CMR manganites: physics, thin films and devices". In: *Journal of Physics D: Applied Physics* 36.8 (2003), R127. DOI: 10.1088/0022-3727/36/8/201.

[57] J.-S. Lee, D. A. Arena, T. S. Santos, C. S. Nelson, S. I. Hyun, J. H. Shim, and C.-C. Kao. "Controlling competing interactions at oxide interfaces: Enhanced anisotropy in $La_{0.7}Sr_{0.3}MnO_3$ films via interface engineering". en. In: *Physical Review B* 85.23 (June 2012). DOI: 10.1103/PhysRevB.85.235125.

[58] Evgeny Y Tsymbal, Elbio RA Dagotto, Chang-Beom Eom, and Ramamoorthy Ramesh. *Multifunctional oxide heterostructures*. OUP Oxford, 2012. DOI: 10.1093/acprof:oso/9780199584123.001.0001.

[59] Robert Eason. *Pulsed laser deposition of thin films: applications-led growth of functional materials*. John Wiley & Sons, 2006. DOI: 10.1002/0470052120.

[60] Sayani Majumdar and Sebastiaan van Dijken. "Pulsed laser deposition of $La_{1-x}Sr_xMnO_3$: thin-film properties and spintronic applications". In: *Journal of Physics D: Applied Physics* 47.3 (2013), p. 034010. DOI: 10.1088/0022-3727/47/3/034010.

[61] Guus JHM Rijnders, Gertjan Koster, Dave HA Blank, and Horst Rogalla. "In situ monitoring during pulsed laser deposition of complex oxides using reflection high energy electron diffraction under high oxygen pressure". In: *Applied physics letters* 70.14 (1997), pp. 1888–1890. DOI: 10.1063/1.118687.

[62] Emil Christiansen. "TEM Characterization of $LaFeO_3$ Thin Films on $SrTiO_3$ (111) Substrates". MA thesis. Norwegian University of Science and Technology, 2015.

[63] E Christiansen, M Nord, I Hallsteinsen, P E Vullum, T Tybell, and R Holmestad. "Structural investigation of epitaxial $LaFeO_3$ thin films on (111) oriented $SrTiO_3$ by transmission electron microscopy". In: *Journal of Physics: Conference Series* 644.1 (2015), p. 012002. DOI: 10.1088/1742-6596/644/1/012002.

[64] M Basletic, J-L Maurice, C Carrétéro, Gervasi Herranz, Olivier Copie, Manuel Bibes, Éric Jacquet, Karim Bouzehouane, Stephen Fusil, and Agnes Barthélémy. "Mapping the spatial distribution of charge carriers in $LaAlO_3/SrTiO_3$ heterostructures". In: *Nature materials* 7.8 (2008), pp. 621–625. DOI: 10.1038/nmat2223.

[65] A Ohtomo and HY Hwang. "A high-mobility electron gas at the $LaAlO_3/SrTiO_3$ heterointerface". In: *Nature* 427.6973 (2004), pp. 423–426. DOI: 10.1038/nature02308.

[66] M. Bosman, V. J. Keast, J. L. Garcı/a-Muñoz, A. J. D'Alfonso, S. D. Findlay, and L. J. Allen. "Two-Dimensional Mapping of Chemical Information at Atomic Resolution". In: *Phys. Rev. Lett.* 99 (8 Aug. 2007), p. 086102. DOI: 10.1103/PhysRevLett.99.086102.

[67] Channing C. Ahn and Peter Rez. "Inner shell edge profiles in electron energy loss spectroscopy". In: *Ultramicroscopy* 17.2 (1985), pp. 105–115. DOI: 10.1016/0304-3991(85)90003-8.

[68] T. Riedl, T. Gemming, and K. Wetzig. "Extraction of EELS white-line intensities of manganese compounds: Methods, accuracy, and valence sensitivity". In: *Ultramicroscopy* 106.4–5 (2005), pp. 284–291. DOI: 10.1016/j.ultramic.2005.09.002.

[69] T. Riedl, T. Gemming, W. Gruner, J. Acker, and K. Wetzig. "Determination of manganese valency in $La_{1-x}Sr_xMnO_3$ using ELNES in the (S)TEM". In: *Micron* 38.3 (2007), pp. 224–230. DOI: 10.1016/j.micron.2006.06.017.

[70] Ian MacLaren, Rafael Villaurrutia, Bernhard Schaffer, Lothar Houben, and Aimé Peláiz-Barranco. "Atomic-Scale Imaging and Quantification of Electrical Polarisation in Incommensurate Antiferroelectric Lanthanum-Doped Lead Zirconate Titanate". In: *Advanced Functional Materials* 22.2 (2012), pp. 261–266. DOI: 10.1002/adfm.201101220.

[71] J. D. Ferguson, Y. Kim, L. Fitting Kourkoutis, A. Vodnick, A. R. Woll, D. A. Muller, and J. D. Brock. "Epitaxial Oxygen Getter for a Brownmillerite Phase Transformation in Manganite Films". In: *Advanced Materials* 23.10 (2011), pp. 1226–1230. DOI: 10.1002/adma.201003581.

[72] J. Gazquez, Shameek Bose, M. Sharma, M. A. Torija, S. J. Pennycook, C. Leighton, and M. Varela. "Lattice mismatch accommodation via oxygen vacancy ordering in epitaxial $La_{0.5}Sr_{0.5}CoO_{3-\delta}$ thin films". In: *APL Mater.* 1.1, 012105 (2013). DOI: 10.1063/1.4809547.

[73] Jian-Min Zuo, Amish B. Shah, Honggyu Kim, Yifei Meng, Wenpei Gao, and Jean-Luc Rouviére. "Lattice and strain analysis of atomic resolution Z-contrast images based on template matching". In: *Ultramicroscopy* 136 (2014), pp. 50–60. DOI: 10.1016/j.ultramic.2013.07.018.

[74] L.J. Allen, S.D. Findlay, M.P. Oxley, and C.J. Rossouw. "Lattice-resolution contrast from a focused coherent electron probe. Part I". In: *Ultramicroscopy* 96.1 (2003), pp. 47–63. DOI: 10.1016/S0304-3991(02)00380-7.

[75] *iMtools*. http://www.er-c.org/centre/software/imtools.htm.

[76] Stephen M. Anthony and Steve Granick. "Image Analysis with Rapid and Accurate Two-Dimensional Gaussian Fitting". en. In: *Langmuir* 25.14 (July 2009), pp. 8152–8160. DOI: 10.1021/la900393v.

[77] E. Folven, J. Linder, O. V. Gomonay, A. Scholl, A. Doran, A. T. Young, S. T. Retterer, V. K. Malik, T. Tybell, Y. Takamura, and J. K. Grepstad. "Controlling the switching field in nanomagnets by means of domain-engineered antiferromagnets". In: *Phys. Rev. B* 92 (9 Sept. 2015), p. 094421. DOI: 10.1103/PhysRevB.92.094421.

Part IV

Appendix

FIB recipe

FIB cross section sample preparation of STO-(111) heterostructures

Magnus Nord

1 Introduction

This is a guide on how to make a cross section Transmission Electron Microscopy (TEM) sample of perovskite heterostructures grown on (111)-$SrTiO_3$ (STO) using a Focused Ion Beam (FIB). The procedure is the same as regular TEM FIB samplepreparation using liftout, except for the final thinning and having a thicker protective layer. This is due to (111)-oriented STO seems to bend more easily compared to other materials, and other orientations of STO. Thus the thinning part is optimized for only having a small region (about 2 µm) which is optimal for high-end TEM work. Before putting the sample in the FIB, it is recommended to sputter coat on a thin layer (20 nm) of for example Pd/Pt. Firstly it protects the sample from "stray" gallium ions in the FIB, which can (possibly) happen when changing apertures on the gallium beam. Secondly it reduces the possibility of charge-up, which I've observed on samples which should be conductive (like doped STO). This can be due to bad contact between the wafer and carbon tape, so use both rotation and tilt on the sputter coater. Thirdly it can help with thermal conduction, which is a possible mechanism for beam damage when using high-intensity probes in the TEM.

However, the Pd/Pt-layer will introduce a "curtaining effect", creating some variations in sample thickness. This is caused by the nano crystallinity of this layer.

These instructions are for a Helios NanoLab DualBeam FIB, but the general steps should be applicable for any FIB.

2 General instructions

- Take pictures through the whole process
- Do not place the TEM grids on outer part of TEM grid holder. It is easy to touch them by accident when loading the holder into the FIB

3 Depositing protective layer

- If you have some kind of feature to align the sample
  - In menu: Stage → xT-align feature
  - This will rotate the stage
- In Pattering menu → Gas injection → in Pt-needle right click "Cold" and select "Heat"
- Pt-protection using electron beam
  - Make rectangular pattern, 12 µm x 3 µm, z=0.2 µm(?)
  - Select "Pt e-dep structure"
  - High e-beam current, 2.7 nA
  - Set e-beam to 3 keV
  - Go to 0° tilt
  - Insert Pt-needle
  - Do deposition. About 1 minutes, dwell time 1 µs
  - Retract Pt-needle
  - Cool down Pt-needle
- C-protection using electron beam (only insert C-needle at 52° tilt)
  - Go to 52° tilt
  - Warm C-needle
  - Make rectangular pattern, 12 µm x 3 µm, z=1 µm (right on top of the previous deposition)
  - Select "C e-dep surface"
  - Insert C-needle
  - Do deposition. About 4 minutes, 200 ns dwell time
- Change e-beam back to imaging (15 keV, 0.17 nA)
- C-protection using ion beam
  - 30 keV ion beam energy
  - 0.27 nA ion beam current
  - Align ion beam away from region of interest
  - Make rectangular pattern, 12 µm x 3 µm, z=4 µm (right on top of the previous deposition)
  - Select "C dep"
  - Insert C-needle
  - Do deposition. About 11 minutes, 200 ns dwell time
  - Turn off C-needle heating, retract needle
- See figure 1 for how the end result should look.

4 Make trenches

- Maximum ion beam current, 20 nA
- Align ion beam away from protective layer
- Use regular cross section, 22 µm x 15 µm, z=18 µm. Have a small gap between protective layer and trench, due to ion beam not being completely sharp (see fig. 4)
- Direction: bottom to top. Application: "Si"
- Select "Multiscan" in advanced patterning, multi-passes = 4
- Do milling. About 4 minutes, 1 µs dwell time
- Repeat trench on other side, but switch direction to top to bottom

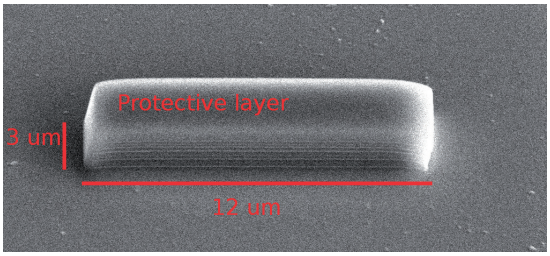

Figure 1: Protective layer

5 "J-cut", under and side of sample

- Check sample at 0° tilt
- Go to -9° to get a better under-cut
- Ion beam current 6.5 nA
- Use rectangle pattern, under and sides (see fig. 4) , use parallel milling to reduce redeposition
- Continue milling until you see a "cut" in the trench on the other side using the electron beam. 4-6 minutes.
- Tilt back to 52°, and cut away redepositions on the sample using cleaning cross section
- Make sure there are no parts of the sample, expect the "bridge" which is connected to the rest of the material. Use cleaning cross section to remove.

6 Omniprobe

- Before insertion: go to "Park position"
- Go to 0°, make sure you are at eucentric height
- In pattering menu: "Insert omniprobe"
- If omniprobe in unsharp
  - Move away from the sample
  - Go to high Z
  - Put probe in eucentric height (in the middle of both the e- and i-beam)

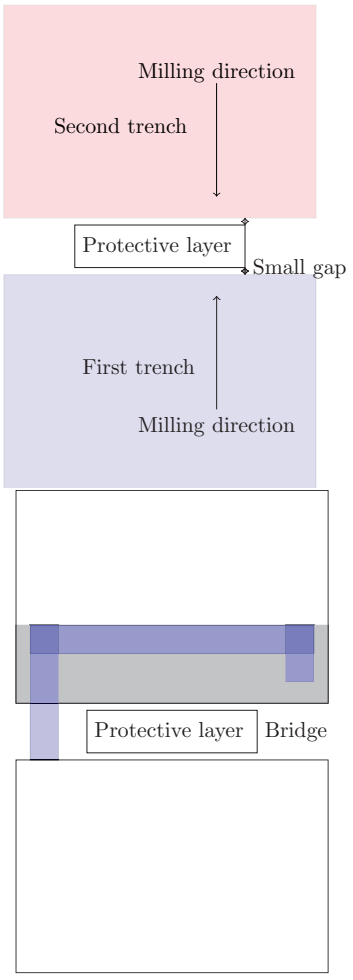

Figure 2: How to make the trenches

  - In pattering, use polygon to make the omniprobe sharper
  - Do milling
  - Rotate omniprobe 90° physically on the FIB
  - Do the same polygon milling
  - Rotate omniprobe back to original position
- Go to region of interest
- Go to "Eucentric high"
- Under probe control: "Velocity", "Stage for"
- Move omniprobe to middle of electron beam using X (X direction is shared for electron and ion beam)
- Move sample so omniprobe is right over the protective layer when using the electron beam
- Lower the omniprobe (downwards Z), while using the ion beam at low current (9 pA) to check the height.
- When the omniprobe is fairly close, insert the Pt-needle and switch to deposition ion beam current (0.27 nA). Inserting the Pt-needle and changing ion beam aperture will cause slight movement in the FIB, which could possibly break off the sample if the omniprobe is touching the sample.
- Bring the omniprobe in contact to the left corner of the protective layer. Use very slow speed on the omniprobe. See figure 3.
- When it touches, bring it a little closer to apply a little bit of force, to keep the omniprobe from moving when depositing the Pt. Might get a touch alarm when omniprobe touches the sample.
- Do NOT move the stage at after this point, use image shift to move the ion or electron beam. Lock the stage movement to be sure.
- Do a 2 µm x 2 µm x 2 µm Pt deposition. Application "Pt dep". Use top to bottom deposition to start the deposition on the sample.
- Retract the Pt-needle. This is to avoid Pt being deposited while milling away the bridge.
- Mill away the remaining "bridge", application "Si".
- Slowly raise the Omniprobe (positive Z)
- Lower ion beam current to imaging (9 pA), check width of liftout-sample
- Omniprobe: go to "Eucentric high", then "Park", then retract the omniprobe

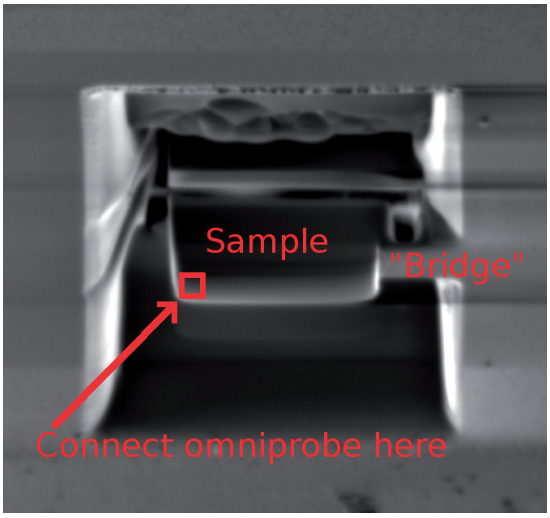

Figure 3:

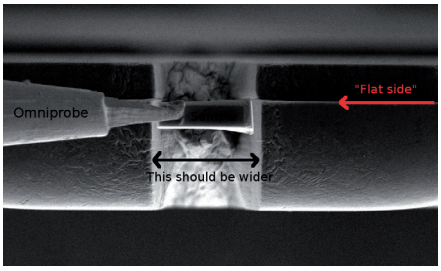

Figure 4:

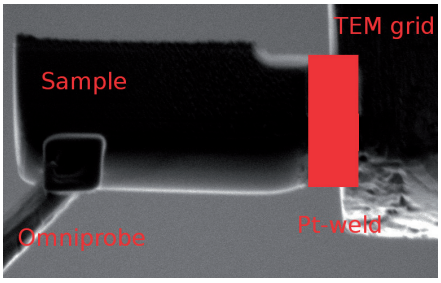

Figure 5: Connecting the liftout sample to the TEM-grid

7 TEM grid

- Go to the TEM-grid holder (probably downwards, if grid holder was on the right part when loading)
- Set eucentric height and point of coincidence
- Mill away a hole in one of the grid positions, double the size of the sample width
- Application Si, ion beam current 20 nA
- After milling, use cleaning cross section to remove redeposition on the sides
- Go to ion beam deposition current, 0.26 nA
- Have the "flat" side pointing upwards, tilt 0°. Fig.4
- Insert omniprobe
- Omniprobe: go to "eucentric high"
- Align it using x- and y-directions to be parallel to the flat part
- Bring it lower using Z, use ion beam to check Z-position
- Check x and y position using electron beam
- Insert Pt-needle
- When liftout sample is in good position, do a 2 µm x 2 µm x 2 µm Pt deposition on one side, see figure 5. Application "Pt dep". Start the deposition on the sample.
- Retract the Pt-needle to avoid Pt-deposition while milling away the connection between the Omniprobe and the sample.
- Slowly raise the omniprobe. Retract Pt-needle. Omniprobe: "eucentric high", "Park".
- If the liftout sample is not firmly attached, do Pt-deposition on opposite side as well

8 Thinning

- Things to keep in mind when doing the final milling:
  - Move the stage as little as possible during the thinning phase, even a small amount of sample drift can lead to the sample being milled too much. Do not rotate the sample, just tilt it from 50° to 54°
  - Before start of milling: make sure there is no stage drift. Wait a minute to see if the image is moving. Do this at every step, especially if the stage has recently been moved.
  - When doing the milling, increase the magnification as much as possible, while still having the whole milling area inside the view
  - Use "End Point Monitor" when doing the final milling. Set it up to take an image for every milling line, and unpause the lower left viewing screen
- 52° tilt
- Start milling on the non-connected side, the end result should be a "staircase" with decreasing thickness closer to the non-connected side. See figure 7. Cleaning cross section, 0.92 nA ion beam, 30 keV, application Si. Clean both sides
- Tilt sample to 54° and mill bottom part of sample. 0.92 nA ion beam. Tilt sample to 52° and make sure the top side is even and straight. Z = about 1 µm, see if the sample is milled all the way down. If not, increase Z. If Z is too high, the copper beneath the sample can be sputtered. This will most likely lead to redeposition on the sample, which is not ideal.
- Tilt sample to 50° and mill top part of sample.
- Tilt sample to 52° and make sure the top side is even and straight. If not, mill away this using cleaning cross section.
- Repeat these steps, while reducing the x-size. The final thin area should be about 2 µm in the x-direction.
- At 1.5 µm reduce ion beam current to 28 pA
- At this point, it is ok if the lower, substrate, part is thicker compared to the top, thin film part. This will reduce the chance of the sample bending when it gets very thin
- The TLD detector is better for seeing thickness variations, so switch to this mode when the sample is thin.
- At 300 nm, change voltage to 5 keV, 48° and 56° tilt, 93 pA, cleaning from top. Z = 0.5 µm.
- When the top part of the protective layer starts being milled away, reduce the Z milling parameter (0.1 µm). Keep milling with End Point Monitor taking an e-beam image every line, when the top carbon protective layer starts disintegrating the sample should be thin enough.
- Use 2 keV, 81 pA, 48° and 56° tilt, z = 0.1 µm as finish. The beam will be very large, so its hard to image properly. But it should be possible to see where the thin part of the sample is located.

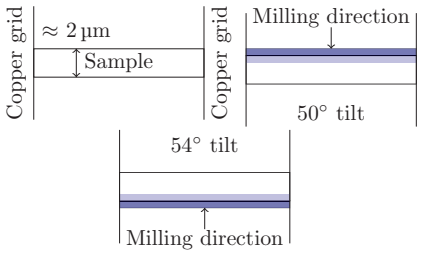

Figure 6: Final thinning of the sample

- Keep using End Point Monitor, and pay attention to the protective layer. Some parts of it should be milled away.

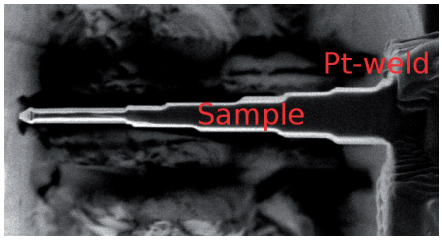

Figure 7: End result, showing the ”staircase” structure

Paper V: Supplementary material

Supplementary material

Concurrent magnetic and structural reconstructions at the interface of (111)-oriented $La_{0.7}Sr_{0.3}MnO_3/LaFeO_3$

I. Hallsteinsen[1,2], M.Moreau[1], A. Grutter[3], M.Nord[4,5], P-E. Vullum[5], D. A. Gilbert[3], T. Bolstad[1], F. Olsen[1], J. K. Grepstad[1], R. Holmestad[4], S. M. Selbach[6], A. T. N'Diaye[2], B. J. Kirby[3], E. Arenholz[2] and T. Tybell[1a)]

[1]Department of Electronics and Telecommunications, NTNU - Norwegian University of Science and Technology, Trondheim, 7491, Norway

[2]Advanced Light Source, Lawrence Berkeley National Laboratory, Berkeley, California 94720, USA

[3]Center for Neutron Research, National Institute of Standards and Technology, Gaithersburg, Maryland 20899

[4]Department of Physics, NTNU - Norwegian University of Science and Technology, Trondheim, 7491, Norway

[5]SINTEF Materials and Chemistry, 7491, Norway

[6]Department of Material Science, NTNU - Norwegian University of Science and Technology, Trondheim, 7491, Norway

I: Thin film synthesis and macroscopic magnetic data

The films were deposited at 540° C, 0.35 mbar oxygen pressure and 45mm target-substrate distance to obtain thermal mode growth with subsequent cooling in 100mbar oxygen pressure. A KrF excimer laser (λ=248 nm) with a fluency of ~2 Jcm^{-2} and repetition rate 1 Hz was employed, impinging on a stoichiometric targets. The 0.05° miscut STO(111) substrates were pretreated with buffered hydrogenfluoride and subsequently annealed at 1050° C in oxygen flow. The growth was monitored with RHEED, showing periodic oscillations characteristic of layer-by-layer growth, see Fig S1a). Cu Ka_1 x-ray diffraction, using a diffractometer equipped with a Göbel mirror, V-groove beam compressor and 0.2 mm detector slits, shows lattice constants consistent with fully strained (111)-oriented films, with out-of-plane d_{111} constants of 0.228 nm for LFO and 0.223 nm for LSMO i.e., compared to 0.225nm for STO. Fig S1b) shows a reflectometry plot is shown and in Fig S1c) a theta- 2theta diffraction plot of the (111) peak, which are both consistent with a total film thickness of 7.5 nm. Tapping mode atomic force microscopy revealed atomically smooth step-and-terrace surfaces, with steps of single d_{111} atomic layer height and a roughness of 0.10 nm on the plateaus as shown in Fig S1d). The macroscopic magnetic measurements were done with a vibrating sample magnetometer. In Fig S1e) the temperature dependence of the magnetic moment after 2T field cooling is plotted. No significant change was found for zero field cooling with similar samples.

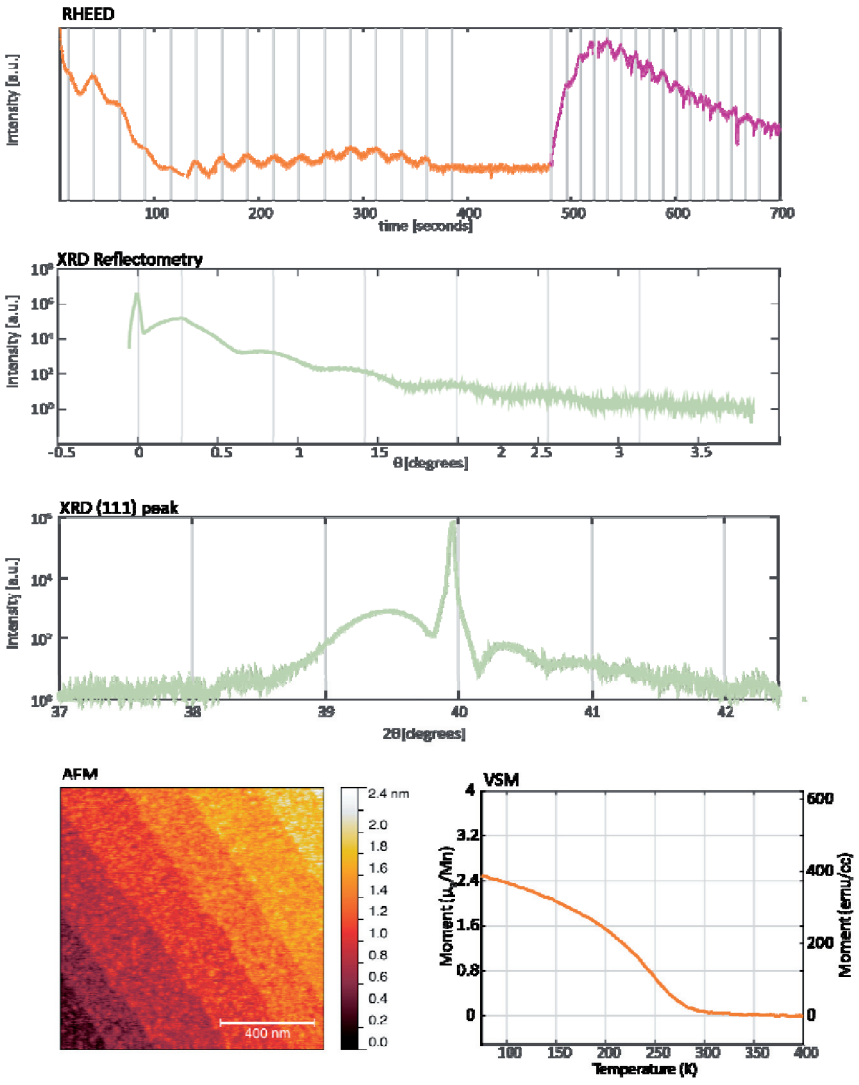

Fig S1:

a) RHEED oscillations during growth, plotted as intensity vs time. The plot line is colored orange during LFO growth, and purple during LSMO growth. The oscillation period is denoted by grey lines.
b) XRD reflectometry
c) XRD theta-2theta plot of the (111) peak
d) AFM image of 1μm x 1μm of the heterostructure after growth and cool down
e) Temperature dependence of the magnetic moment of the heterostructure measured by VSM

II: STEM and EELS investigations

The atomic structure was analyzed by scanning transmission electron microscopy (STEM) using high-angle annular dark field (HAADF), annular bright field (ABF) and electron energy loss spectroscopy (EELS).

STEM-HAADF and -ABF data were acquired simultaneously, using detector collection semi-angles from 73 to about 200 milliradians (HAADF) and 11.7 to 22.7 milliradians (ABF). The convergence semi-angle of the electron beam was 20.4 milliradians. To reduce the effects of scanning distortions the data was acquired as image stacks with a pixel time of 2.0 µs, resulting in two one-image stacks for the ABF and one image stack for the HAADF. The HAADF image stack was processed using SmartAlign [1] resulting in an HAADF data with reduced scanning distortions. Next, the ABF image stack was processed relying on the same distortion corrections as obtained for the HAADF data. The end result is scanning distorted corrected HAADF and ABF images.

The STEM-EELS data was acquired with a convergence semi-angle of 27.4 milliradians, a collection semi-angle of 33.2 milliradians. To obtain elemental maps, such as in Fig1a of the main manuscript, a power-law background subtracted and the response of the respective EELS edges: Ti-L23, Mn-L23, Fe-L23, La-M54 and Sr-L23 were depicted. The dark layer at the $LaFeO_3/SrTiO_3$-interface is due to interdiffusion, as discussed in Ref [2]. All EELS processing was done using HyperSpy [3]. The spatial resolution of the EELS signal is determined to be 0.15 nm by the width of fitted gaussian for the atomically resolved EELS map. The interface widths were defined by the decline from 75% to 25% of the elemental signal, for different processing: raw data, fitting to an arctan and a smoothing with a gaussian of FWHM of 0.4 nm, as shown in Fig S2. For all fits, the LSMO/LFO interface has a narrower interface width than the LFO/STO interface. The maximum interface length for LSMO/LFO is 0.6 nm, corresponding to one layer of each material.

To estimate the amount of structural distortions, two different measures were used: ellipticity of the A-cation columns and oxygen column superstructures in the (100)-direction. To determine the position and shape of the atomic columns, 2-D Gaussian fits were made to each atomic column. The A- and B-cation columns were fitted using the HAADF data, whilst the oxygen columns were fitted using the ABF image.

The ellipticity was found by using non-symmetric 2-D Gaussian fit with rotation, allowing for two different sigmas (x and y) that can rotate for the two Gaussians. To obtain a measure of the ellipticity the largest obtained sigma was divided with the smallest. This measure of ellipticity gives a measure on how much the A-cations "zig-zag" in the direction parallel to the electron beam. For a perfect cubic structure this value would be 1. However, we note that in the cubic $SrTiO_3$ substrate the ellipticity averaged to about 1.15 due to a range of factors: sample drift, non-perfect correction of astigmatism and residual effects of the scanning distortions. However, the increased ellipticity observed in the $LaFeO_3$ film is substantially larger compared to the noise level measured in the $SrTiO_3$.

The oxygen column superstructures was calculated by estimating the distance between a given oxygen column, and the next oxygen column in the (100)-direction, subtracting to the distance between the oxygen columns and the previous one. By dividing this number by 4 gives one gets a measure of how much the oxygen column position deviates from a perovskite

oxide with no oxygen octahedral tilting, or a octahedral tilting pattern not observable in this TEM-projection. Hence, for a cubic material, such as $SrTiO_3$ substrate this value is 0 pm, and for bulk $LaFeO_3$ 39.3 pm. We note that this approach results in a measure oscillating between positive and negative values.

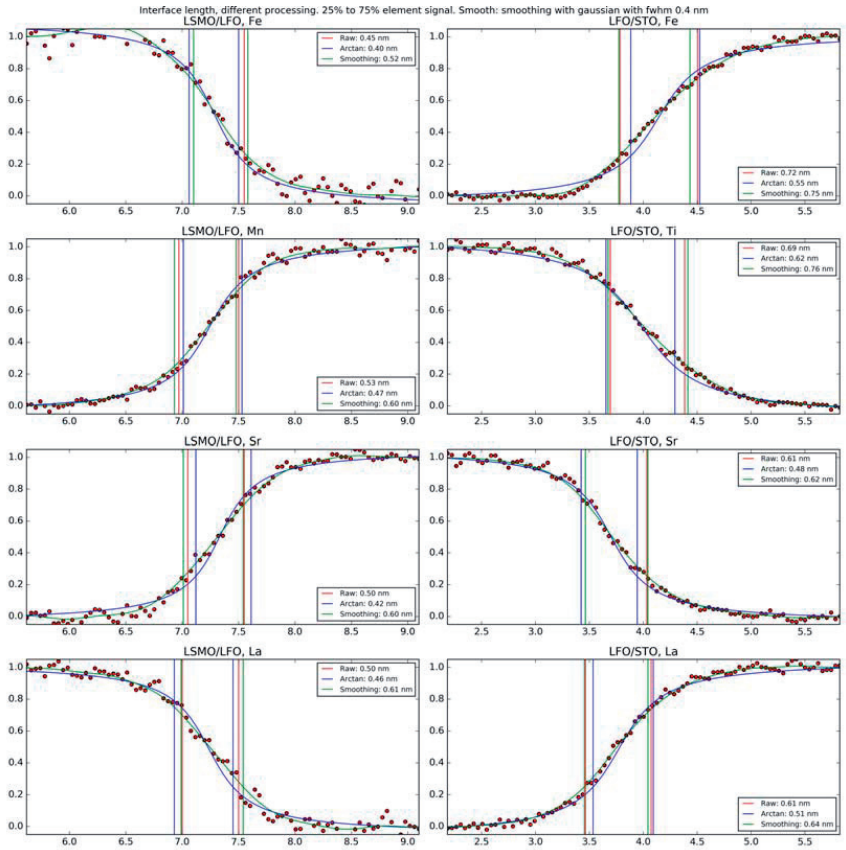

Fig S2:

Estimated width of the chemical interface (75-25% decline) by using the raw data (red), an arctan fit (blue) and a smoothed curve (green) for the different elements on the two interfaces in the heterostructure.

III: Neutron reflectivity fits

The structure and magnetization has also been refined through fitting a model which is identical except that the magnetization within the LFO layer is constrained to be zero. After optimization, we find an increase in the reduced Chi-squared from 1.121 in the case of magnetic LFO at the interface to 1.368 without an interfacial LFO moment. This increase of 22% originates in the fact that the spin "up-up" channel is undershot by the fit in the range of Qz = 0.75-1.2 nm^{-1} and the spin "down-down" channel is undershot from Qz = 0.075-0.9 nm^{-1}. As expected, the interface effect is quite subtle. However, the statistical significance of the difference is more than sufficient to establish an antiparallel magnetization in the interfacial LFO.

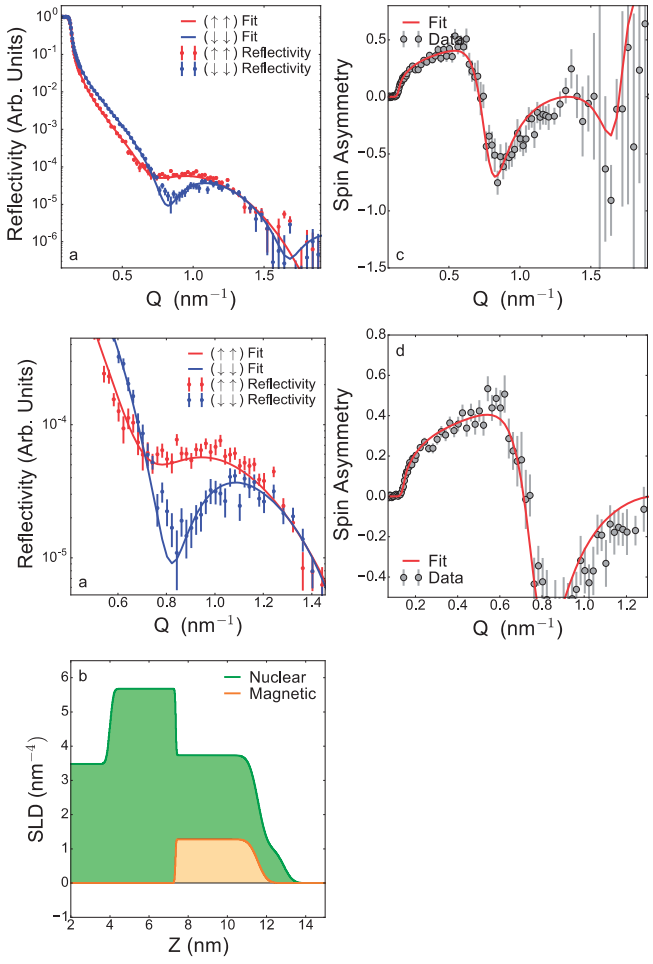

Fig S3:

Fits of the neutron reflectivity data and spin asymmetry without any induced ferromagnetism at LFO, as shown in the depth profile at the bottom of the figure.

III: DFT-investigations of the non-symmetric response of the Fe moments

The response of the Fe-moment were shown in Fig 5 b) of the main manuscript to not be symmetric with respect to the direction of the Mn-moment at the interface. In Fig S1 we show how the details of the spin structure changes when changing the Hubbard U-values of the Fe closest to the interface, U_{Fe},when the U_{Mn} = 3 and 5 eV. By reducing the U-values on Fe the reduction of Fe moment happens mainly at the closest Fe moment that has the spin direction parallel to the Mn spin direction. As shown, this effect is stronger when it is the first Fe-layer from the interface that is parallel to the spin direction of LSMO, as compared to the second Fe-layer. This can been seen by observing which arrows are reduced in Fig S4. When the manganese moment is positive (up) it is the first Fe layer from the interface that has the largest reduction of moment if having a positive (up) magnetization. When the manganese moment is negative (down) in Fig. S4, the reduction is largest in the second Fe-layer from the interface, which also has a negative moment (down). However, this reduction of moment in the second Fe-layer from the interface is not as large as the reduction for the first Fe-layer when the manganese moment is positive (up). We attribute the observed asymmetry to a proximity effect, where the distance to the LSMO is important due to reduced overlap of the wave functions.

The effect of reduced localization of the electrons on Fe can be further understood by considering the spin and layer resolved density of states (DOS), as shown in Fig. S5 and S6. Figure S5 shows the spin and layer resolved DOS for the case of a positive Mn moment and U_{Fe} = 1 eV and U_{Mn} = 5 eV at the layers closest to the interface. The Fe layer closest to the interface is then clearly metallic. In Fig S6 we show spin and layer resolved DOS for the same U-values, but with a negative Mn moment. Here we observe that there is some Fe states close to the Fermi level both in the layer closest to the interface and in the second Fe-layer from the interface, indicating a reduced localization in both layers.

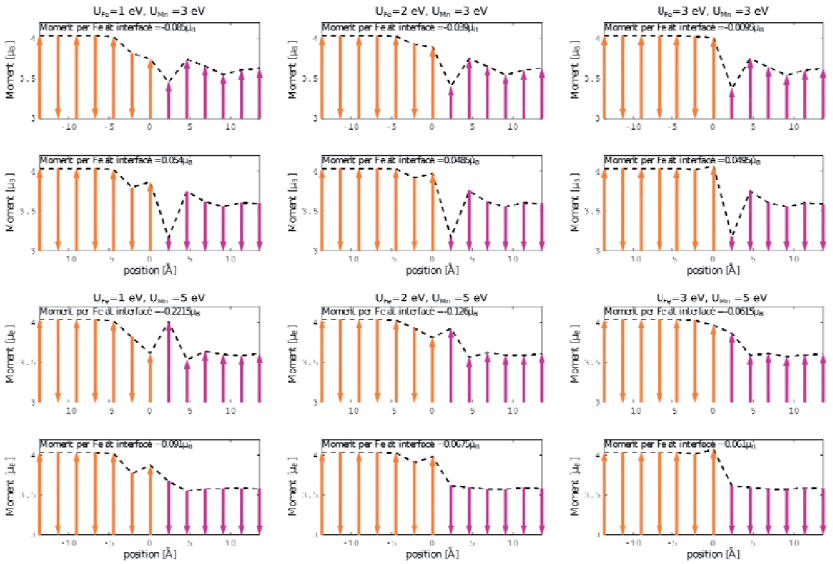

Figure S4, magnetic moment as a function of distance from the interface for different U_{Fe} and U_{Mn} at the interface and different alignment of the Mn moment, with respect to the Fe moments.

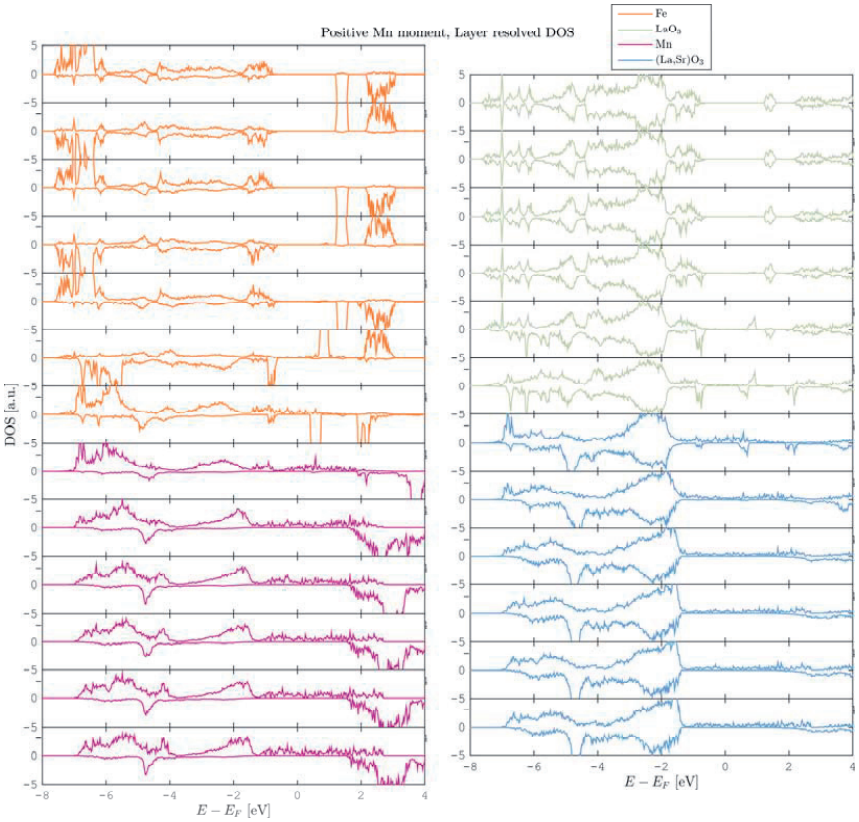

Figure S5, spin and layer resolved density of states for positive Mn moment and U_{Fe} = 1 eV and U_{Mn} = 5 eV at the interface. Spin up states are plotted on the positive *y*-axis while spin down are plotted on the negative *y*-axis. The different panels show the projection of the density of states for each d_{111} layer, as one crosses the interface in the [111]-direction.

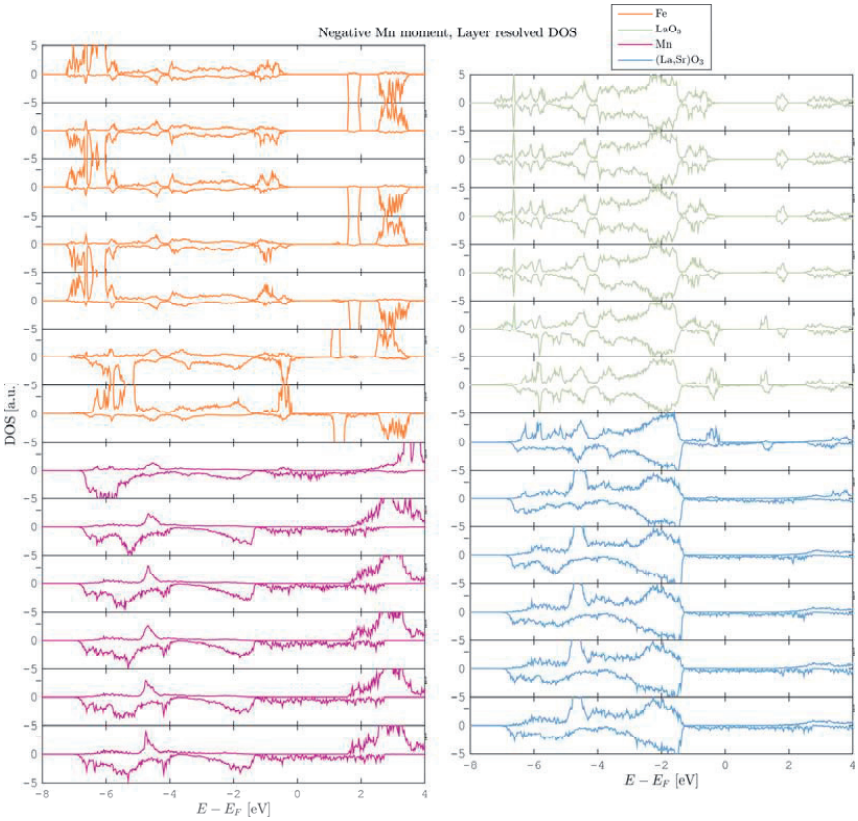

Figure S6, Spin and Layer resolved density of states for negative Mn moment and U_{Fe} = 1 eV and U_{Mn} = 5 eV at the interface. Spin up states are plotted on the positive *y*-axis while spin down are plotted on the negative *y*-axis. The different panels show the projection of the density of states for each d_{111} layer, as one crosses the interface in the [111]-direction.

[1] L. Jones, H. Yang, T. J. Pennycook, M. S. J. Marshall, S. Van Aert, N. D. Browning, M. R. Castell, and P. D. Nellist, Adv struct chem imaging **1**, 1 (2015).

[2] I. Hallsteinsen *et al.*, Crystal Growth & Design (2016).

[3] F. d. l. Peña *et al.*, hyperspy: HyperSpy 0.8.2.